AMORPHOUS METALLIC FOAM: SYNTHESIS AND MECHANICAL PROPERTIES

Thesis by

Chris Veazey

In Partial Fulfillment of the Requirements

for the Degree of

Doctor of Philosophy

California Institute of Technology

Pasadena, CA 91125

2007

(Defended July 6, 2006)

ACKNOWLEDGMENTS

I sincerely thank Bill Johnson for allowing me to pursue my Ph.D. under his extraordinary leadership. I am grateful to the professors of the Materials Science department for seeing potential in my application. It was a dream come true when Dr. Fultz called me to inform me of acceptance into the program. He was also kind enough to warn me about the difficulties of Caltech mathematics.

My studies were more successful and enjoyable by working with Jan Schroers, Marios Demetriou, Jay Hanan, Ersan Üstündag, and Bill Kaukler. I thank Dale Conner for his insightful advice along the way. My office mates, John Harmon, Joe Schramm, Andy Waniuk, and Greg Welsh, were great people to be around and helped me to succeed. I thank the Johnson group members for all their help and suggestions on research. I also thank my summer research assistants, including Blake Buchanan, Joan Christodoulou, and Kristen Virdone. I owe Pam Albertson for making the finances come together and for telling me what to expect.

I would like to thank my undergraduate advisor, Professor Kevin E. Johnson, of Pacific University. He encouraged me to attend graduate school and believed in my potential. I'd like to thank Chris Rubio for his friendship through the years that made Southern California feel like home. I am blessed by the love and support of my girlfriend and best friend, Kristy Drafahl. She was happy to edit this entire thesis and has helped me through the rough spots in research. And, I would not be here today if it were not for the loving attention of my parents, Thomas and Roxanne Veazey.

ABSTRACT

Bulk metallic glass alloys were processed into foam by several synthesis routes. These methods utilize the thermodynamic stability and thermoplastic formability of the supercooled liquid state to produce low-density homogeneous foams. The cellular structure is shown to evolve by growth of randomly distributed spherical bubbles towards polyhedral-like cells separated by microscopic intracellular membranes exhibiting random orientations and aspect ratios. The ability of amorphous metals to develop such random cellular morphologies is attributed primarily to the high ductility exhibited by their softened state, which enables large superplastic membrane elongations during foaming.

Upon loading, moderate porosity foams are known to deform plastically by recurring non-linear yielding transitions followed by non-catastrophic collapse events. The ability of these foams to yield non-catastrophically is a result of the plastic deformability of amorphous metals in sub-millimeter dimensions. Nonlinear yielding is found to be accommodated by clusters involving 4–6 cells, which yield by intracellular membrane buckling and ultimately collapse plastically to produce a localized plastic collapse band. By comparison, high-porosity foams deform plastically by multiple recurring non-catastrophic collapse events without undergoing macroscopic failure. The numerous minor collapse events are associated with localized ligament collapse, and the few major collapse events are associated with the cooperative collapse of several adjacent ligaments and the formation of a collapse band. On average, the serrated flow responses between major events appear to be self-similar and resemble the recurring nonlinear yielding responses exhibited by moderate porosity foams.

TABLE OF CONTENTS

CHAPTER 1 1
1.1 Motivation and objectives 1
1.2 Amorphous metallic foam literature 3
1.3 Conclusion 5
1.4 References 7
CHAPTER 2 9
2.1 Introduction 9
2.2 Crystallization kinetics 11
2.3 Sedimentation dynamics 12
2.4 Ductility of the supercooled liquid 14
2.5 A model of foam expansion kinetics in the supercooled liquid 15
2.6 Conclusion 22
2.7 References 23
CHAPTER 3 25
3.1 Introduction 25
3.2 Experimental alloying procedure of $Pd_{43}Ni_{10}Cu_{27}P_{20}$ 26
3.3 Alpha-foam experimental procedure 27
3.4 Alpha-foam results and discussion 28
3.5 Alpha-foam conclusion 30
3.6 Refined alpha-foam experimental procedure 31
3.7 Refined alpha-foam results and discussion 31
3.8 Refined alpha-foam conclusion 36
3.9 Beta-foam experimental procedure 37
3.10 Beta-foam results and discussion 39
3.11 Beta-foam conclusion 45
3.12 Refined beta-foam experimental procedure 45
3.13 Refined beta-foam results and discussion 46
3.14 Refined beta-foam conclusion 51
3.15 References 52
CHAPTER 4 53
4.1 Motivation and objectives 53
4.2 Moderate-porosity-foam mechanical properties 57
4.3 High-porosity-foam mechanical properties 71
4.4 References 74
CHAPTER 5 76
5.1 Summary 76
5.2 Future research on amorphous metallic foam 76
5.3 Future research on amorphous cellular composites 77
5.4 Future research on the application of amorphous metallic foam 78
5.5 Conclusion 80
5.1 References 81
APPENDIX I 82
APPENDIX II 92
APPENDIX III 96

CHAPTER 1

INTRODUCTION

1.1 Motivation and objectives

Discovered at the California Institute of Technology in 1960, metallic glasses possess exceptional mechanical properties such as high yield strengths (~2 GPa) [1], large elastic strain limits (2%), and a wide range of fracture toughness (20–55 MPa $\cdot$ $m^{1/2}$) [2,3]. Monolithic bulk metallic glasses (BMGs) have developed in thickness from microns to centimeters through years of research. The first metallic glass was a binary $Si_{25}Au_{75}$ alloy splat quenched at 10^6 K/s to a foil with a thickness of 10 microns [4]. Today, $Pd_{43}Ni_{10}Cu_{27}P_{20}$ has a critical casting thickness of 10 centimeters [5] and a critical cooling rate on the order of 0.1 K/s [6]. Exceptional glass stability allows a time window for $Pd_{43}Ni_{10}Cu_{27}P_{20}$ processing of 200 seconds at the nose of the time-temperature-transformation (TTT) diagram [6]. Plastic forming is possible due to the large range of attainable viscosities (from 10^{12} to 10^0 Pas) of the undercooled liquid [7].

Bulk metallic glasses are regarded as a new class of materials, as they differ fundamentally from conventional metals in their atomic structure, mechanical properties, and fundamental solidification behavior. Metallic glass-forming alloys vitrify (become configurationally “frozen”) upon cooling in the undercooled liquid state to form bulk glasses. Owing to the non-equilibrium nature of the vitrified state, glass transition involves no latent heat release and no discontinuous volume change. These factors, taken together, suggest that BMG could become a new-generation engineering material [7].

In mechanical loading, amorphous metals exhibit impressive strength and elastic strain yet yield catastrophically by incipient shear [8]. Over the past five years, metallic glass engineers have sought to alleviate brittleness by conceiving means to extend the attainable global plasticity. Precipitating a soft dendritic phase into the amorphous matrix [9] was shown to extend global plasticity substantially by catalyzing the formation of shear bands and hence proliferating plastic strain. This was attributed principally to the effect of soft inclusions to reduce the global shear-to-bulk modulus ratio [10], or equivalently, to increase the global Poisson's ratio, which designates the ability of the material to accommodate stress by shear. It thus became conceivable that introducing infinitely soft inclusions, such as pores [11], would contribute to extend global plasticity by increasing the global Poisson's ratio [12]. Moreover, in the limit of high porosity, the plastic deformability exhibited by amorphous metals in sub-mm dimensions [13] was thought to be a potentially exploitable engineering property of an amorphous metallic cellular structure. It was hence envisioned that a structure consisting of a network of efficiently arranged amorphous metallic membranes could exhibit unique mechanical characteristics.

Metallic foams find increasingly more interest as structural materials. This is to a large extent due to high stiffness in conjunction with very low specific weight and high energy-absorption capability [14]. This unique combination of properties makes foams an attractive structural material, which can mimic the mechanical characteristics of those foams found in nature, such as wood or bones. Foams can be classified as either open or closed porous. Open-celled foams are characterized by interconnected voids and are mainly used as functional materials such as thermal and acoustic insulation. Closed-

celled foams are characterized by spatially separated bubbles and find applications as structural materials such as energy absorbers or lightweight stiff materials. Since the amount of energy that can be absorbed scales with the strength of the material, BMGs exhibiting a yield strength on the order of 2 GPa [1] can be regarded as superior energy absorbers as compared to aluminum, which exhibits a strength of 250 MPa.

1.2 Amorphous metallic foam literature

Liquid metals can be foamed by various methods including gas-releasing blowing agents, gas injection, or infiltration into a space-holder. This thesis concentrates on the gas-releasing blowing-agent method. When heated, the blowing agent will release gas into the molten metal and drive expansion of gas bubbles. The first foam-synthesis route was developed by the Shinko Wire Company to foam aluminum using TiH_2 as a blowing agent. Typically, additives such as calcium are stirred into the aluminum melt to increase viscosity and thereby improve foam stability. Foam with 90% porosity can be produced by this method [14]. Similar strategies utilized in foaming conventional metals can be applied to the foaming of bulk metallic glass.

Historically, the first theoretical strategy for foaming bulk metallic glass was termed dynamic decompression and cooling (DDC) and was proposed by Apfel and Qiu [15]. The first step of the process is to supersaturate the melt with droplets of volatile liquid, followed by dynamic depressurization, which causes rapid vaporization. The result is rapid expansion and quenching of the melt due to the latent heat of vaporization. This process is limited because there are few volatile liquids that will remain in liquid form up to the relatively high liquidus temperature of BMGs.

Over the last three years, amorphous metallic foam (AMF) has gathered considerable attention from numerous materials science research centers. In early 2003, Schroers and co-workers reported development of closed-cell amorphous metallic foam by expansion of entrained bubbles in the undercooled liquid state as shown in Figure 1 [16]. Later in 2003, Wada and Inoue reported the development of open-cell amorphous metallic foam by salt replication [17]. In early 2004, Brothers and Dunand reported the development of closed-cell syntactic amorphous metallic foam by liquid infiltration into carbon micro-spheres [18]. Later in 2004, Wada and Inoue reported formation of closed-cell amorphous metallic foam by precipitation of dissolved hydrogen [19]. In late 2004, Schroers and co-workers proposed a thermoplastic foam-expansion method, which involves expansion of entrained bubbles in the supercooled liquid state [20]. In early 2005, Brothers and Dunand presented an improved methodology for the development of open-cell amorphous metallic foam by salt replication [21]. A comprehensive report on the progress in the various synthesis methods of amorphous metallic foam can be found in [22].

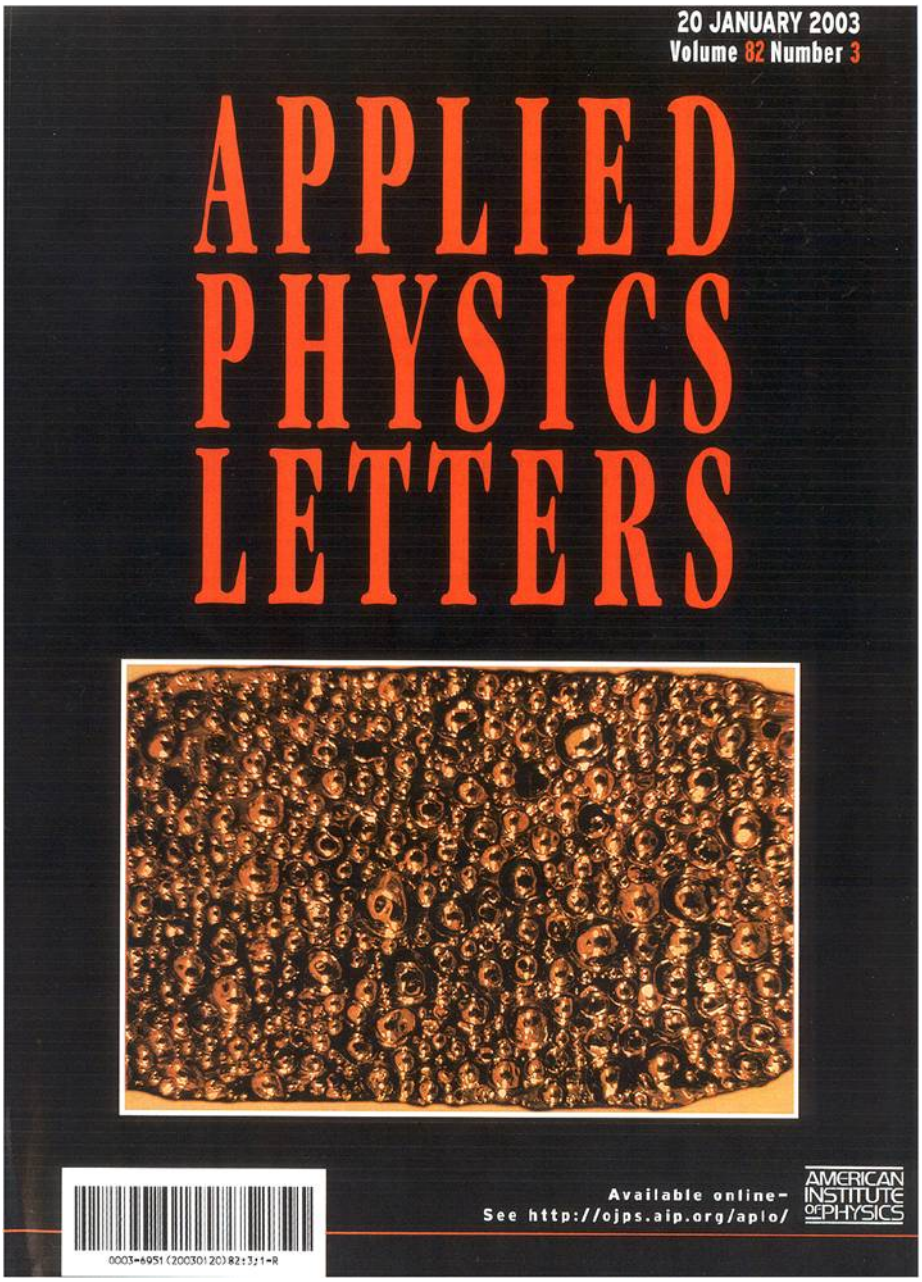

Figure 1. Amorphous metallic foam, which appeared on the cover of Applied Physics Letters January 20th, 2003

1.3 Conclusion

The engineering potential of a thermoplastically expanded amorphous metallic foam was conceived by recognizing the improvement in global attainable plasticity that can be realized by introducing pores in the bulk amorphous phase [11]. Moreover, the

surprising bending ductility exhibited by amorphous metallic struts at microscopic sizes [13], as shown in Figure 2, was thought to be a potentially functional engineering property of a highly porous amorphous metallic foam. It has hence been envisioned that an amorphous metallic structure, which encompasses a network of efficiently arranged microscopic struts, would be capable of undergoing superior global elasticity and plasticity. In fact, the vision of such highly networked amorphous metallic cellular structure constituted the drive for the development of a vigorous research project, aiming to gain insight into the morphological development and the mechanical behavior of this emerging structural material.

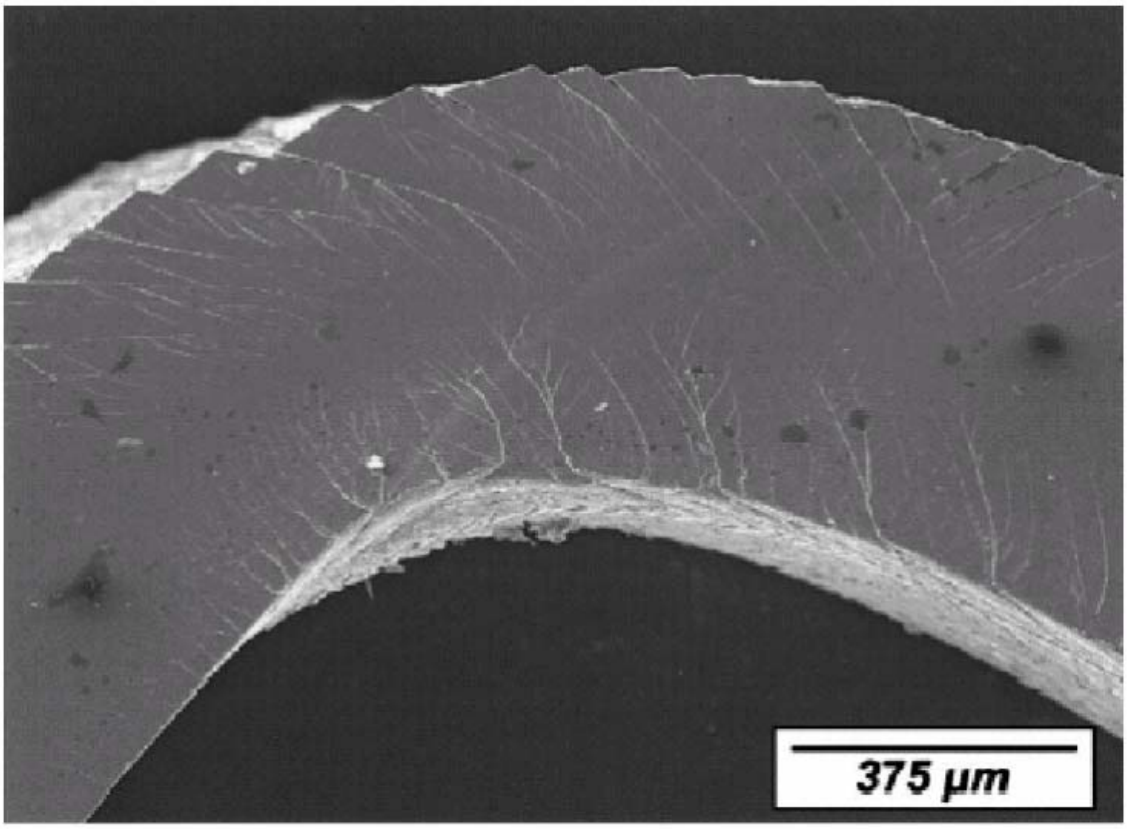

Figure 2. SEM micrograph of shear bands observed in a thin strip of Vitreloy 106a after mechanical bending. Figure is from [Conner RD, Johnson WL, Paton NE, Nix WD. J. Appl. Phys. 2003;94:904.]

1.4 References

[1] Bruck HA, Christman T, Rosakis AJ, Johnson WL. Quasi-Static Constitutive Behavior of $Zr_{41.25}Ti_{13.75}Ni_{10}Cu_{12.5}Be_{22.5}$ Bulk Amorphous-Alloys. Scr. Metall. Mater. 1994;30:429.

[2] Lowhaphandu P, Lewandowski JJ. Fracture toughness and notched toughness of bulk amorphous alloy: Zr-Ti-Ni-Cu-Be. Scr. Mater. 1998;38:1811.

[3] Gilbert CJ, Ritchie RO, Johnson WL. Fracture toughness and fatigue-crack propagation in a Zr-Ti-Ni-Cu-Be bulk metallic glass Appl. Phys. Lett. 1997;71:476.

[4] Klement W, Willens RH, Duwez P. Non-Crystalline Structure in Solidified Gold-Silicon Alloys. Nature 1960;187:869.

[5] Telford M. The case for bulk metallic glass. Mater. Today 2004;7:36.

[6] Schroers J, Johnson WL, Busch R. Crystallization kinetics of the bulk-glass-forming $Pd_{43}Ni_{10}Cu_{27}P_{20}$ melt. Appl. Phys. Lett. 2000;77:1158.

[7] Johnson WL. Bulk amorphous metal - An emerging engineering material. JOM 2002;54:40.

[8] Pampillo CA. Localized Shear Deformation in a Glassy Metal. Scr. Metall. 1972;6:915.

[9] Hays CC, Kim CP, Johnson WL. Microstructure controlled shear band pattern formation and enhanced plasticity of bulk metallic glasses containing in situ formed ductile phase dendrite dispersions. Phys. Rev. Lett. 2000;84:2901.

[10] Schroers J, Johnson WL. Ductile bulk metallic glass. Phys. Rev. Lett. 2004;93.

[11] Wada T, Inoue A, Greer AL. Enhancement of room-temperature plasticity in a bulk metallic glass by finely dispersed porosity. Appl. Phys. Lett. 2005;86.

[12] Phani KK, Sanyal D. Critical reevaluation of the prediction of effective Poisson's ratio for porous materials. J. Mater. Sci. 2005;40:5685.

[13] Conner RD, Johnson WL, Paton NE, Nix WD. Shear bands and cracking of metallic glass plates in bending. J. Appl. Phys. 2003;94:904.

[14] Banhart J. Manufacture, characterisation and application of cellular metals and metal foams. Prog. Mat. Sci. 2001;46:559.

[15] Apfel RE, Qiu N. Principle of dynamic decompression and cooling for materials processing. J. Mater. Res. 1996;11:2916.

[16] Schroers J, Veazey C, Johnson WL. Amorphous metallic foam. Appl. Phys. Lett. 2003;82:370.

[17] Wada T, Inoue A. Fabrication, thermal stability and mechanical properties of porous bulk glassy Pd-Cu-Ni-P alloys. Mater. Trans. JIM 2003;44:2228.

[18] Brothers AH, Dunand DC. Syntactic bulk metallic glass foam. Appl. Phys. Lett. 2004;84:1108.

[19] Wada T, Inoue A. Formation of porous Pd-based bulk glassy alloys by a high hydrogen pressure melting-water quenching method and their mechanical properties. Mater. Trans. JIM 2004;45:2761.

[20] Schroers J, Veazey C, Demetriou MD, Johnson WL. Synthesis method for amorphous metallic foam. J. Appl. Phys. 2004;96:7723.

[21] Brothers AH, Dunand DC. Ductile bulk metallic glass foams. Adv. Mat. 2005;17:484.

[22] Brothers AH, Dunand DC. Amorphous metal foams. Scr. Mater. 2006;54:513.

CHAPTER 2

TECHNOLOGICAL ASPECTS OF THERMOPLASTIC AMORPHOUS METAL FOAMING

2.1 Introduction

Foaming liquid metals is a challenging task since the dynamics of bubble nucleation, growth, sedimentation, merge, and collapse scale inversely with liquid viscosity, which for conventional metals is relatively low. The viscosity at the liquidus is 10^{-3} Pa s for a pure metal [1] and 1 Pa s for a BMG [2]. Therefore, the foaming kinetics of BMGs are expected to be drastically slower compared to pure metals. In addition, one of the unique features of BMG-forming liquids is the existence of a supercooled liquid state that is continuous and exhibits excellent stability against crystallization [3,4]. This metastable liquid state appears in a temperature region between glass transition and crystallization. An interest in "thermoplastically" processing amorphous metallic foam evolved by recognizing the exceptional forming ability of the supercooled liquid state of amorphous metals [5, 6].

The supercooled liquid state of these alloys exhibits a remarkable rheology characterized by viscosities that vary smoothly and predictably from viscous fluid to solid. This rheology renders bulk amorphous metals suitable for thermoplastic processes similar to the processing of plastics and conventional glasses [7]. The strong dependence of viscosity on temperature allows for precise control of the foam expansion process by varying temperature within the supercooled region. Such processing ability of the

supercooled liquid state is ideal for thermoplastic foaming [5,6]. Furthermore, amorphous metals in their supercooled liquid state are known to exhibit near-ideal ductility enabling nearly infinite plastic elongations [8]. It has therefore been envisioned that large superplastic elongations of intracellular membranes during thermoplastic foaming can lead to the development of highly networked amorphous metallic cellular structures.

To date, success in thermoplastic foaming of amorphous metals has only been reported in palladium based amorphous metallic alloys [9-12]. Amorphous metals from this alloy family possess a fairly robust and stable supercooled liquid state, and can hence be considered suitable for thermoplastic processing. Principally, the suitability of these alloys for thermoplastic foam processing stems from their low chemical reactivity, which enables the utilization of foaming agents. Most importantly, however, the foaming agents must be able to release gas at temperatures near the liquidus temperature of the alloy. Foaming agents typically consist of inorganic, thermally unstable compounds, which at a certain temperature decompose to release gas. By utilizing such blowing agents, thermoplastic foaming becomes attainable, since the enormous volume of gas chemically stored in these compounds (typically 1000:1) can provide substantial driving force for expansion when entrained in the metal. For the Pd-based amorphous metallic systems, an obvious choice for a foaming agent is hydrated boron oxide or boric acid (H_3BO_3). Dry boron oxide (B_2O_3) is commonly used as a fluxing agent for Pd-based systems [4,13,14], and hence its hydrated form can be thought of as a natural foaming agent. Other inorganic compounds such as carbonates, nitrates, or hydrides, which decompose at temperatures above the alloy glass transition, can also be utilized as

foaming agents for the Pd-based alloys. On the other hand, zirconium based amorphous metallic alloys are equally robust and well suited for thermoplastic processing, however they are highly reactive. It is therefore impractical to utilize a foaming agent effectively for these alloys, which are hence rendered unsuitable for thermoplastic foaming. Other foaming methods such as micro-sphere infiltration [15] or salt replication [16] have been proven more successful in producing Zr-based amorphous metallic foam.

2.2 Crystallization kinetics

The challenge of making amorphous foams by cooling the sample from the stable liquid is to circumvent crystallization during subsequent cooling. A minimum quench rate is required to bypass crystallization, which is termed the critical cooling rate. The quench rate is dictated by the rate of heat removal such that limitations are imposed on the dimensions of products that can be cast amorphous. The largest size that can be cast amorphous is often identified as the critical casting thickness. In order to extract heat sufficiently fast enough to avoid crystallization, amorphous foam dimensions are restricted in one dimension. Thus, techniques used for commercial metal foam production are excluded since they do not allow fast cooling.

The influence of the foaming process on the critical cooling rate, assuming the foaming process does not cause heterogeneous crystal nucleation, can be estimated through the increase in thermal diffusion length. If $\alpha_g << \alpha_l$ (α : thermal conductivity), $\rho_g << \rho_l$, and $c_{p,g} \leq c_{p,l}$ the heat will predominately transfer through the liquid. This requires an increased diffusion length since the linear path is interrupted. Assuming a dense packing of spherically shaped, uniform bubbles, the additional diffusion length can

be calculated by comparing the length of going around a bubble with the bubble diameter, resulting in a factor of $\pi/2$. This results in a critical casting thickness for a foam that is a factor of $2/\pi$ (or 65%) of the bulk material critical casting thickness.

2.3 Sedimentation dynamics

Owing to the high viscosities characterizing BMG-forming liquids, bubble sedimentation can be reduced to negligible levels. The sedimentation velocity, u, of a gas bubble in a liquid can be approximated by Stokes equation:

$$u = \frac{8R^2(\rho_l - \rho_g)g}{9\eta} \quad (1)$$

where R is the radius of the bubble; ρ_l and ρ_g are the densities of liquid and gas, respectively; g the gravitational acceleration; and η is the viscosity. To evaluate the sedimentation dynamics in BMG-forming liquids, the sedimentation velocity of 1 atm argon gas bubbles in the $Pd_{43}Ni_{10}Cu_{27}P_{20}$ liquid is considered at two different temperatures: 870 K and 650 K. The temperature of 870 K is the liquidus temperature of this alloy, while the temperature of 650 K is within the supercooled liquid region. Therefore, these temperatures represent the processing temperatures for the prefoaming stage (step 1) and the foam expansion stage (step 3), respectively (Figure 1). The ideal gas law is used for the density of argon, while for $Pd_{43}Ni_{10}Cu_{27}P_{20}$ liquid the density is taken as 9340 kg/m^3 (measured), and the viscosities at 870 K and 650 K are taken as 0.6 Pa-s and 1.1×10^6 Pa-s, respectively [17]. A limit for detectable sedimentation can be established by considering that in 1 cm samples, sedimentations of less than 1 mm during experimental times of 100 s are undetectable. This criterion therefore suggests that

undetectable stratification can be characterized by sedimentation velocities of less than 10 μm/s. The results for the sedimentation velocity as a function of bubble radius as estimated from Eq. (1) are shown in Figure 1. At the temperature of 870 K, where prefoam processing takes place, the criterion for negligible sedimentation can be fulfilled for bubble radii of less than 10 μm. This suggests that sedimentation would be undetectable in prefoams with an average bubble size of 10 microns. At the temperature of 650 K however, where foam expansion is processed, the criterion for negligible sedimentation can be fulfilled for bubble radii of less than 1 cm. This implies that during foam expansion, bubble sizes in the centimeter range can be produced without detectable sedimentation.

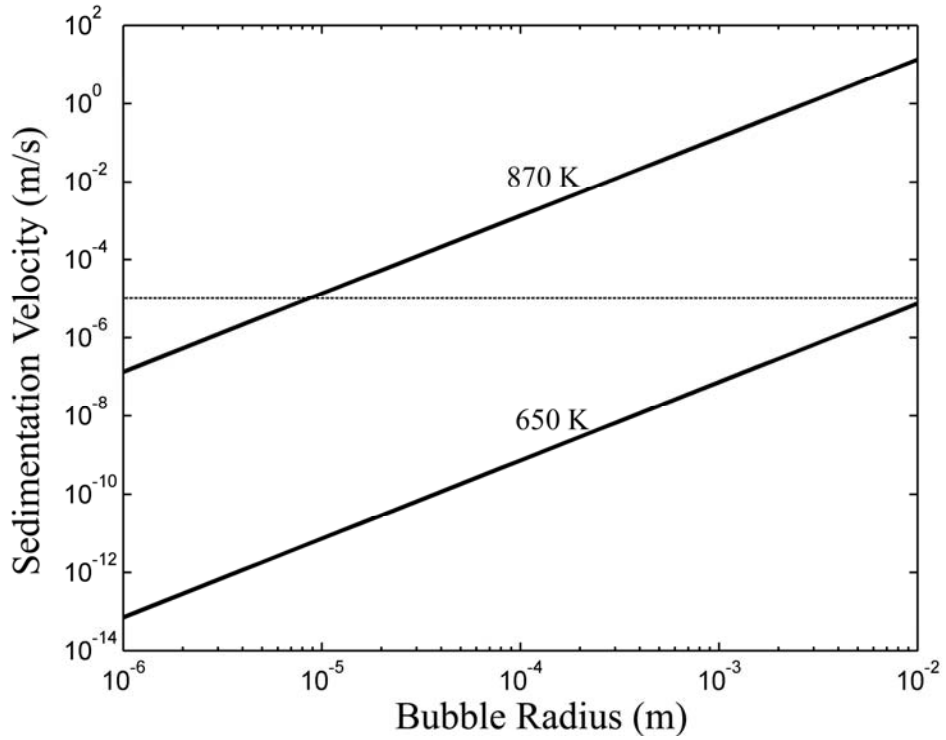

Figure 1. The sedimentation velocity of bubbles in $Pd_{43}Ni_{10}Cu_{27}P_{20}$ liquid as a function of bubble radius at temperatures 870 K (liquidus) and 650 K (deeply undercooled region) as computed by Eq. (1).

Therefore, owing to the excessively high viscosities of BMG-forming liquids, no density gradients along the gravity direction caused by bubble sedimentation are expected to form in foam products produced by this method. However, non-uniformities in the morphologies may appear in these foams. Such non-uniformities are attributed to the strong dependence of viscosity on temperature in the supercooled liquid region. As will be demonstrated in Section 2.5, the kinetics of bubble expansion scale inversely with viscosity. Even shallow temperature gradients during foam expansion can give rise to steep viscosity gradients, which would contribute to spatially non-uniform bubble growth and ultimately to non-uniform morphology. Therefore, in order to achieve spatially uniform foam morphologies by this method, it is essential to process foam expansion under uniform temperatures.

2.4 Ductility of the supercooled liquid

Solid-state foaming of crystalline metals was proven to be rather limited, as the attainable porosities are restricted to near 40% [18]. Owing to enormously high viscosities, superplastic deformation of crystalline metals is associated with creep rather than flow, and consequently the attainable plasticity is limited. On the other hand, visco-plastic deformation of supercooled liquids is associated with flow and gives rise to near-ideal plastic behavior. In fact, it has been demonstrated that stretching of a supercooled liquid under a low strain rate can produce plastic elongations as high as 150,000% [8].

Within the supercooled liquid region, flow is Newtonian for low strain rates, i.e., it exhibits no strain-rate sensitivity. The limiting strain rate at different temperatures for Newtonian flow of $Pd_{43}Ni_{10}Cu_{27}P_{20}$ supercooled liquid is shown in Figure 2 [19]. As the

flow becomes non-Newtonian at higher strain rates, its strain-rate sensitivity increases resulting in shear thinning and necking upon tension. When the porosity during foaming approaches a critical value (typically less than the density of random sphere packing of 63.7%), further expansion is possible by membrane stretching, provided that flow exhibits low strain-rate sensitivity and membrane necking is avoided. Therefore, in order to attain porosities exceeding 70%, expansive flow should be nearly Newtonian.

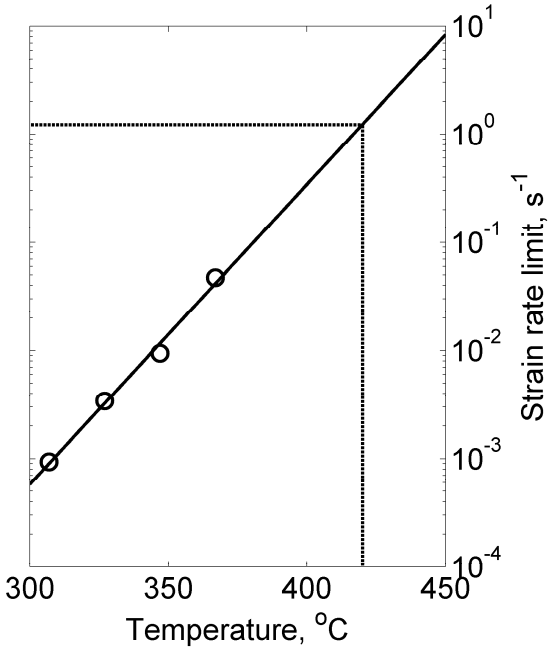

Figure 2. Limit of strain-rate sensitivity of $Pd_{43}Ni_{10}Cu_{27}P_{20}$ liquid at different temperatures from [Saotome Y, Itoh K, Zhang T, Inoue A. Scr. Mater. 2001;44:1541.]. By extrapolation, the strain rate limit to maintain Newtonian flow at 420 °C is estimated to be ~1 s^{-1}.

2.5 A model of foam expansion kinetics in the supercooled liquid

In this section, a model for the kinetics of foam expansion in a BMG-forming liquid is established in order to assess the feasibility of the foam expansion process. The model utilizes available kinetic data for the supercooled liquid and evaluates the expansion kinetics of individual bubbles by assuming the bubbles maintain spherical

symmetry and the liquid is infinite and incompressible. The current model is not intended to simulate the expansion evolution during foaming accurately, but rather to give an approximate assessment of the feasibility of processing foam expansion in the supercooled liquid region.

Denoting the bubble pressure on the gas-side of the interface as p_i, the pressure on the liquid-side of the interface as p_o, and the far-stream liquid pressure as p_∞, the total driving force for growth $\left(p_i - p_\infty\right)$ can be expressed as a sum of an interfacial driving force $\left(p_i - p_o\right)$ and a far-stream driving force $\left(p_o - p_\infty\right)$, as follows:

$$\left(p_i - p_\infty\right) = \left(p_i - p_o\right) + \left(p_o - p_\infty\right) \tag{2}$$

The interfacial kinetics are taken as suggested by Poritsky [20]:

$$\left(p_i - p_o\right) = 4\eta \frac{dR/dt}{R} + \frac{2\sigma}{R} \tag{3}$$

where σ is the surface tension, η is the liquid viscosity, and R is the time-dependent bubble radius. The first term on the right represents the principal normal stresses on the bubble while the second term constitutes the surface-tension contribution. The far-stream inertia kinetics are given by the irrotational-flow analysis of Rayleigh [21] as follows:

$$\left(p_o - p_\infty\right) = \rho\left[R\frac{d^2R}{dt^2} + \frac{3}{2}\left(\frac{dR}{dt}\right)^2\right] \tag{4}$$

where ρ is the liquid density. Furthermore, the pressure at the gas-side of the bubble interface can be related to the number of moles of the gas, n, by assuming the ideal gas law:

$$p_i = \frac{nRT}{\left(4\pi/3\right)R^3} \tag{5}$$

where R is the gas constant and T is temperature. The number of moles, n, which is conserved during expansion, can be obtained from the initial gas pressure in the bubble p_0. Substituting Eqs. (3)–(5) into Eq. (2):

$$\rho R\frac{d^2R}{dt^2}+\frac{3}{2}\rho\left(\frac{dR}{dt}\right)^2+\frac{4\eta}{R}\frac{dR}{dt}=\frac{nRT}{(4\pi/3)R^3}-\frac{2\sigma}{R}-p_\infty \tag{6}$$

Equation (6) is a differential equation governing the growth evolution of a single bubble from an initial size R_0 to an equilibrium size R_{eq}, which can be obtained by setting $dR/dt = d^2R/dt^2 = 0$ in Eq. (6). Owing to the excessively high viscosities characterizing BMG-forming liquids, Eq. (6) can be simplified substantially by means of a scaling analysis. Two relaxation processes take place during bubble growth: far-stream hydrodynamic relaxation, which for such irrotational flow is characterized by a time scale of $\tau_{hyd} = \Delta R\sqrt{\rho/\Delta p}$, and interfacial stress relaxation, which is characterized by a diffusive time scale of $\tau_{vis} = \rho\Delta R^2/4\eta$. In the above expressions, $\Delta R = R_{eq} - R_0$ and $\Delta p = p_0 - p_\infty$. Defining dimensionless variables as $\hat{R} = R/\Delta R$ and $\hat{t} = t/\tau_{hyd}$, Eq. (6) can be scaled as follows:

$$\hat{R}\frac{d^2\hat{R}}{d\hat{t}^2}+\frac{3}{2}\left(\frac{d\hat{R}}{d\hat{t}}\right)^2+\frac{\tau_{hyd}}{\tau_{vis}}\frac{1}{\hat{R}}\frac{d\hat{R}}{d\hat{t}}=\frac{nRT}{\Delta p(4\pi/3)\Delta R^3}\frac{1}{\hat{R}^3}-\frac{2\sigma}{\Delta p\Delta R}\frac{1}{\hat{R}}-\frac{p_\infty}{\Delta p} \tag{7}$$

For excessively high viscosities the time-scale ratio becomes $\tau_{hyd}/\tau_{vis} >> 1$ such that the inertia contribution (first two terms on the left of Eq. (6)) becomes vanishingly small compared to the interfacial stress contribution (third term on the left). Accordingly, the evolution equation can be simplified to the following dimensional form:

$$\frac{4\eta}{R}\frac{dR}{dt}=\frac{nRT}{(4\pi/3)R^3}-\frac{2\sigma}{R}-p_\infty \tag{8}$$

Equation (8) can be used to model the growth evolution of a single bubble expanding in a highly viscous liquid. Since inertia terms are vanishingly small, the constraint for the liquid to extend to infinity can therefore be relaxed. This implies that interactions between adjacently expanding bubbles would be negligible, i.e., bubbles would essentially expand like balloons. The above argument, however, is only true when no merging of bubbles takes place. Nevertheless, under the assumption of no bubble merging, Eq. (8) could be employed to simulate the growth evolution adequately of a size distribution of bubbles expanding in a viscous liquid.

In the context of this study, the supercooled liquid will be assumed to be structurally relaxed to its equilibrium state during expansion, i.e., its viscosity will be assumed to be at its Newtonian value. Under this assumption, non-equilibrium effects contributed by quenched-in free volume or induced by strain rates during growth are neglected. In practice however, such non-equilibrium effects may become important and may contribute to dramatically decrease the viscosity, and hence substantially increase the kinetics of expansion. Under such assumptions, the kinetics are accounted for conservatively and hence expansion is evaluated at the slowest possible rate. The Newtonian viscosity of $Pd_{43}Ni_{10}Cu_{27}P_{20}$ as evaluated recently by Fan et al.[7] will be employed: $\log_{10}(\eta) = -6.8 + 2\times 2880 \Big/ \left\{ T - 447 + \left[(T-447)^2 + 4\times 7.3T \right]^{1/2} \right\}$ Pa-s. The surface tension of $Pd_{43}Ni_{10}Cu_{27}P_{20}$ can be approximated by that of $Pd_{76}Cu_6Si_{18}$ [22]: $\sigma = 1.399 + 0.26\times 10^{-3}(T - 1033)$ N/m. For the density of $Pd_{43}Ni_{10}Cu_{27}P_{20}$, the measured value of $\rho = 9340$ kg/m^3 will be utilized.

In order to evaluate the accuracy of Eqs. (6) and (8), and hence validate the scaling analysis given by Eq. (7), the expansion of a 100 μm bubble in supercooled

$Pd_{43}Ni_{10}Cu_{27}P_{20}$ liquid at 650 K for 3000 s is considered. The initial bubble pressure p_0 is taken to be 10^5 Pa, while the far-stream liquid pressure p_∞ is taken to be 1 Pa. Under these conditions, the time-scale ratio becomes $\tau_{hyd}/\tau_{vis} \sim 10^5$, hence implying negligible inertia effects, and accordingly Eq. (8) must be a good approximation to Eq. (6). Equations (6) and (8) are both non-linear and were therefore solved numerically. A MATLAB solver with a relative tolerance of 10^{-12} was employed. The computed evolutions from the initial size to the equilibrium one predicted by the two equations are shown in (Figure 3). The evolutions appear to be identical, hence verifying the validity of the scaling analysis and suggesting that Eq. (8) is adequate to simulate evolution in a highly viscous liquid.

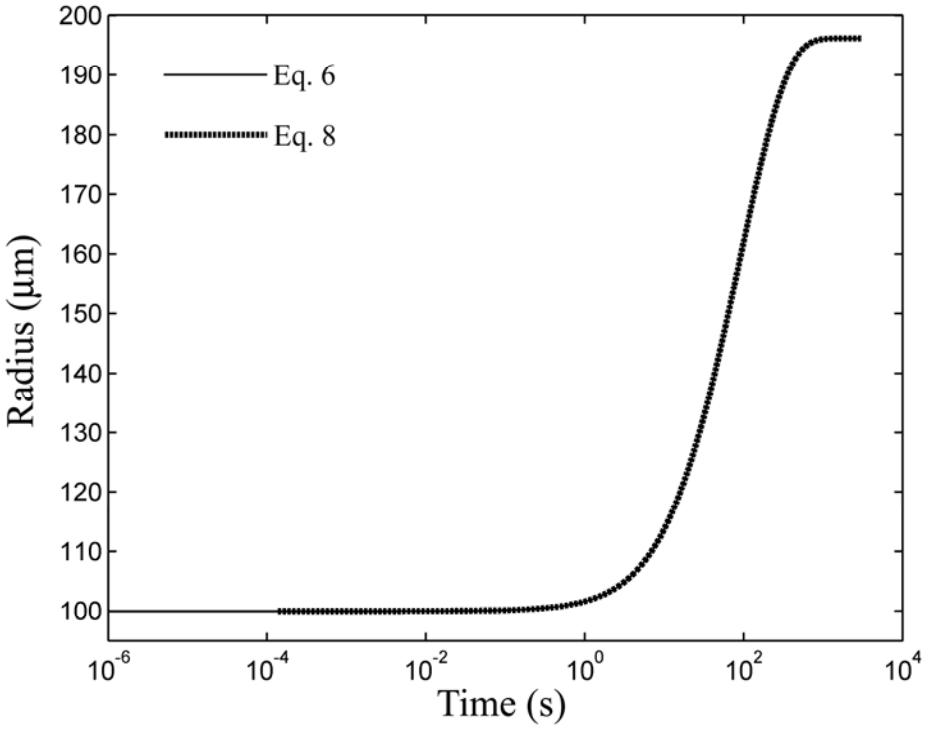

Figure 3. Expansion evolution of a 100 mm radius bubble initially at p_i = 105 Pa expanding in undercooled $Pd_{43}Ni_{10}Cu_{27}P_{20}$ liquid at 675 K and p_∞ = 1 Pa, as computed by Eqs. (6) and (8).

The developed model, Eq. (8), is employed to investigate the effect of varying temperature in the supercooled liquid region on the expansion evolution. Expansion of a 100 μm bubble for 3000 s in undercooled $Pd_{43}Ni_{10}Cu_{27}P_{20}$ liquid was considered. The far-stream pressure was taken to be 1 Pa. The computed evolutions at temperatures 625, 650, and 675 K for an initial gas pressure of 10^5 Pa are shown in Figure 4. The results suggest that for the processing conditions considered, the bubbles at 650 K and 675 K would attain the equilibrium size, while the one at 625 K would grow substantially but would not attain equilibrium. From the results it appears that the expansion kinetics are enhanced substantially by increasing temperature as a consequence of the dramatic decrease in viscosity. The viscosities at temperatures 625, 650, and 675 K are 3.5×10^7, 1.1×10^6, and 6.6×10^4 Pa-s, respectively. In order to assess whether adequate expansion is possible before crystallization sets in, the expansion kinetics must be compared against crystallization kinetics. This can be accomplished by superimposing the time for isothermal crystallization, as obtained from an experimental TTT diagram, onto the expansion evolution. The crystallization times at temperatures 625, 650, and 675 K are obtained from the experimental TTT diagram [23] as 2470, 600, and 112 s, respectively, and are superimposed on the plot by an asterisk (Figure 4). From the results it appears that at 675 K and 650 K, expansion equilibrates before crystallization sets in; however at 625 K, crystallization precedes equilibration. The model therefore confirms that under the slowest possible kinetic conditions (i.e., equilibrium Newtonian conditions), expansion in the deeply undercooled liquid is feasible, as a processing time window exists between expansion and crystallization.

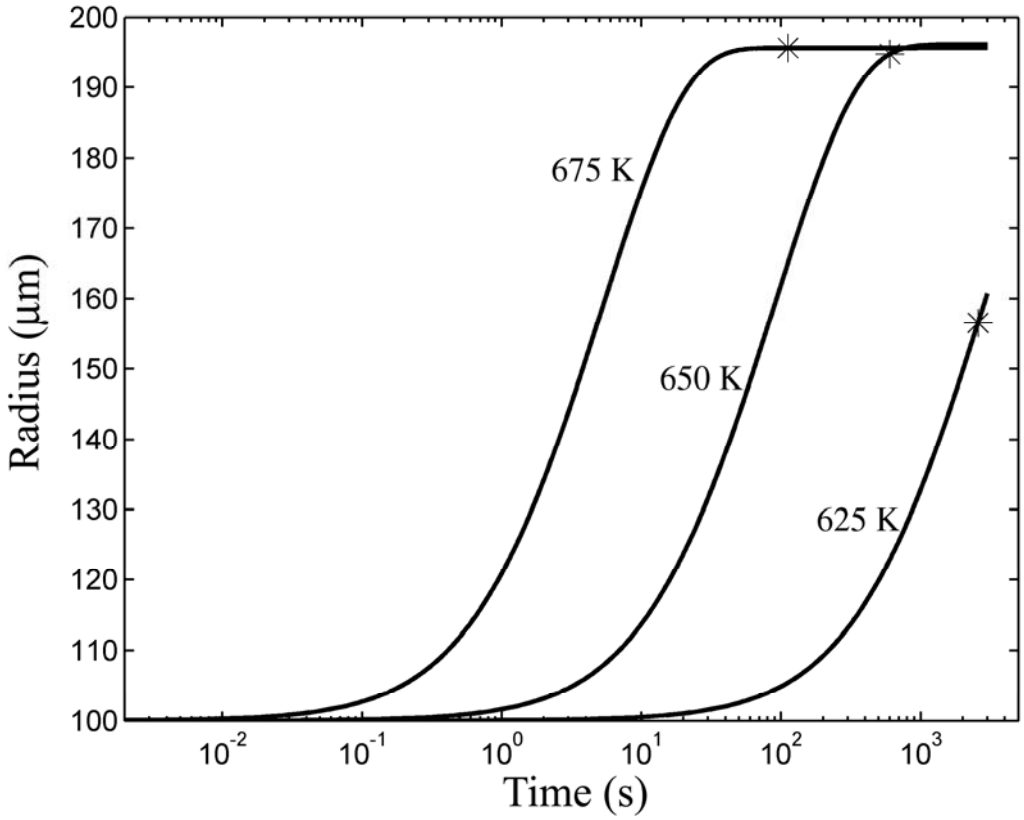

Figure 4. Expansion evolution of a 100 mm radius bubble initially at p_i = 105 Pa expanding in undercooled $Pd_{43}Ni_{10}Cu_{27}P_{20}$ liquid at p_∞ = 1 Pa and temperatures of 625 K, 650 K, and 675 K. The onset of crystallization at each temperature is marked with an asterisk.

Additionally, the model is utilized to explore the effect of initial gas pressure on bubble expansion. The same conditions as above were used. The computed evolutions for initial gas pressures of 0.5×10^5, 1.0×10^5, and 2.0×10^5 Pa at a temperature of 650 K are shown in Figure 5. As expected, higher initial gas pressure results in greater equilibrium bubble size, since it corresponds to greater molar quantities. The expansion kinetics at different pressures appear similar: Relaxation to equilibrium size occurs between 300-500 s in all three cases. This is attributed to the fact that the dependence of kinetics on molar quantity is very weak as compared to the dependence on viscosity. The time for the onset of crystallization at 650 K is also superimposed on the plot, suggesting that similar processing time windows exist at all pressures.

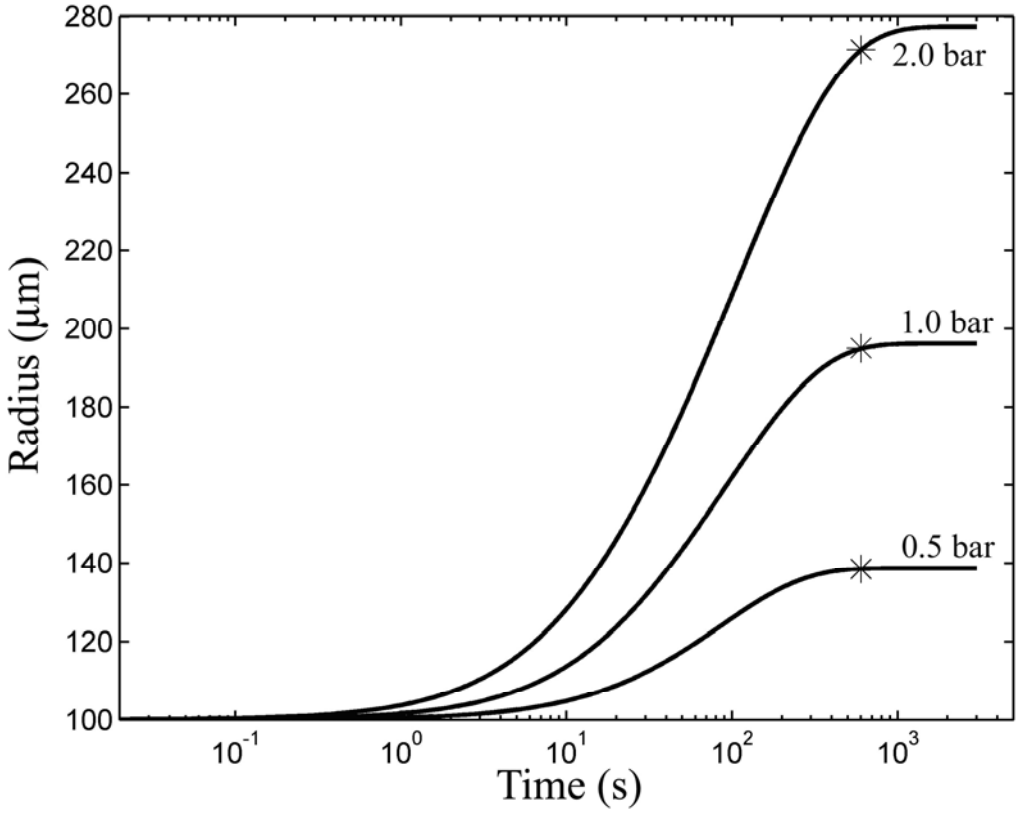

Figure 5. Expansion evolution of a 100 mm radius bubble initially at pressures of 0.5 x 10^5, 1.0 x 10^5, and 2 x 10^5 Pa expanding in undercooled $Pd_{43}Ni_{10}Cu_{27}P_{20}$ liquid at 650 K and p_∞ = 1 Pa. The onset of crystallization at 650 K is marked with an asterisk.

2.6 Conclusion

In this chapter, the pertinent issues surrounding the state-of-the-art foaming of bulk metallic glass were analyzed from scientific principles. The successful production of a homogeneous foam product benefits greatly from the controllable viscosity and ductility of the supercooled liquid state. Additionally, amorphous foams can be expanded and rendered amorphous by observing the restrictions on processing time and temperature. The advantages and limitations of BMG as a foam matrix have contributed to the development of several distinct synthesis routes, which are described in the next chapter.

2.7 References

[1] Iida T, Guthrie RIL. The Physical Properties of Liquid Metals. Oxford: Clarendon, 1988.

[2] Masuhr A, Waniuk TA, Busch R, Johnson WL. Time scales for viscous flow, atomic transport, and crystallization in the liquid and supercooled liquid states of $Zr_{41.2}Ti_{13.8}Cu_{12.5}Ni_{10.0}Be_{22.5}$. Phys. Rev. Lett. 1999;82:2290.

[3] Peker A, Johnson WL. A Highly Processable Metallic-Glass - $Zr_{41.2}Ti_{13.8}Cu_{12.5}Ni_{10.0}Be_{22.5}$. Appl. Phys. Lett. 1993;63:2342.

[4] Inoue A, Nishiyama N, Matsuda T. Preparation of bulk glassy $Pd_{40}Ni_{10}Cu_{30}P_{20}$ alloy of 40 mm in diameter by water quenching. Mater. Trans. JIM 1996;37:181.

[5] Kang J, Johnson WL, Peker A, Schroers J, Veazey C, Demetriou MD. Foamed structures of bulk-solidifying amorphous alloys. U.S. Patent Application 20040035502. 2004.

[6] Schroers J, Johnson WL, Veazey C, Demetriou MD. Production of amorphous metallic foam by powder consolidation. International Provisional Patent Application PCT WO 2004/076099 A2. 2003.

[7] Schroers J. The superplastic forming of bulk metallic glasses. JOM 2005;57:35.

[8] Inoue A, Zhang T. Novel superplasticity of supercooled liquid for bulk amorphous alloys. Superplasticity in Advanced Materials - Icsam-97, vol. 243-. 1997. p.197.

[9] Schroers J, Veazey C, Johnson WL. Amorphous metallic foam. Appl. Phys. Lett. 2003;82:370.

[10] Schroers J, Veazey C, Demetriou MD, Johnson WL. Synthesis method for amorphous metallic foam. J. Appl. Phys. 2004;96:7723.

[11] Demetriou MD, Veazey C, Schroers J, Hanan JC, Johnson WL. Expansion Evolution During Foaming of Amorphous Metals. Proc. RQ12 (Aug. 2005). Mat. Sci. Eng.: A 2005.

[12] Demetriou MD, Veazey C, Schroers J, Hanan JC, Johnson WL. Thermo-plastic Expansion of Amorphous Metallic Foam. Proc. Ismanam '05 (Jul. 2005). J. Alloys. Comp., 2005.

[13] Kui HW, Greer AL, Turnbull D. Formation of Bulk Metallic-Glass by Fluxing. Appl. Phys. Lett. 1984;45:615.

[14] Schroers J, Wu Y, Johnson WL. Heterogeneous influences on the crystallization of $Pd_{43}Ni_{10}Cu_{27}P_{20}$. Philos. Mag. A 2002;82:1207.

[15] Brothers AH, Dunand DC. Syntactic bulk metallic glass foam. Appl. Phys. Lett. 2004;84:1108.

[16] Brothers AH, Dunand DC. Ductile bulk metallic glass foams. Adv. Mat. 2005;17:484.

[17] Fan GJ, Fecht HJ, Lavernia EJ. Viscous flow of the $Pd_{43}Ni_{10}Cu_{27}P_{20}$ bulk metallic glass-forming liquid. Appl. Phys. Lett. 2004;84:487.

[18] Elzey DM, Wadley HNG. The limits of solid state foaming. Acta. Mater. 2001;49:849.

[19] Saotome Y, Itoh K, Zhang T, Inoue A. Superplastic nanoforming of Pd-based amorphous alloy. Scr. Mater. 2001;44:1541.

[20] Poritsky H. The Collapse or Growth of a Spherical Bubble or Cavity in a Viscous Fluid. Proc. of the First U.S. Nat. Congress Appl. Mech., ASME, 1952. p. 813.

[21] Rayleigh L, Strutt JW. Philos. Mag. 1917; 34.

[22] Egry I, Lohofer G, Seyhan I, Schneider S, Feuerbacher B. Viscosity and surface tension measurements in microgravity. Int. J. Thermophys. 1999;20:1005.

[23] Schroers J, Wu Y, Busch R, Johnson WL. Transition from nucleation controlled to growth controlled crystallization in $Pd_{43}Ni_{10}Cu_{27}P_{20}$ melts. Acta. Mater. 2001;49:2773.

CHAPTER 3

AMORPHOUS METALLIC FOAM SYNTHESIS

3.1 Introduction

Several synthesis routes for amorphous metallic foam have been invented[†]. Discovered in 2002, it was termed alpha-foam to identify it as a single-step process to produce an expanded foam. This method involved foam expansion near the liquidus. In 2004, further refinement on the alpha-foam process improved cellular homogeneity by controlling foaming temperature and expansion rate.

Research in 2003 led to beta-foam, named for its two step process involving a distinct prefoaming stage and an expansion stage. To investigate the effects of microgravity on beta-foam expansion, an experiment was conducted with NASA onboard the International Space Station in July 2005 (see Appendix I). The potential of BMG foam as an expandable space structure was evaluated. Additional research in 2004 on beta-foam led to controlled foaming experiments that demonstrated the cellular morphology evolution.

Research in 2005 created a gamma-foam by utilizing a three-step process that begins with amorphous powder, then hot powder compaction to form a prefoam, followed by an expansion stage (see Appendix II). Additional research was conducted on the mechanical air-entrainment technique (see Appendix III). The gamma-foam method

[†] Patent pending on "Foamed structures of bulk-solidifying amorphous alloys" (US04/001575).

and mechanical air-entrainment technique are promising for future foaming of commercial BMG alloys.

Experimental methods employed for the preparation of the alloy, prefoaming, and foam expansion are presented in the following sections. All synthesis routes involve expanding entrained gas bubbles at a temperature between the liquidus and the glass transition. Each synthesis route, with its advantages and limitations, will be described in this chapter. Chosen for its chemically inert nature and thermodynamic stability, the alloy utilized for foam synthesis development was $Pd_{43}Ni_{10}Cu_{27}P_{20}$.

3.2 Experimental alloying procedure of $Pd_{43}Ni_{10}Cu_{27}P_{20}$

The alloy $Pd_{43}Ni_{10}Cu_{27}P_{20}$ ingot is prepared by first pre-alloying Pd (99.9% purity), Ni (99.9% purity), and Cu (99.99% purity) by induction melting in a quartz tube into a master alloy. The second step involves slowly alloying P (99.9999% purity) with the master alloy by step-wise furnace heating in a hermetically sealed quartz tube. This approach is beneficial for three reasons. First, phosphorus cannot be alloyed directly with Pd, Ni, and Cu due to the large difference in melting points. Second, phosphorus vapor cannot escape from the closed vesselm, which allows for precise determination of alloy mass. Based on experimental results, additional phosphorus should be added to achieve the correct composition because some phosphorus may oxidize and not alloy. Third, adding pure phosphorus in a second step avoids the use of phosphorus compounds such as Ni_2P with typically lower purity than commercially received. In a final step, fluxing of the alloy by B_2O_3 is necessary to improve the alloy's undercooled liquid thermodynamic stability. Fluxing is performed by induction melting the

$Pd_{43}Ni_{10}Cu_{27}P_{20}$-completed alloy on a bed of high-purity B_2O_3 in a quartz tube for 1200 s at 1200 K, followed by water quenching.

3.3 Alpha-foam experimental procedure

Prefoam procedure: This section reports on the first synthesis method to foam $Pd_{43}Ni_{10}Cu_{27}P_{20}$. First, the alloy is prefoamed by induction melting the alloy over the blowing agent hydrated boron oxide at an external pressure such as 1 bar. During the prefoaming process, a large number of water-vapor bubbles are released from the blowing agent into the liquid alloy at 1100 K. The morphology of a final foam product should exhibit narrow bubble size distribution as well as uniform spatial distribution of bubbles. It is therefore critical that the prefoam morphology also possess those size and spatial distribution characteristics, so that it can evolve into a desirable foam product.

Foam procedure: Immediately after prefoaming, the sample temperature is lowered to the alloy's liquidus of 860 K. Foaming is then triggered by reducing the external pressure. The water-vapor bubbles grow and attain an equilibrium size, resulting in a low-density closed-cell foam. By water quenching, the foam is rendered amorphous. The method is shown schematically in Figure 1. Differential scanning calorimetry (DSC) measurements were carried out to confirm the amorphous nature of the foam. Thermal analysis to confirm the amorphous nature of the foam was performed in a Perkin Elmer DSC 7 and a Netzsch Pegasus DSC 404C.

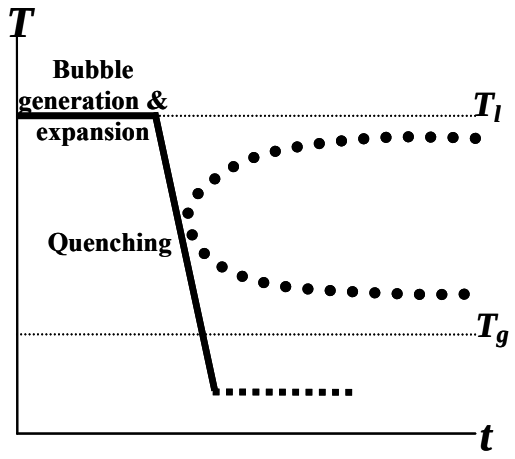

Figure 1. Alpha-foam method utilizes bubble creation and expansion in the liquid state and subsequent quench of the foamed liquid to its amorphous state. Symbols T_l and T_g denote liquidus and glass transition temperatures respectively.

3.4 Alpha-foam results and discussion

The lowering of the external pressure results in the foaming of the alloy. After 20 s, when the material reaches its maximum foam height, it is water quenched. The resulting structure is shown in Figure 2. The density of this foam is 2.2×10^3 kg/m^3 compared to 9.1×10^3 kg/m^3 for the bulk $Pd_{43}Ni_{10}Cu_{27}P_{20}$ sample [1]. The bubbles vary in diameter between 10^{-4} m and 10^{-3} m. A very uniform bubble distribution can be observed without a noticeable gradient from top to bottom.

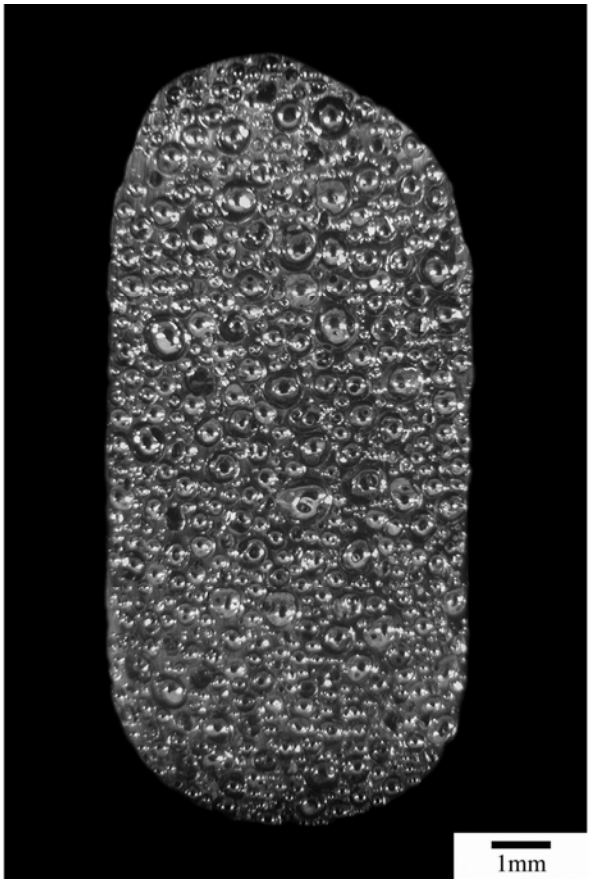

Figure 2. $Pd_{43}Ni_{10}Cu_{27}P_{20}$ foam prepared from the prefoam by decreasing the pressure at the liquidus temperature to 10^{-2} mbar. The bubbles vary in size between 100 microns and 1 mm. The density of this foam is 2.2 g/cm^3 which is 24% of the density of $Pd_{43}Ni_{10}Cu_{27}P_{20}$.

In order to determine whether the foam can be vitrified upon cooling, thermal analysis is performed by heating at a rate of 0.33 K/s. The thermograms for the prefoam and foam are shown in Figure 3. Both thermograms look very similar and the fact that T_g and T_x are not altered by the foaming process indicates that the foaming does not degrade the glass-forming ability. The heat of crystallization measured for the prefoam and foam is similar, indicating the final foam product is entirely amorphous.

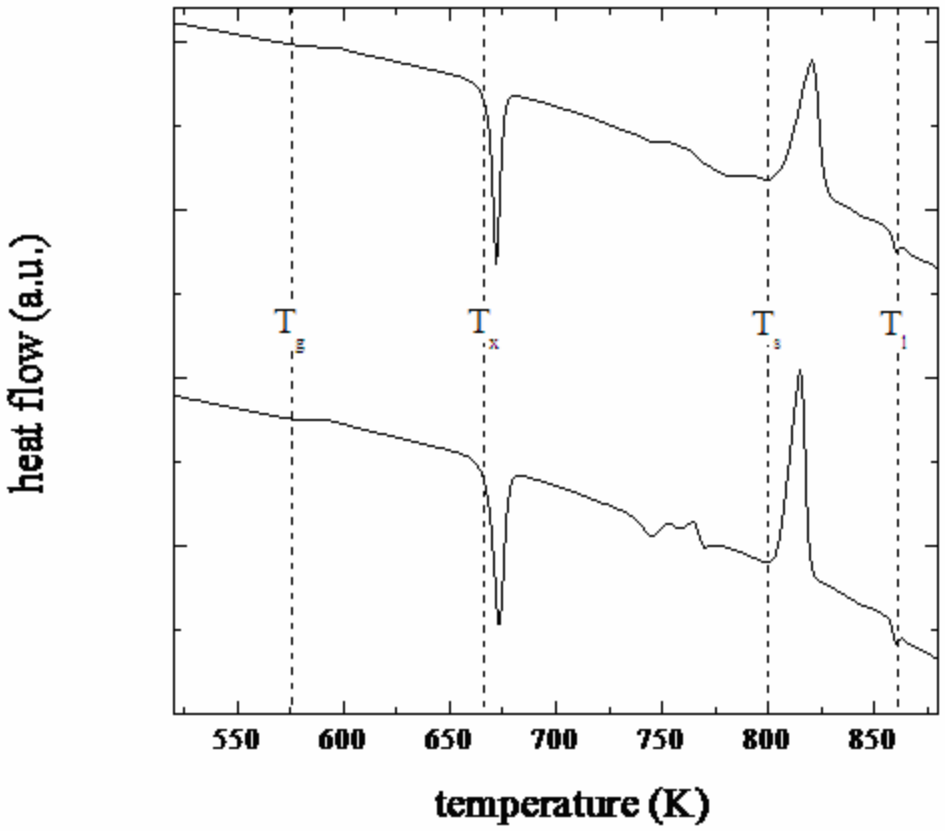

Figure 3. DSC thermograms of heating experiments with 20 K/min. The bottom thermogram was obtained for the prefoam material and the top thermogram for the foamed material. For the prefoam material Tg = 578 K, Tx = 667 K, $\Delta H = 3 \times 10^3$ J/mol, T_s = 804 K and T_l = 859 K have been measured. Almost identical values of Tg = 577 K, Tx = 666.8 K, $\Delta H = 2.9 \times 10^3$ J/mol, T_s = 804 K and T_l = 858 K are determined for the foam.

3.5 Alpha-foam conclusion

For the first time, the bulk metallic glass forming alloy $Pd_{43}Ni_{10}Cu_{27}P_{20}$ was processed into amorphous foam. The homogeneity of the foam is a result of a very low sedimentation velocity due to the high viscosity at the alloy's liquidus. The resulting foams have densities as low as 1.4 g/cm^3 with a homogeneous distribution of bubbles of a

size range between 200 μm and 1 mm. Further research will demonstrate the improvements attainable by foaming in the undercooled liquid.

3.6 Refined alpha-foam experimental procedure

The refined alpha-foam method employs foam expansion in the undercooled liquid region. Although prefoam processing is similar to the original alpha-foam method, the blowing agent boric acid (H_3BO_3) was utilized because it releases more water vapor than hydrated boron oxide. A greater amount of water vapor allows for a larger foam expansion capability. The alloy $Pd_{43}Ni_{10}Cu_{27}P_{20}$ along with the blowing agent (10% by mass boric acid (H_3BO_3) powder) was enclosed in a quartz tube under argon at 1 bar. After inductively melting the alloy at approximately 1175 K for 90 s, a bubbly liquid mixture was generated by the decomposing blowing agent. The quartz tube containing the liquid mixture was then immersed in molten tin at 693 K, and was settled for approximately 30 s to attain thermal equilibration in the undercooled liquid state. Pressure was then slowly removed over a period of 60–90 s. The expanded foam was subsequently water quenched. The foam porosity by this method was controlled by the amount of pressure removed during foaming. Porosity was measured by the Archimedes or graphical method.

3.7 Refined alpha-foam results and discussion

The goal of refining the alpha-foam method was to produce higher porosity foam (up to 90%) with a high degree of homogeneity. A processing window in which the undercooled liquid can exhibit high ductility yet low fluidity can be regarded as ideal

with respect to maximizing foam expansion. Unfortunately, such an ideal processing window is predicted to exist in the vicinity of the TTT nose, where crystallization kinetics peak and configurational freezing to the glassy state becomes most challenging. Nevertheless, a kinetically robust supercooled liquid exhibiting adequate stability at the TTT nose may allow sufficient time for foaming under such optimum processing conditions.

Experimentation led to an optimal temperature and pressure reduction for foaming. Consider the TTT diagram of $Pd_{43}Ni_{10}Cu_{27}P_{20}$ [2] presented in Figure 4. In this diagram, processing times of 200 s are indicated in the vicinity of the nose. The temperature of 693 K appears to be particularly attractive for foam processing, as the liquid at that temperature is expected to exhibit relatively low fluidity but adequately high ductility, as determined by the estimates derived below.

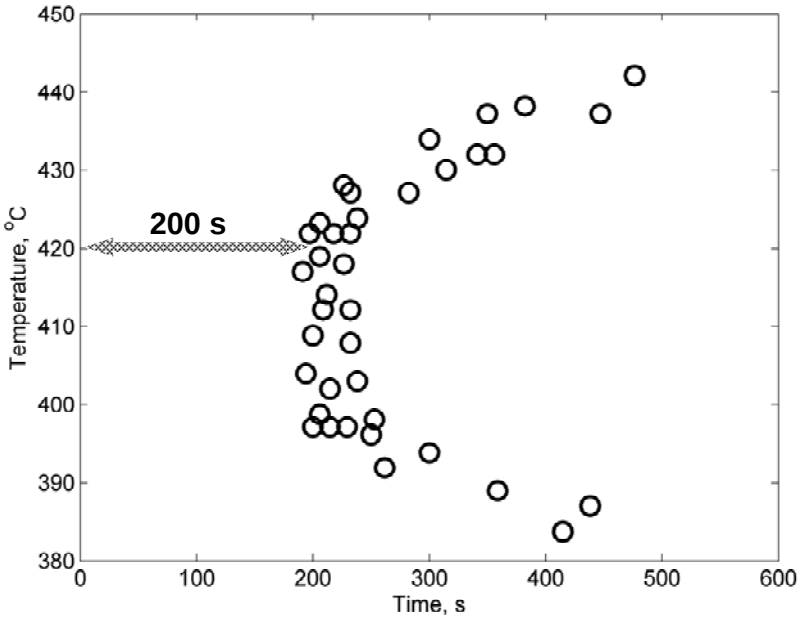

Figure 4. TTT (Time-Temperature-Transformation) diagram of $Pd_{43}Ni_{10}Cu_{27}P_{20}$ from [Schroers J, Johnson WL, Busch R. Appl. Phys. Lett. 2000; 77, 1158]. A 200-s processing time window is indicated at 420 °C, which can be utilized for foam expansion.

The temperature-dependent viscosity of supercooled $Pd_{43}Ni_{10}Cu_{27}P_{20}$ liquid is presented in Figure 5. By extrapolation, the liquid viscosity at 693 K is estimated to be ~1×10^4 Pa-s. At this temperature, the sedimentation velocity of a 1 mm water-vapor bubble (at 1 atm) can be estimated from Stokes law to be ~3 μm/s. This suggests that for 30 s foam processing time, sedimentations of less than 100 μm would be realized, which implies that the morphological dynamics of the foam at 693 K would be nearly frozen.

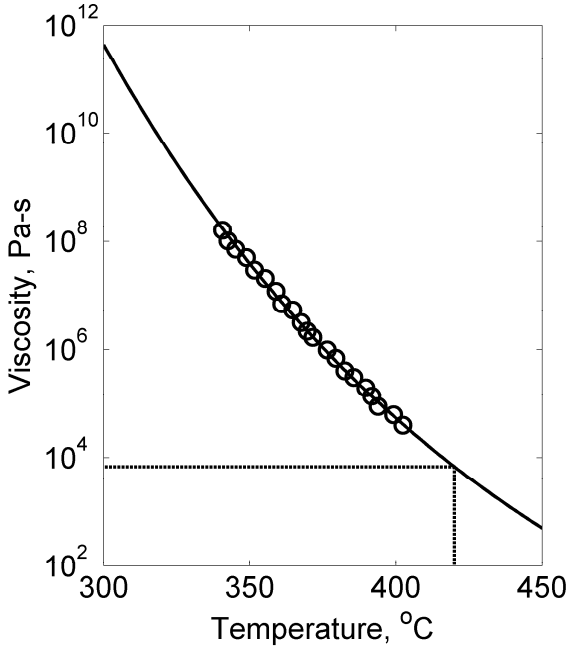

Figure 5. Temperature dependent viscosity of $Pd_{43}Ni_{10}Cu_{27}P_{20}$ liquid from [Fan GJ, Fecht HJ, Lavernia EJ, Appl. Phys. Lett. 2004; 84: 487.]. By extrapolation, the liquid viscosity at 420 °C is estimated to be 1 x 10^4 Pa-s.

For temperatures below the TTT nose, the limiting strain rates to maintain Newtonian flow conditions (under which liquid can exhibit ideal ductility) are presented in Figure 6 [3]. By linear extrapolation, the limiting strain rate at 693 K can be estimated to be ~1 s^{-1}. This strain-rate limit is orders of magnitude higher than those corresponding to temperatures below the TTT nose. This suggests that at 693 K, Newtonian flow

conditions (and hence ideal liquid ductility) can be maintained under higher foaming rates.

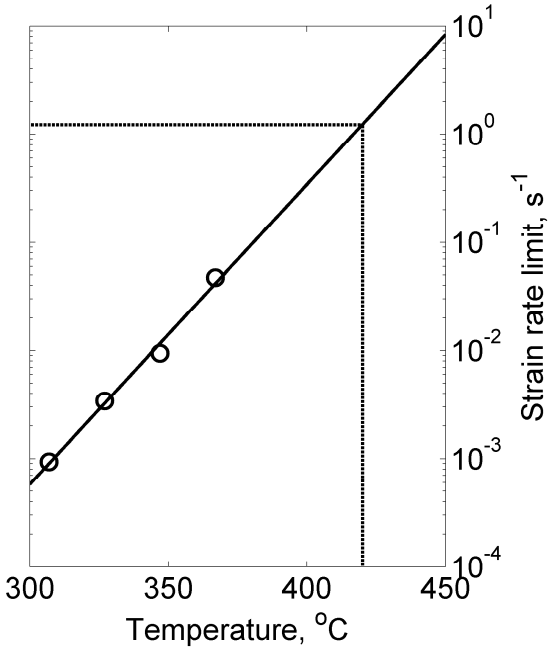

Figure 6. Limit of strain-rate sensitivity of $Pd_{43}Ni_{10}Cu_{27}P_{20}$ liquid at different temperatures from [Saotome Y, Itoh K, Zhang T, Inoue A. Scr. Mater. 2001;44:1541.]. By extrapolation, the strain rate limit to maintain Newtonian flow at 420 °C is estimated to be ~1 s^{-1}.

Therefore, these simple estimates establish that the optimum foaming temperature for $Pd_{43}Ni_{10}Cu_{27}P_{20}$ would be 693 K. An amorphous metallic foam of 87% porosity produced by this method is shown in Figure 7 beside an alloy button having the same mass as the foam. The inset panel shows the x-ray diffractogram that displays the amorphous nature of the foam. Amorphous foams with porosities up to 91% were produced by this synthesis method. In Figure 8, optical micrographs depicting a cross section of the foam at different magnifications are presented. The cellular structure is shown to exhibit homogeneity as well as cell-size uniformity. Furthermore, cells are shown to be separated by intracellular membranes having thicknesses on the order of a

few microns. These micro-membranes are essentially products of a foam expansion process in which large plastic elongations were realized. This implicitly verifies that Newtonian flow conditions dominated during foaming, which gave rise to near ideal ductility and led to large plastic elongations. It is also worth noting that cell-size gradients along the gravity direction are found to be rather small (average cell sizes are found to vary by approximately 1% per mm of length). This supports the idea that sedimentation during foaming was adequately suppressed, as predicted.

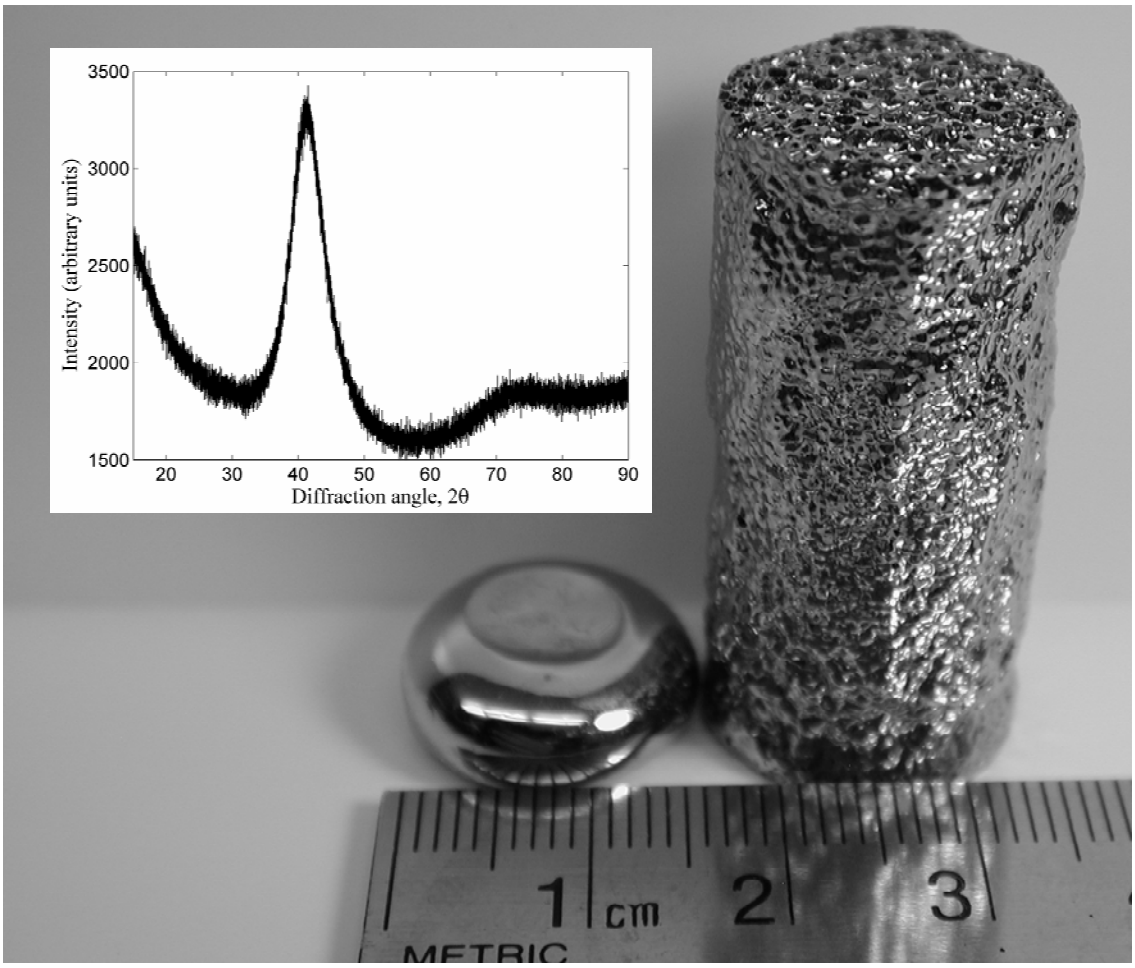

Figure 7. 87%-porosity foam produced by the refined beta-foam method. In the insert, the x-ray diffractogram verifying the amorphous nature of the foam is presented. A button of the pore-free alloy having the same mass as the foam is also shown, in order to demonstrate the nearly 10-fold increase in volume produced by foaming.

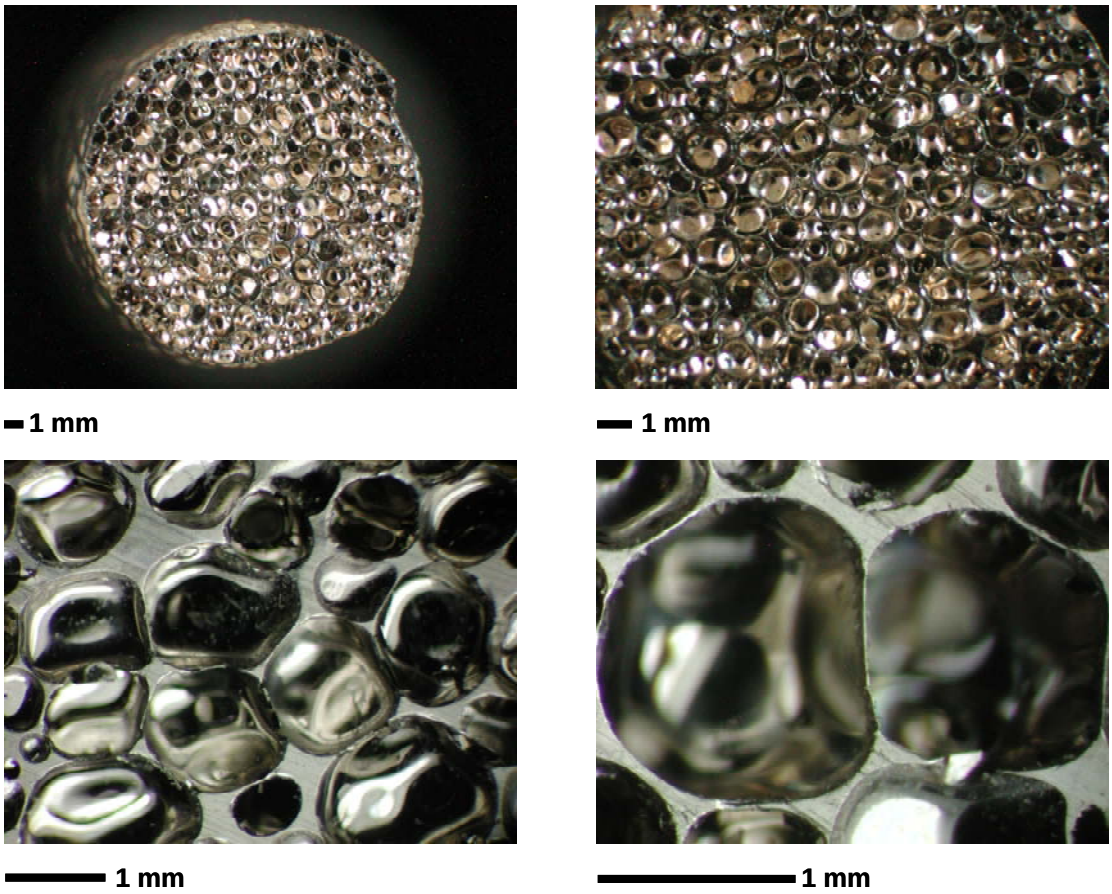

Figure 8. Optical micrographs depicting a cross section of the foam at different magnifications. The cellular structure exhibits homogeneity as well as cell-size uniformity. Cells are separated by intracellular membranes having thicknesses on the order of few microns.

3.8 Refined alpha-foam conclusion

The foaming temperature of the refined alpha-foam method has been optimized through experimentation. Additionally, the refined alpha-foam method takes advantage of foaming in the undercooled liquid. However, as stated previously, the predicted optimal foaming temperature falls at the TTT nose, where crystallization kinetics peak. Despite this fact, amorphous BMG foams have been produced with no crystallization observed. The refined alpha-foam synthesis produces foams with higher porosity due to low fluidity, and with greater homogeneity due to Newtonian flow during expansion.

3.9 Beta-foam experimental procedure

Prefoam for the beta-foam method is produced by using the same methods as for the alpha-foam method described in Section 3.3. The main difference is that all prefoams are water quenched before continuing to the second foam expansion step. $Pd_{43}Ni_{10}Cu_{27}P_{20}$ is mixed with 50% by volume of hydrated boron oxide and was processed in a quartz tube at 1170 K for 5 min under argon atmosphere at 2 bar external pressure. An increased external pressure of 2 bar was utilized to investigate its effect on reducing prefoam bubble size. After being processed, the prefoam was water quenched to its amorphous state. The $Pd_{43}Ni_{10}Cu_{27}P_{20}$ prefoam produced is shown in Figure 9. The prefoam consists of 15 vol% bubbles homogeneously distributed throughout the sample having an average size of 70 μm. Its amorphous nature was confirmed by thermal analysis.

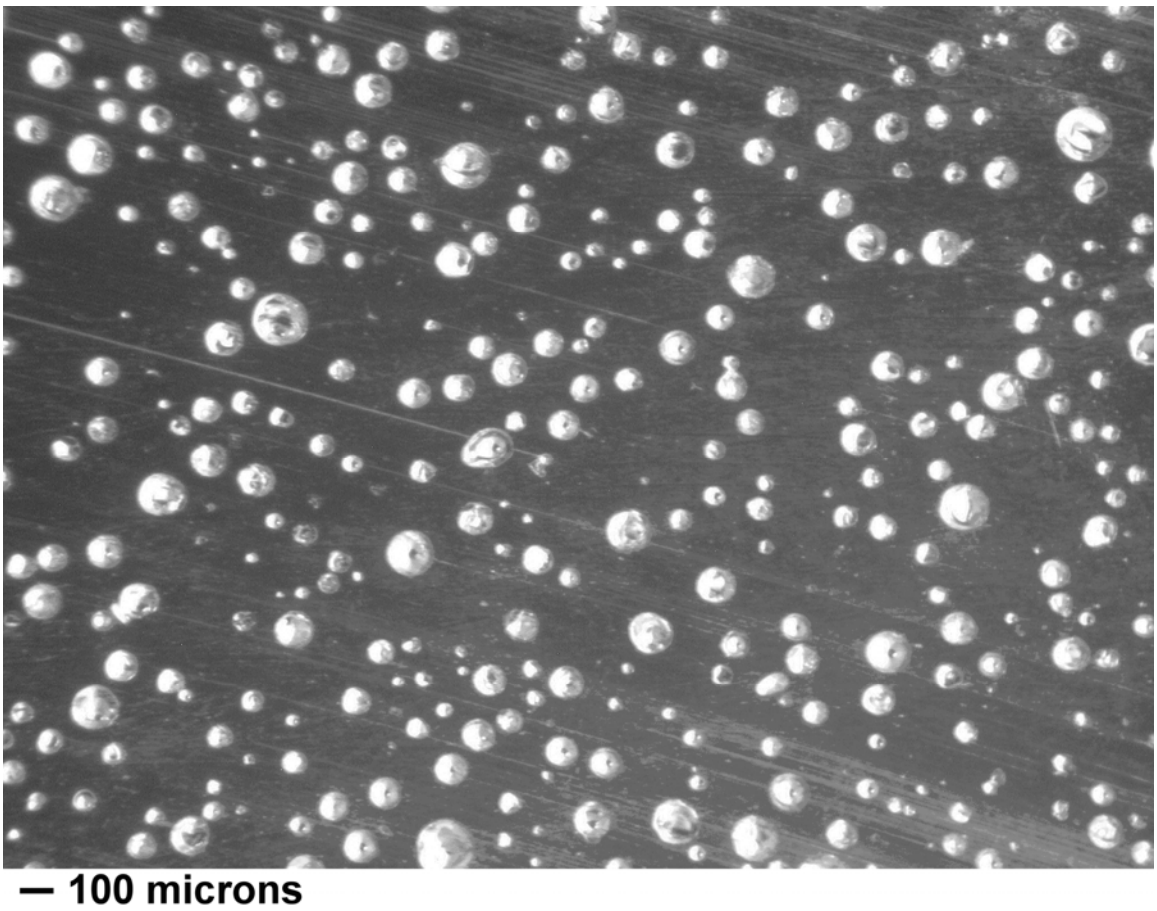

Figure 9. $Pd_{43}Ni_{10}Cu_{27}P_{20}$ prefoam processed for 5 min at 2-bar pressure and 1170 K. It consists of 15-vol% bubbles homogeneously distributed throughout the prefoam with an average bubble size of 70 mm.

Foam expansion: In the beta-foam method, the prefoam is water quenched to its amorphous state. Prefoams were heated into the supercooled liquid region by means of a compact-resistance heater, or alternatively by an RF coil. The samples were then annealed at a given temperature in the supercooled region and foam expansion was activated by reducing the external pressure. The external pressures imposed in the foaming stage were on the order of 10^{-3} mbar.

3.10 Beta-foam results and discussion

The beta-foam synthesis method utilizes the thermodynamic stability and thermoplastic formability of the supercooled liquid state. In this method, the constraints dictated by the critical cooling rate are removed such that low-density amorphous foams in dimensions that are not limited to the critical casting thickness can be produced. The unique characteristics of the supercooled liquid state can be utilized to develop a three-step manufacturing method for producing amorphous metallic foams. The first step involves the generation of a large number of small bubbles into the equilibrium liquid under pressure to produce a prefoam having a small bubble-volume fraction. The intermediate step involves quenching of the bubbly liquid to its amorphous state by cooling at rates greater than the critical cooling rate. The last step involves reheating of the sample to the supercooled liquid region and reducing the pressure to values substantially lower than those used in the prefoaming step in order to activate bubble expansion. This method is illustrated schematically in Figure 10. Since in this method bubble expansion takes place below the nose of the TTT diagram, the critical cooling rate to bypass crystallization is essentially infinite. Therefore, it becomes trivial to quench the foam from the supercooled liquid state to the amorphous state. Cooling-rate constraints on vitrification are therefore relaxed and consequently low-density amorphous foams in dimensions that are not limited to the critical casting thickness can be produced by this method.

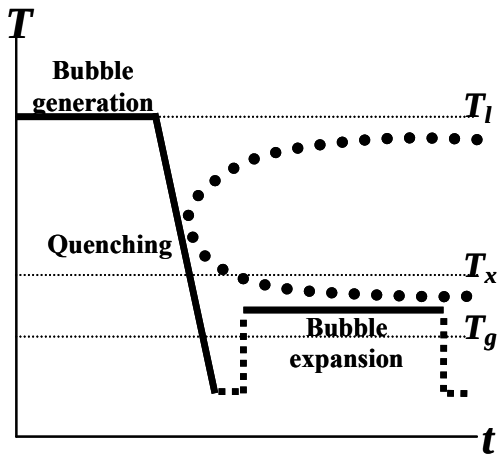

Figure 10. Proposed beta-foam method: (1) a large number of small bubbles are created in the equilibrium liquid under pressure; (2) the liquid prefoam is quenched to its amorphous state; (3) the amorphous prefoam is reheated to the supercooled liquid region and the pressure is substantially reduced to activate bubble expansion. Symbols T_l, Tx, and Tg denote liquidus, crystallization, and glass transition temperatures respectively.

Figure 11 shows a $Pd_{43}Ni_{10}Cu_{27}P_{20}$ foam exhibiting 85% bubble volume fraction. The foam was processed by RF-coil heating with a heating rate of 40 K/min. This demonstrates that production of low-density foam is possible using this synthesis method. The magnified view of this foam is shown in Figure 12. It depicts that bubbles deviate from their spherical geometry at such low densities, however bubble merging appears to be restrained by the interconnecting films. This points to a self-stabilizing mechanism between bubbles in BMG foams.

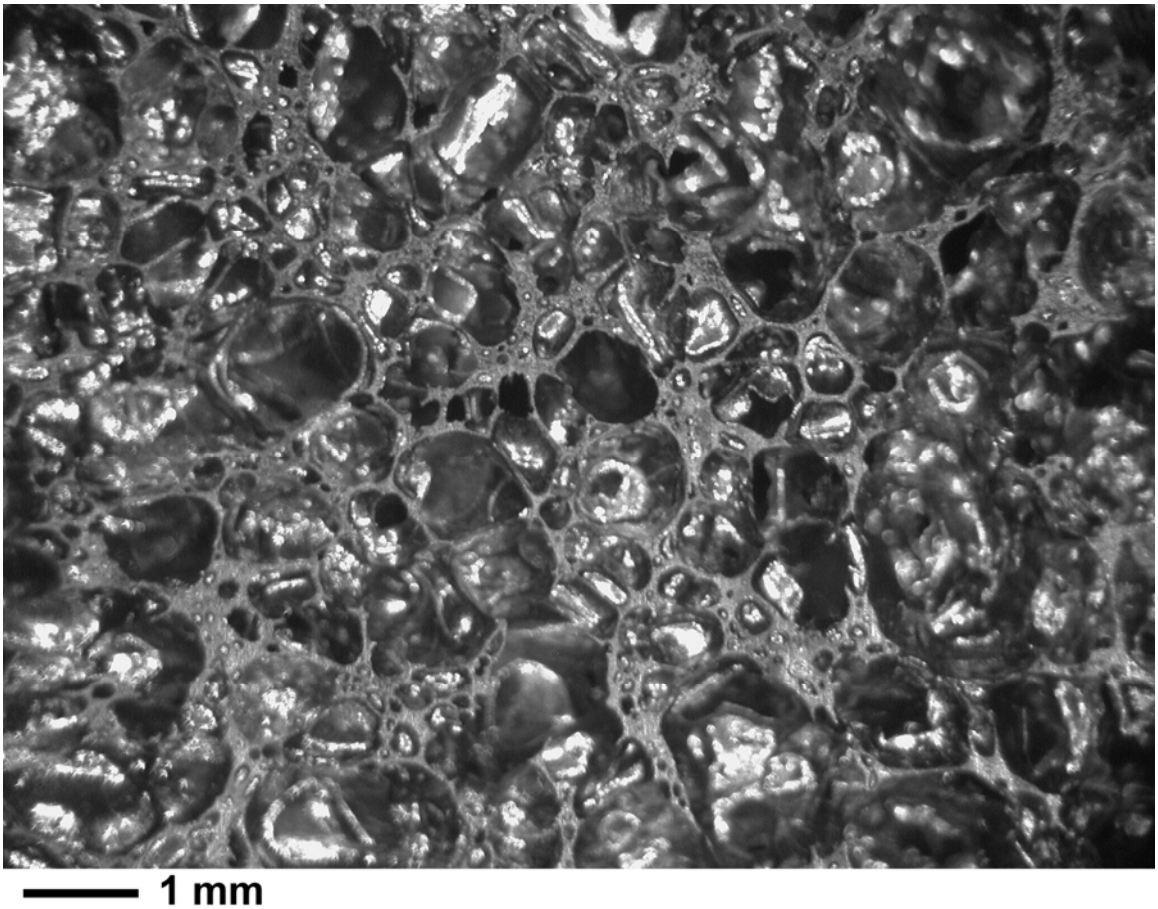

Figure 11. $Pd_{43}Ni_{10}Cu_{27}P_{20}$ foam expanded for 6 min by means of RF-coil heating. The foam exhibits a bubble volume fraction of 85%.

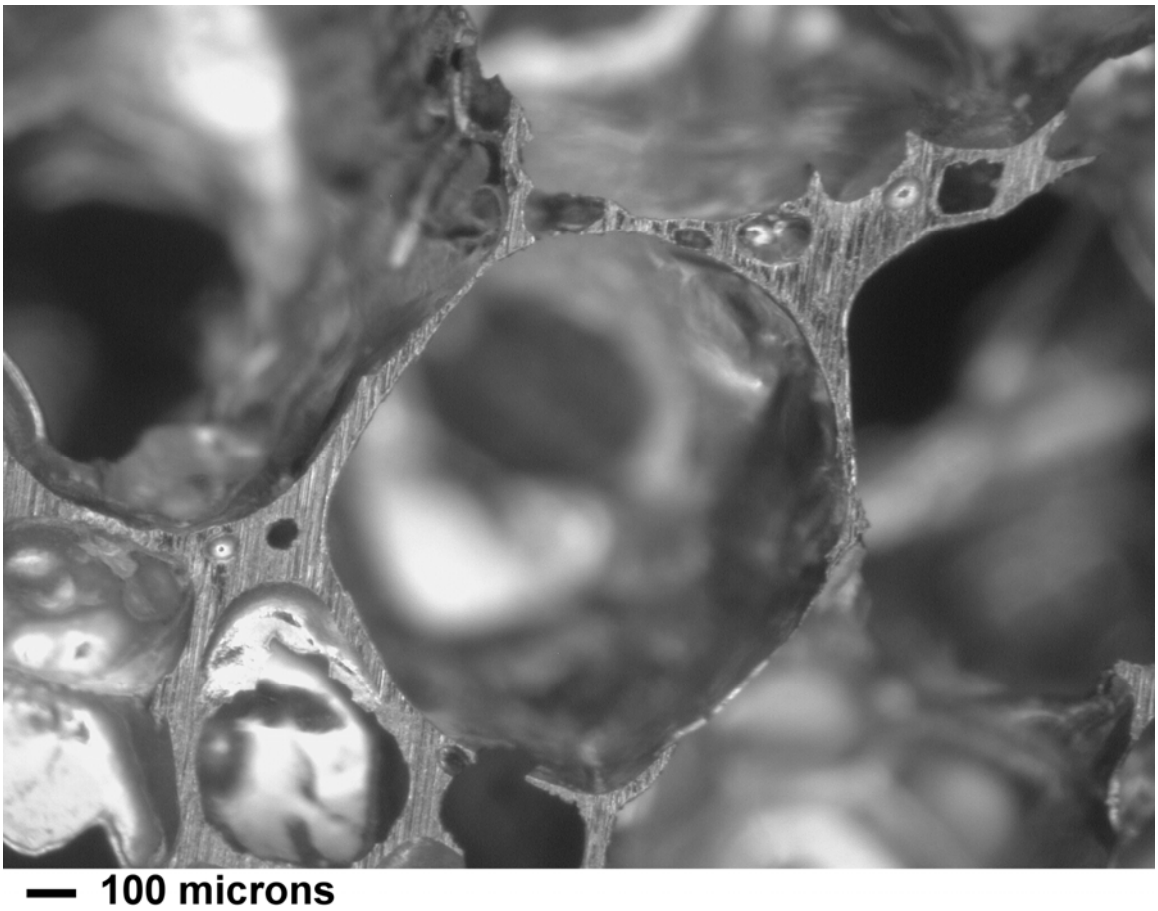

Figure 12. Magnified view. Bubbles deviate from spherical symmetry, however bubble merging appears to be restrained by the interconnecting films.

In Figure 13 a $Pd_{43}Ni_{10}Cu_{27}P_{20}$ prefoam is shown together with the corresponding expanded foam. The figure illustrates bulk expansion of the sample, which is a consequence of the foaming process employed in this synthesis method. The prefoam consisted of 10 vol% of bubbles and was processed by the gas-releasing agent method under 3-bar pressure. The expanded foam exhibits a bubble volume fraction of 75%. The amorphous nature of the foam was verified by thermal analysis.

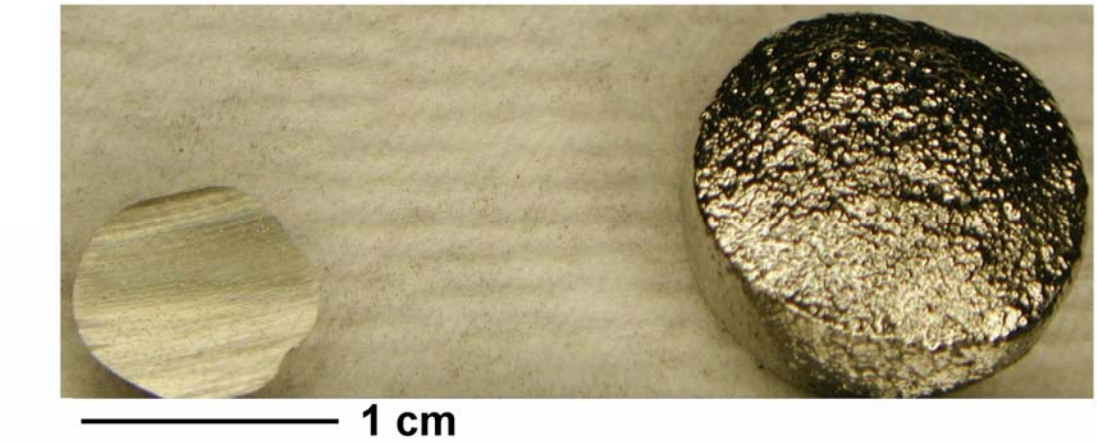

Figure 13. Size comparison of $Pd_{43}Ni_{10}Cu_{27}P_{20}$ prefoam (left) and expanded foam (right) by RF-coil. The bubble volume fraction of the prefoam is 10%, while that of the final foam is 75%.

Figure 14 shows a $Pd_{43}Ni_{10}Cu_{27}P_{20}$ prefoam along with two stages of expanded foam. The prefoam (a) consisted of 10% by volume of bubbles and was processed by the gas-releasing agent method under 3-bar pressure. Foam processing was performed by means of a compact-resistance heater. The processing time for the first stage (b) was 7.5 min, and for the second stage (c) was 30 min. The bubble volume fraction in the first expansion stage was 50%, while in the second it was 65%. Therefore, it is demonstrated that by the proposed synthesis method it is possible to expand the foam in stages, which allows controllability over the final foam density. The foam products developed by this synthesis method do not exhibit any observable density gradients attributed to bubble sedimentation. However, non-uniformities in the foam morphologies appear as a consequence of temperature gradients during foaming.

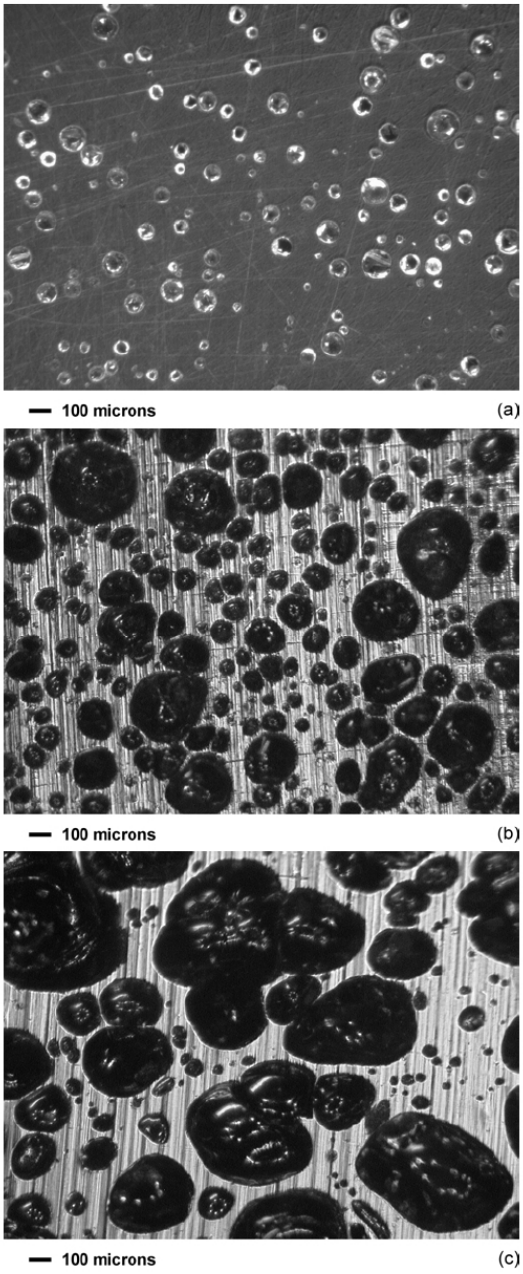

Figure 14. Microstructure growth evolution of $Pd_{43}Ni_{10}Cu_{27}P_{20}$ liquid processed by compact-resistance heating. (a) Prefoam (10-vol% bubbles). (b) Processed for 7.5 minutes (50-vol% bubbles). (c) Processed for 30 minutes (65-vol% bubbles).

3.11 Beta-foam conclusion

In the proposed synthesis method, cooling-rate constraints on vitrification are relaxed and hence amorphous metallic foams can be produced in low densities and dimensions that are not limited to the critical casting thickness. By the beta-foam method, BMG foams characterized by bubble volume fractions as high as 85% are successfully produced. The foam products do not exhibit any observable density gradients attributed to bubble sedimentation. It was also demonstrated in this study that foaming could be performed in a controlled manner such that desired foam densities can be accomplished. However, non-uniformities in the foam morphologies appear as a consequence of temperature gradients during foaming.

3.12 Refined beta-foam experimental procedure

The refined beta-foam method reduces temperature gradients during foaming by thermal equlibration of the prefoam before foaming is initiated. In this study, $Pd_{43}Ni_{10}Cu_{27}P_{20}$ foams were produced at various porosities by means of controlled thermoplastic foaming experiments in an effort to investigate the cellular structure development. The prefoam was prepared by sealing the alloy ingot along with hydrated boron oxide powder under argon atmosphere, heating to 1175 K for 10 minutes, and subsequently water quenching to produce a 25% porosity amorphous prefoam. Expansion of the prefoam was accomplished by first equilibrating to a supercooled liquid state at 635 K and subsequently reducing pressure to 10^{-3} mbar. Expansion was allowed to proceed for durations of 60, 120, and 180 seconds, and was followed by water quenching.

3.13 Refined beta-foam results and discussion

The foaming evolution depicted in Figure 15 qualitatively demonstrates the ability of this material to foam by thermoplastic-like expansion. Optical micrographs of the sectioned foam products with different magnification scales are presented in Figure 16 and Figure 17. Amorphous metallic foams of 38%, 49%, and 70% porosities were produced by expansion durations of 60, 120, and 180 seconds, respectively. This indicates that processing for longer durations produces higher-porosity foams. The amorphous nature was verified by x-ray diffraction analysis. The diffractograms are presented in Figure 18.

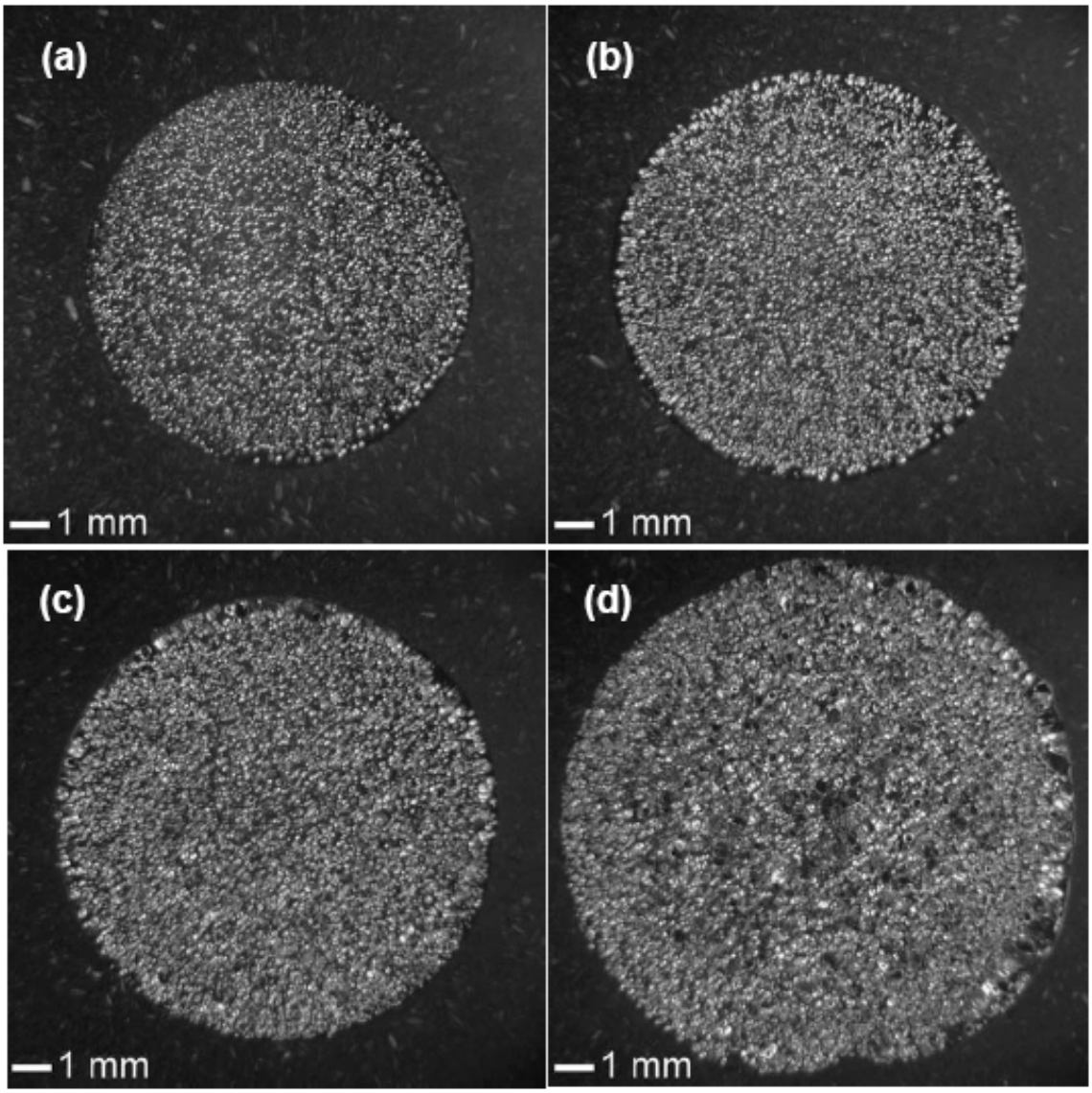

Figure 15. Optical micrographs of the sectioned foam products: (a) 25% porosity (foam precursor); (b) 38% porosity (foam expansion for 60 seconds); (c) 49% porosity (foam expansion for 120 seconds); (d) 70% porosity (foam expansion for 180 seconds).

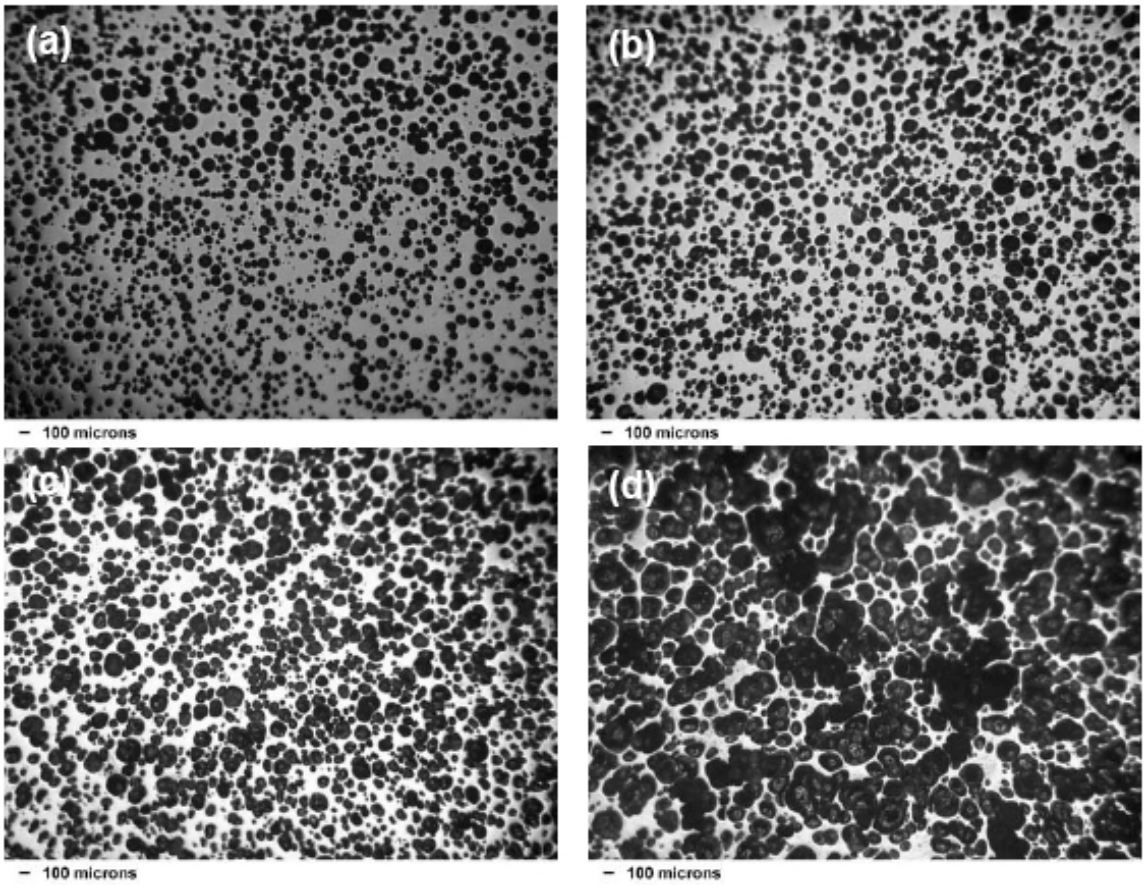

Figure 16. Optical micrographs of the sectioned foam products: (a) 25% porosity; (b) 38% porosity; (c) 49% porosity; (d) 70% porosity.

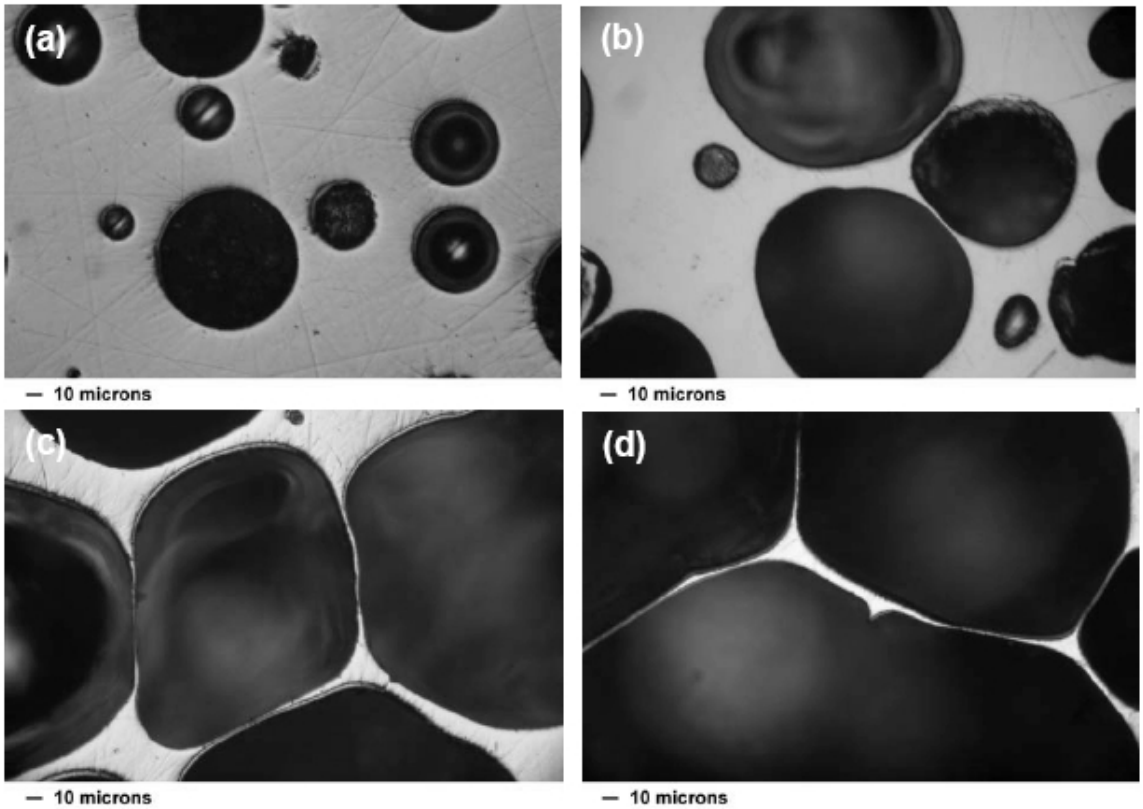

Figure 17. Optical micrographs of the sectioned foam products: (a) 25% porosity; (b) 38% porosity; (c) 49% porosity; (d) 70% porosity.

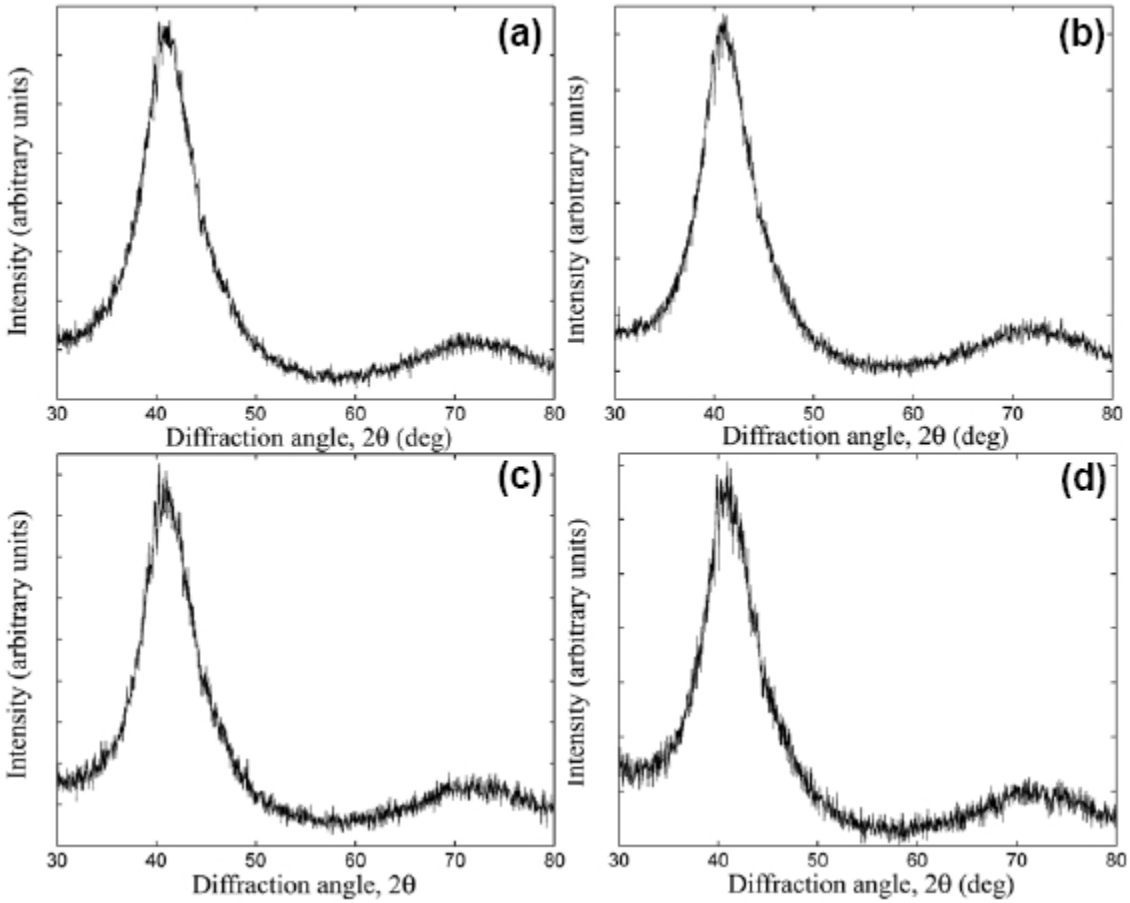

Figure 18. X-ray diffractograms of the foam products: (a) 25% porosity; (b) 38% porosity; (c) 49% porosity (d) 70% porosity.

As shown in Figure 16, the evolved cellular structures exhibit spatial homogeneity and uniformity in bubble size, which has been attributed to the high viscosity of the softened state, which dampens the foaming dynamics and enhances foaming controllability [4-6]. Closer examination of the cellular structures shown in Figure 17 reveals that foaming evolved by growth of spherically symmetric pores towards a critical porosity limit, beyond which foaming progressed by plastic stretching of intracellular membranes. This membrane-stretching expansion mechanism led to the development of a cellular structure consisting of polyhedrally arranged cells held by intracellular micro-membranes exhibiting random orientations and aspect ratios.

3.14 Refined beta-foam conclusion

The ability of amorphous metals to develop such a highly networked cellular structure by thermoplastic expansion is rather remarkable, and can be considered a significant advancement in metal foaming technology. The cellular structure is found to evolve by growth of randomly distributed spherical micro-bubbles towards polyhedral-like cells separated by microscopic intracellular membranes exhibiting random orientations and aspect ratios. The ability of amorphous metals to develop such random structural network is attributed primarily to the near-infinite ductility exhibited by their supercooled liquid state, which enables large superplastic elongations during foaming.

3.15 References

[1] Lu IR, Gorler GP, Willnecker R. Specific volume of glass-forming liquid $Pd_{43}Ni_{10}Cu_{27}P_{20}$ and related thermodynamic aspects of the glass transition. Appl. Phys. Lett. 2002;80:4534.

[2] Schroers J, Johnson WL, Busch R. Crystallization kinetics of the bulk-glass-forming $Pd_{43}Ni_{10}Cu_{27}P_{20}$ melt. Appl. Phys. Lett. 2000;77:1158.

[3] Saotome Y, Itoh K, Zhang T, Inoue A. Superplastic nanoforming of Pd-based amorphous alloy. Scr. Mater. 2001;44:1541.

[4] Schroers J, Veazey C, Demetriou MD, Johnson WL. Synthesis method for amorphous metallic foam. J. Appl. Phys. 2004;96:7723.

[5] Demetriou MD, Veazey C, Schroers J, Hanan JC, Johnson WL. Expansion Evolution During Foaming of Amorphous Metals. Proc. RQ12 (Aug. 2005). Mat. Sci. Eng.: A 2005.

[6] Demetriou MD, Veazey C, Schroers J, Hanan JC, Johnson WL. Thermo-plastic Expansion of Amorphous Metallic Foam. Proc. Ismanam '05 (Jul. 2005). J. Alloys. Comp., 2005.

CHAPTER 4

FOAM MECHANICAL PROPERTIES

4.1 Motivation and objectives

The advances in the processing of closed-cell as well as open-cell amorphous metallic foam have generated increasing interest in understanding the mechanical behavior of this emerging structural material. Foam yield strengths follow a power law derived by Ashby that scales with yield strength of the solid [1]. Data presented from a review article show the trend in Figure 1 [2]. Open-cell amorphous metallic foams exhibit impressive compressive plasticity. However, they are found to yield at low relative strengths as shown in Figure 2 [2]. Plasticity in those foams is shown to propagate by multiple non-catastrophic crushing events accompanied by monotonically increasing flow stress, possibly associated with the tendency of these open-cell foams to densify upon compression [3,4]. Their densification tendency can also explain their ability to attain such remarkable compressive plasticity.

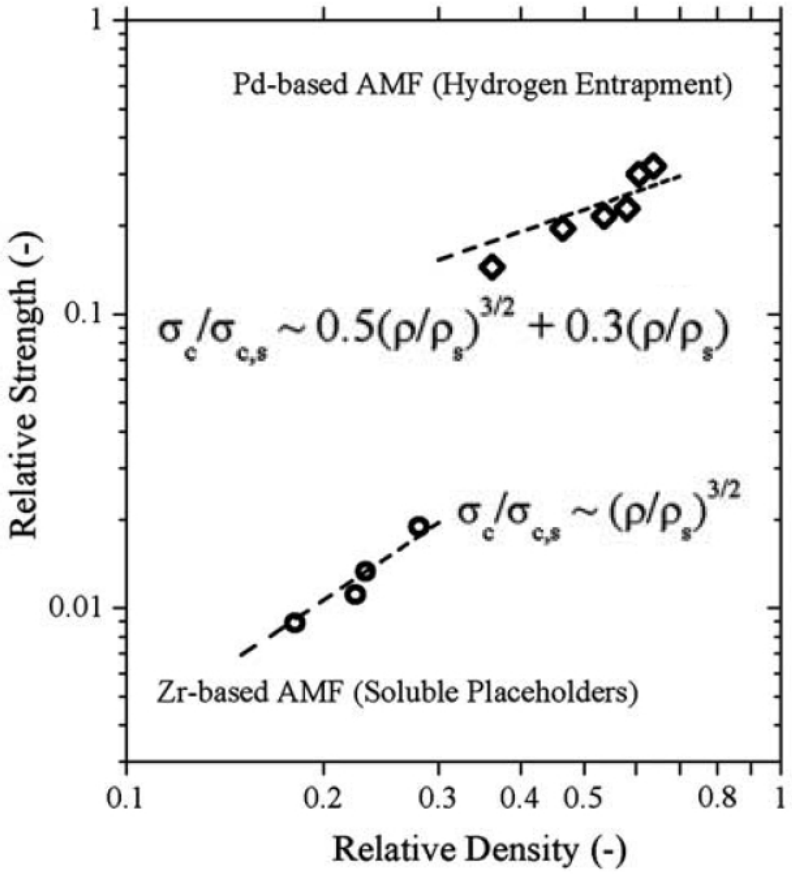

Figure 1. foam yield strength (normalized to the compressive strength of the corresponding monolithic alloy) as a function of foam relative density, for open-cell Zr-based foams with high porosity, and for closed-cell Pd-based foams with low porosity. Best fits using semi-empirical scaling laws described by Ashby et. al. [Ashby MF, Evans AG, Fleck NA, Gibson LJ, Hutchinson JW, Wadley HNG. Metal foams: a design guide. Boston (MA): Butterworth-Heinemann; 2000.] for opened- and closed-cell metal foams are also shown. Figure from [Brothers AH, Dunand DC. Scr. Mater. 2006;54:513.]

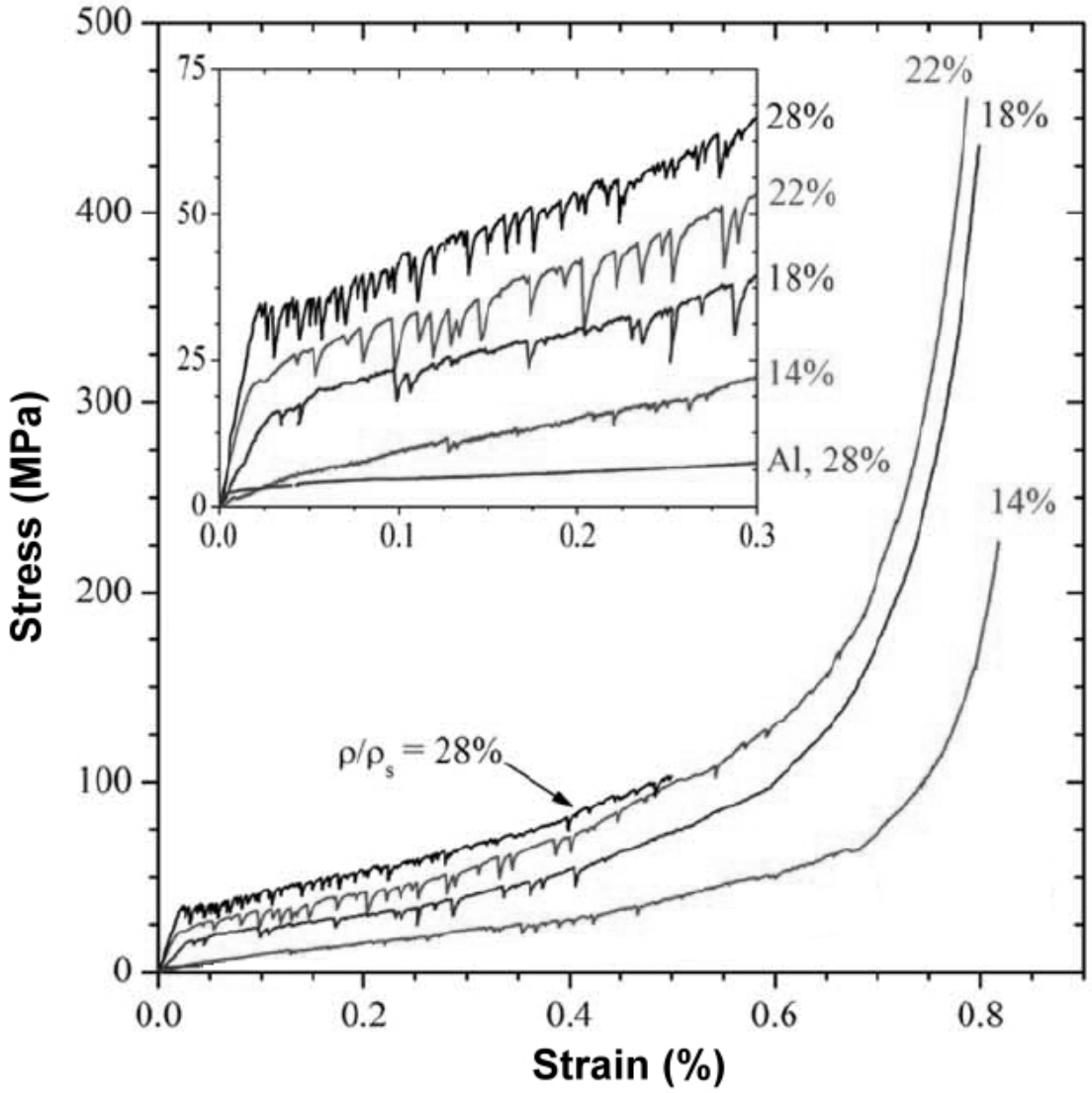

Figure 2. Engineering compressive stress–strain curves of Vit106 foams as a function of relative density for constant pore size 230 microns. Insets magnify the low-strain regions for better visualization of serrations. Figure from [Brothers AH, Dunand DC. Acta Mater 2005;53:4427.]

Conversely, closed-cell amorphous metallic foams are found to exhibit substantially higher relative strengths, but more moderate plasticity propagating by more pronounced non-catastrophic crushing events that are associated with the formation of collapse bands through the foam structure as shown in Figure 3 [2]. These events,

however, appear to be associated with monotonically decreasing flow stress, resembling the typical softening behavior of amorphous metals [5,6].

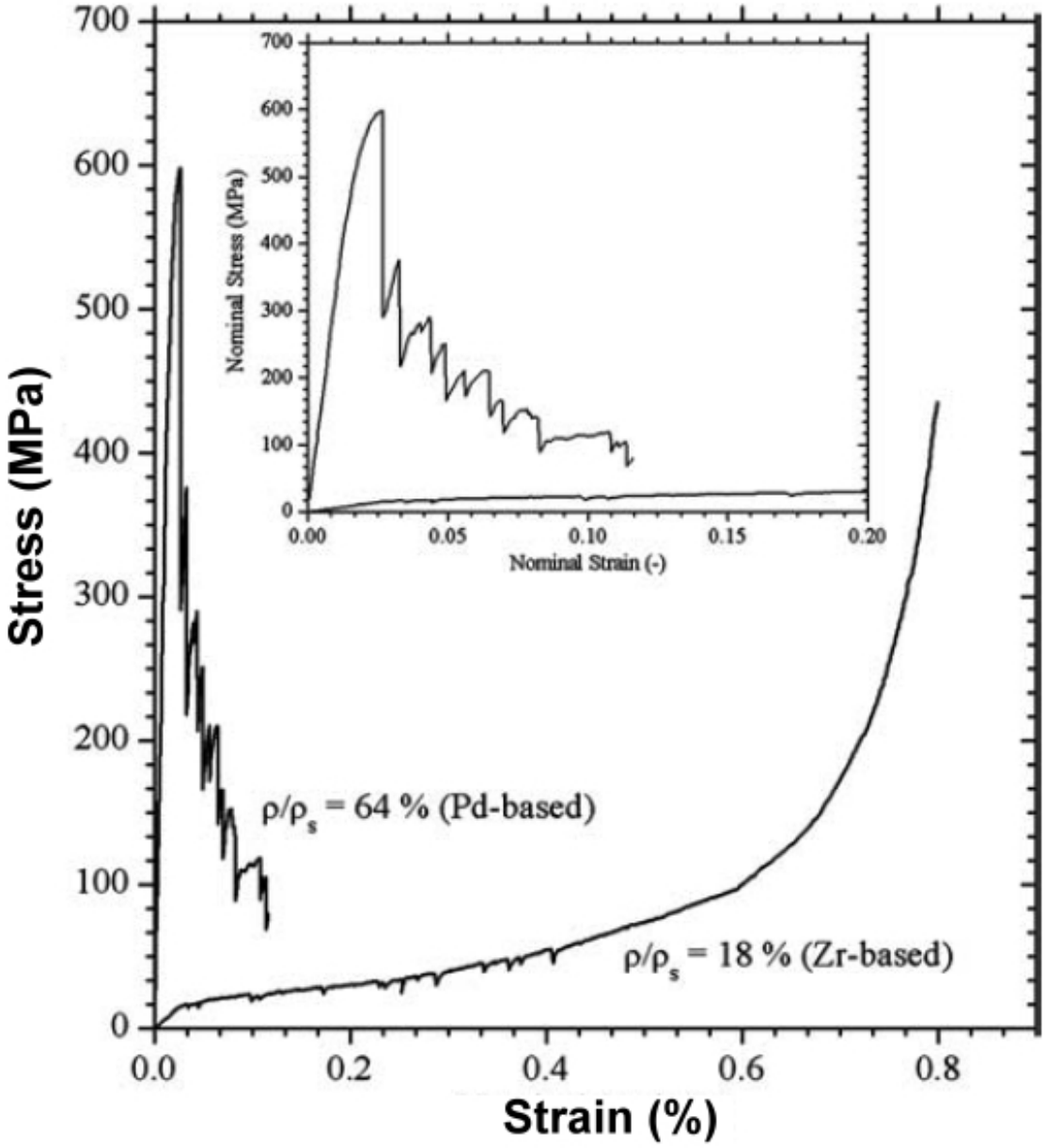

Figure 3. Published compressive mechanical properties of amorphous metal foams: Nominal stress strain curves for high-density (relative density: 64%) Pd-based foam with closed porosity [Wada T, Inoue A. Mater. Trans. JIM 2004;45:2761.] and low-density (relative density: 18%) Zr-based foam with open porosity [Brothers AH, Dunand DC. Acta Mater 2005;53:4427.]. The closed-cell foam shows high strength but comparatively small ductility, while the open-cell foam shows classical ductile metal foam behavior at much lower stresses. Figure from [Brothers AH, Dunand DC. Scr. Mater. 2006;54:513.]

4.2 Moderate-porosity-foam mechanical properties

Upon loading, moderate-porosity closed-cell amorphous metallic foams were shown to deform plastically by recurring non-catastrophic plastic collapse events (Figure 4) [5,7]. Each of these incipient collapse events is associated with the formation of a collapse band through the foam structure. Interestingly, ahead of a collapse event, these moderate-porosity foams appear to exhibit a highly nonlinear yielding response characterized by an extended stress plateau as shown in Figure 4 at porosities of 0.361 and 0.418. Furthermore, the post-collapse stiffness of these foams is shown to remain essentially unaffected, indicating good cellular-structure integrity. Recurrence of multiple self-similar collapse events is shown to result in extensive global plasticity (up to 30% strains), which ultimately causes considerable structural degradation leading to macroscopic failure. For the first time, this research will investigate the mechanisms associated with yielding and the first collapse event by utilizing *in situ* x-ray microtomography.

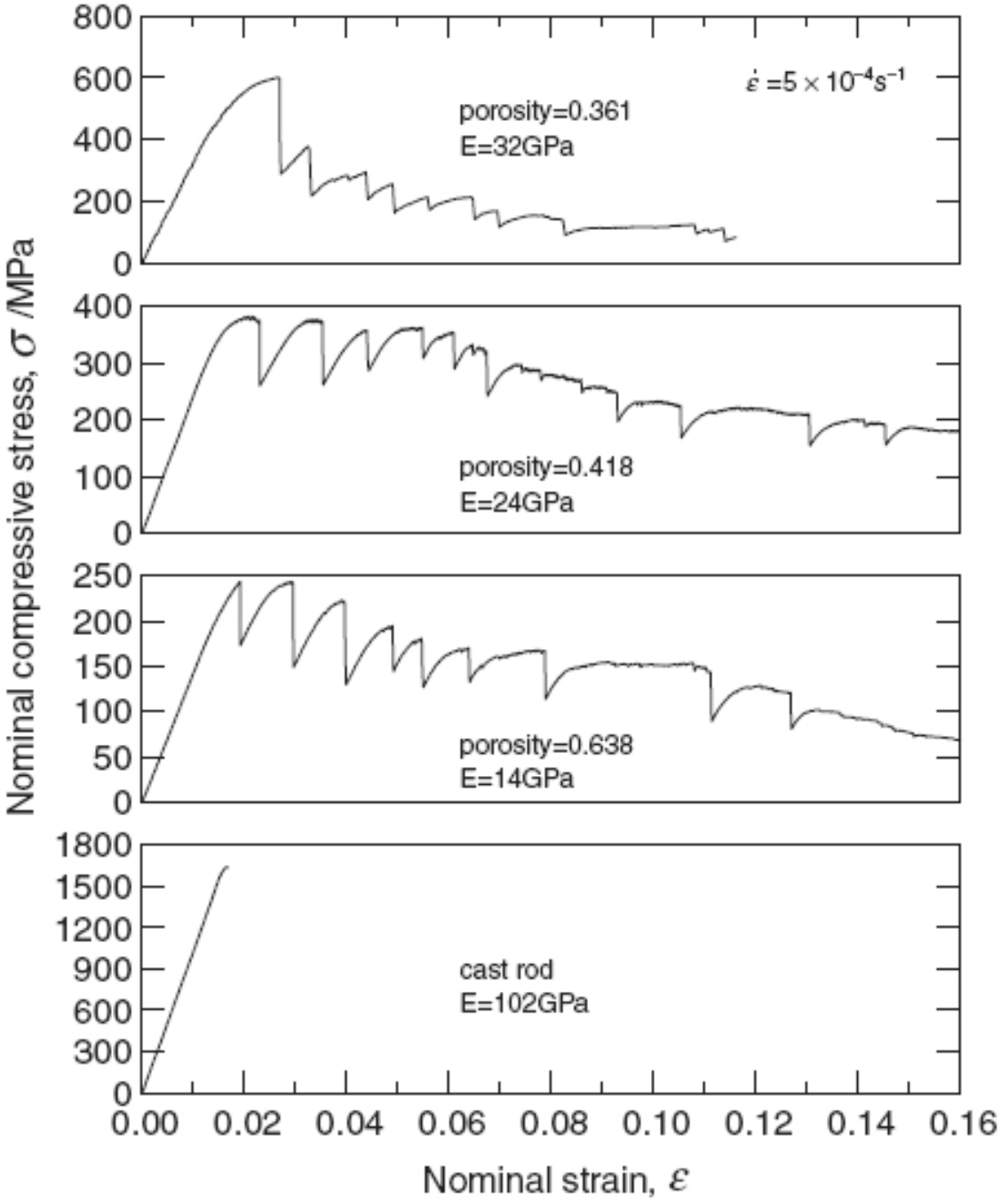

Figure 4. Compressive stress-strain curves of the porous glassy $Pd_{43}Ni_{10}Cu_{27}P_{20}$ alloy rods with porosities of 0.361, 0.418, and 0.638. The data of the pore-free rod prepared by copper mold casting are shown for comparison.

For the loading experiment, a 70% porosity closed-cell amorphous $Pd_{43}Ni_{10}Cu_{27}P_{20}$ foam was prepared by thermoplastic expansion of an amorphous prefoam, as described in Chapter 3 refined beta-foam method [8,9]. The foam was

machined to a tapered test specimen 17.70 mm in height, having a gauge section of 8.08 mm in diameter and 8.14 mm in length. Compressive loading during *in-situ* x-ray microtomography was performed at the ID15A beam line of ESRF [10]. A cylindrical loading fixture specially built for microtomography experiments was utilized [11], which has a maximum loading capacity of 7.5 kN and allows moving a ram at a constant rate in the range of 1-100 μm/min. A ramp displacement rate of 10 μm/min was applied in the present experiment resulting in a nominal strain rate of $\sim 2\times10^{-5}$ s^{-1}. Strains were estimated from crosshead displacement, and were subsequently corrected for nonlinear machine compliance.

The tomographic data recorded at discrete loading states was reconstructed by means of image analysis. A filtered back-projection algorithm [12] was utilized, yielding a 3D representation of the x-ray attenuation coefficient. Tomographic data were subsequently analyzed by the Amira 3D image analysis software using 3D volume rendering and employing an intensity threshold to separate the solid matrix from the cells. For each of the imaged stress states, a $50\times835\times300$ $pixel^3$ segment in the upper half of the $835\times835\times573$ $pixel^3$ foam-specimen gauge section was analyzed at the full resolution of 14 μm/pixel. The rendered view of the analyzed foam segment is presented in Figure 5.

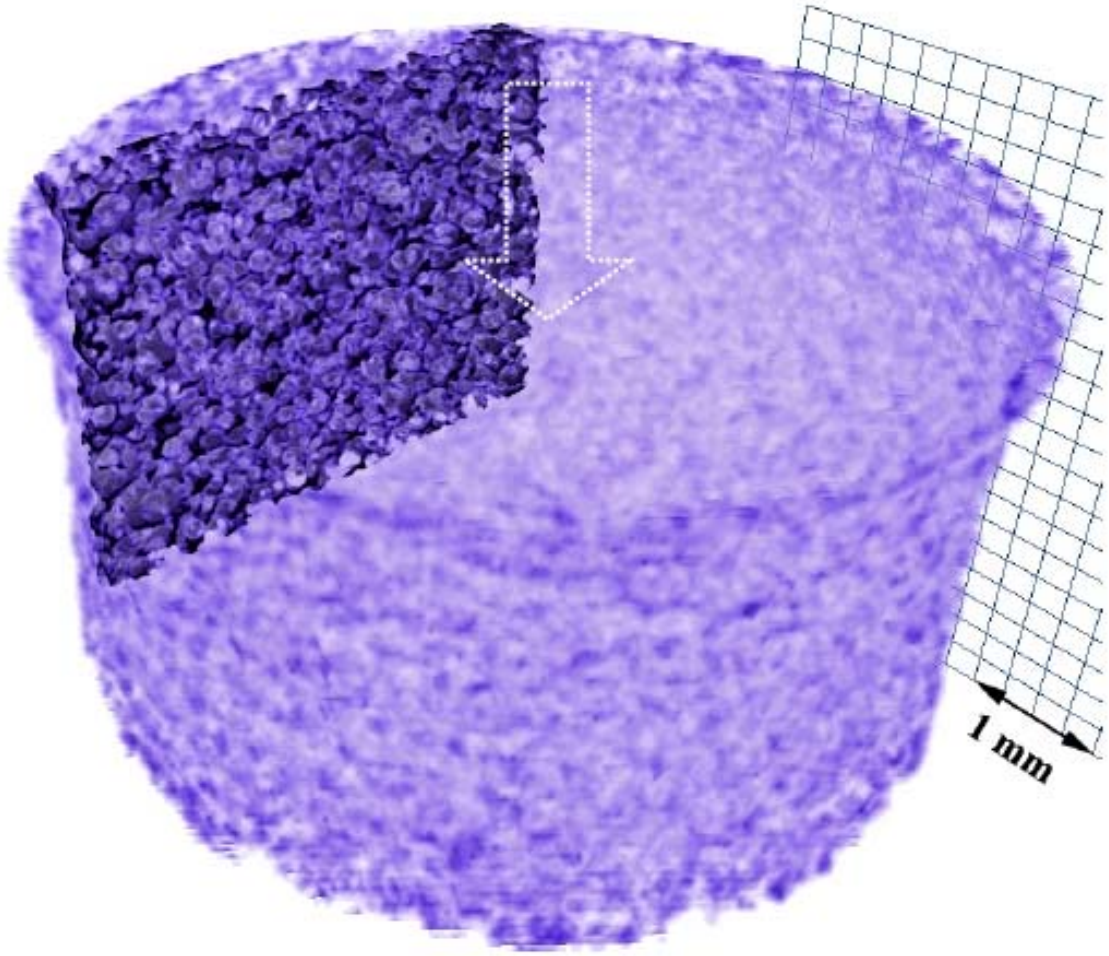

Figure 5. 3D-rendered view of the analysis plane in the unloaded state and its global position within the upper half of the foam-specimen gauge section. Arrow points to the direction of loading.

The cellular structures of the foams produced in this study are found to exhibit rather uniform distributions of cell sizes, which range from a few microns to slightly over 100 μm [9] in all foams. On the contrary, the intracellular solid regions (which can be referred to as intracellular membranes) shown in Figure 3.15 and Figure 3.16 exhibit dimensions that range from μm to mm, and hence their size distributions are expected to be rather broad. This can be attributed to the tendency of cells to impinge and cluster during foaming, which leads to the development of slender intracellular membranes within cell clusters and thick solid regions between clusters. Nevertheless, since these

intracellular regions in effect constitute the structural blocks of the foam, these foams can be regarded as random. Accordingly, the global yielding and collapse of these foams can be expected to evolve stochastically.

The stress-strain diagram associated with the compressive loading of the foam towards the first principal non-catastrophic collapse event and subsequent unloading is shown in Figure 6. The sharp stress oscillations labeled in the loading curve are due to radiation exposure at constant strain during tomographic imaging, which spontaneously elevated the temperature and gave rise to stress amplification. Following a brief high initial compliance, the foam exhibits a linear-elastic response associated with a Young's modulus of ~6 GPa (consistent with established correlations [1]). The loading response eventually departs from linear elasticity towards nonlinearity characterized by an extended stress plateau, which ultimately leads to an incipient non-catastrophic collapse event (between states 14 and 15) associated with a collapse strength of 94 MPa. Upon load reversal, the foam is shown to unload with a modulus essentially unaffected by the collapse event. When completely unloaded, an irreversible strain of 2.3% is recorded.

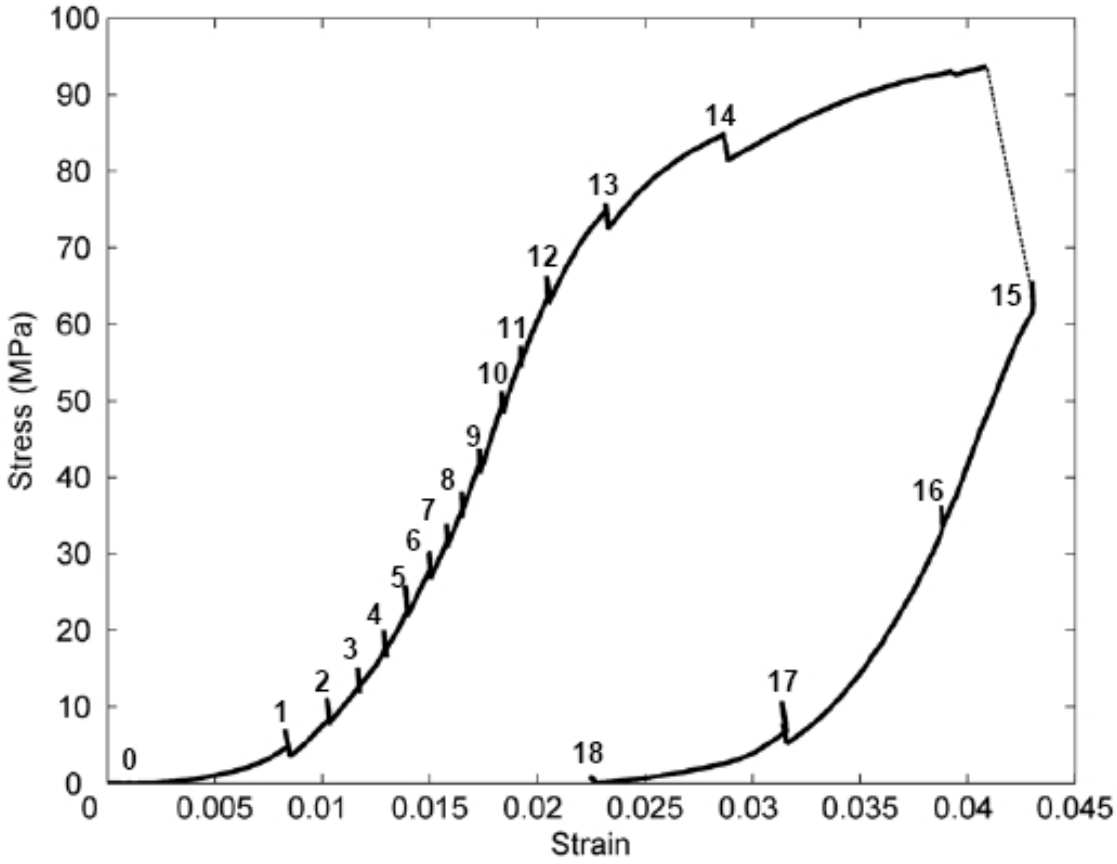

Figure 6. Stress-strain diagram associated with compressive loading of the 70%-porosity foam specimen towards a non-catastrophic collapse event and subsequent unloading. Labels indicate loading states at which x-ray microtomography was recorded.

Despite such large irreversible strain, the unloaded foam specimen appeared intact and no macroscopic damage could be detected. Microscopic damage was inspected by means of scanning electron microscopy. A low-magnification image of the gauge section, presented in panel (a) of Figure 7, reveals no evidence of macroscopic damage. Higher magnification of this image, presented in panel (b), reveals the presence of several microscopic cracks. Further magnification, presented in panel (c), reveals that these cracks were contained by the voids, which acted as stress concentrators inhibiting their propagation. High magnification near a crack, presented in panel (d), reveals the

existence of multiple shear bands indicating buildup of plasticity prior to crack nucleation.

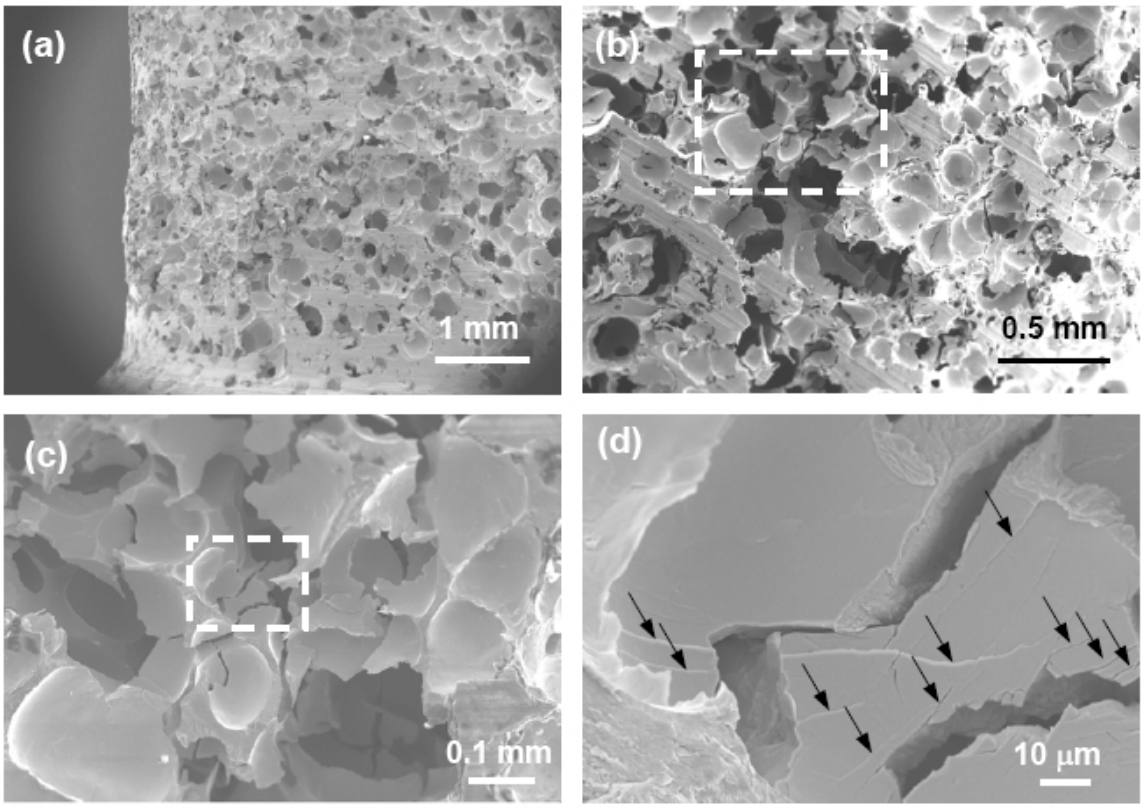

Figure 7. Scanning electron micrographs of the unloaded foam specimen (a) Macroscopic image of the gauge section on a 10:1 magnification; (b) Image of an area in the gauge section on a 20:1 magnification; (c) Magnified image of the area highlighted in (b); (d) Magnified image of the area highlighted in (c) Arrows indicate microscopic shear bands.

By tracking the displacements of cells in the rendered images [13], strains at discrete loading states were calculated as gradients of the displacement fields. The calculated strains are superimposed in Figure 8. In the figure insert, the displacement fields at states 14 and 15 are presented. Within the nonlinear region prior to collapse (state 14), cell displacements appear to be affine, hence verifying a fairly homogeneous deformation. Immediately following collapse (state 15), cell displacements appear non-affine, revealing a large offset of ~0.4 mm. This offset is equal to the change in height of

the specimen measured after unloading. Moreover, this offset corresponds to ~2.3% strain, which is approximately equivalent to the residual strain recorded in the stress-strain diagram. This offset therefore accounts for the majority of irreversibilities realized during this loading cycle (e.g., shear bands and cracks [5,7]). Considering that plasticity in metallic glasses (i.e., shear banding) is manifested in the stress-strain response as serrated flow [14], no significant traces of plasticity can be detected from the foam stress-strain response prior to collapse (aside from minor irreversibilities induced by x-ray exposure at states 13 and 14). Therefore the bulk of irreversible foam damage can be considered to be a product of the collapse event. Accordingly, the nonlinear yielding response of the foam prior to collapse is predominantly elastic.

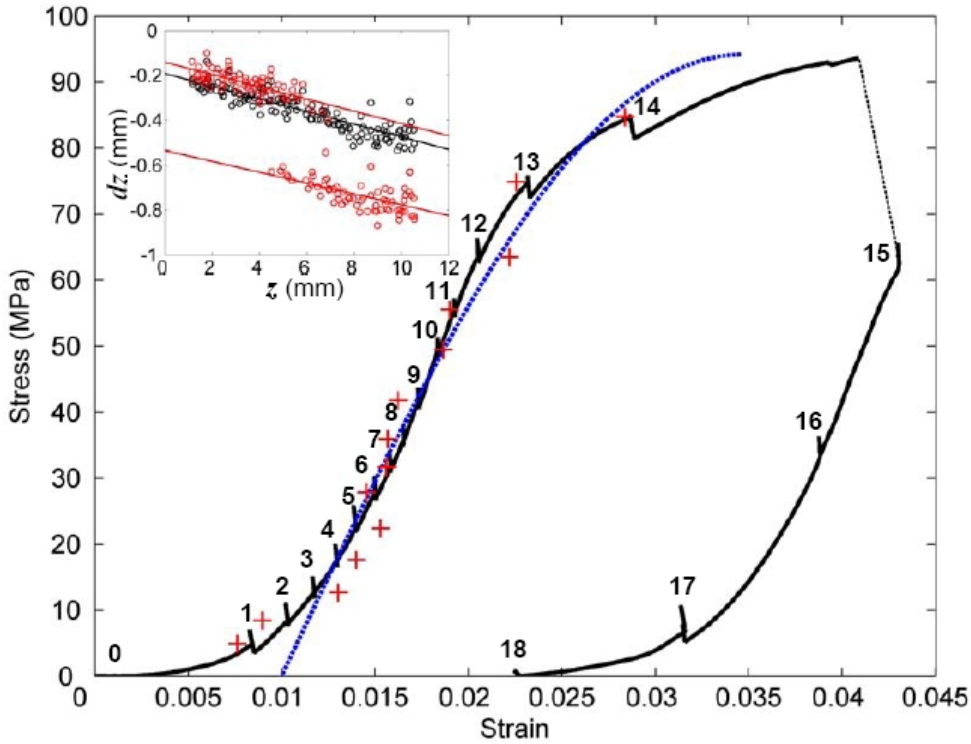

Figure 8. (-) Stress-strain diagram associated with compressive loading of the foam towards a non-catastrophic collapse event and subsequent unloading (labels indicate loading states at which tomographic images were recorded). (- - -) Approximation by the cooperative-yielding model, Eq. . (+) Strain calculated from tracked cell displacements. Insert: Cell displacements vs. cell coordinates along the loading direction: (○) state 14; (○) state 15.

The 3D-rendered view of the analyzed foam segment during loading is presented in Figure 9. In (a) a rendered image of the initial unloaded state (state 0) of the foam segment is presented. In (b), rendered images from states 1-11 are superimposed in an attempt to demonstrate the evolution of linear-elastic deformation. The uniform blurring depicted in this composite image qualitatively verifies that deformation in the linear-elastic regime is homogeneous, as expected. The onset of yielding, which is presented in (c) by superimposing images from states 12-14, is shown to be rather localized along an intermediate transverse plane. The collapse event, which is depicted in (d) by superimposing images from states 14 and 15, shows that foam ultimately collapses along localized yielded regions.

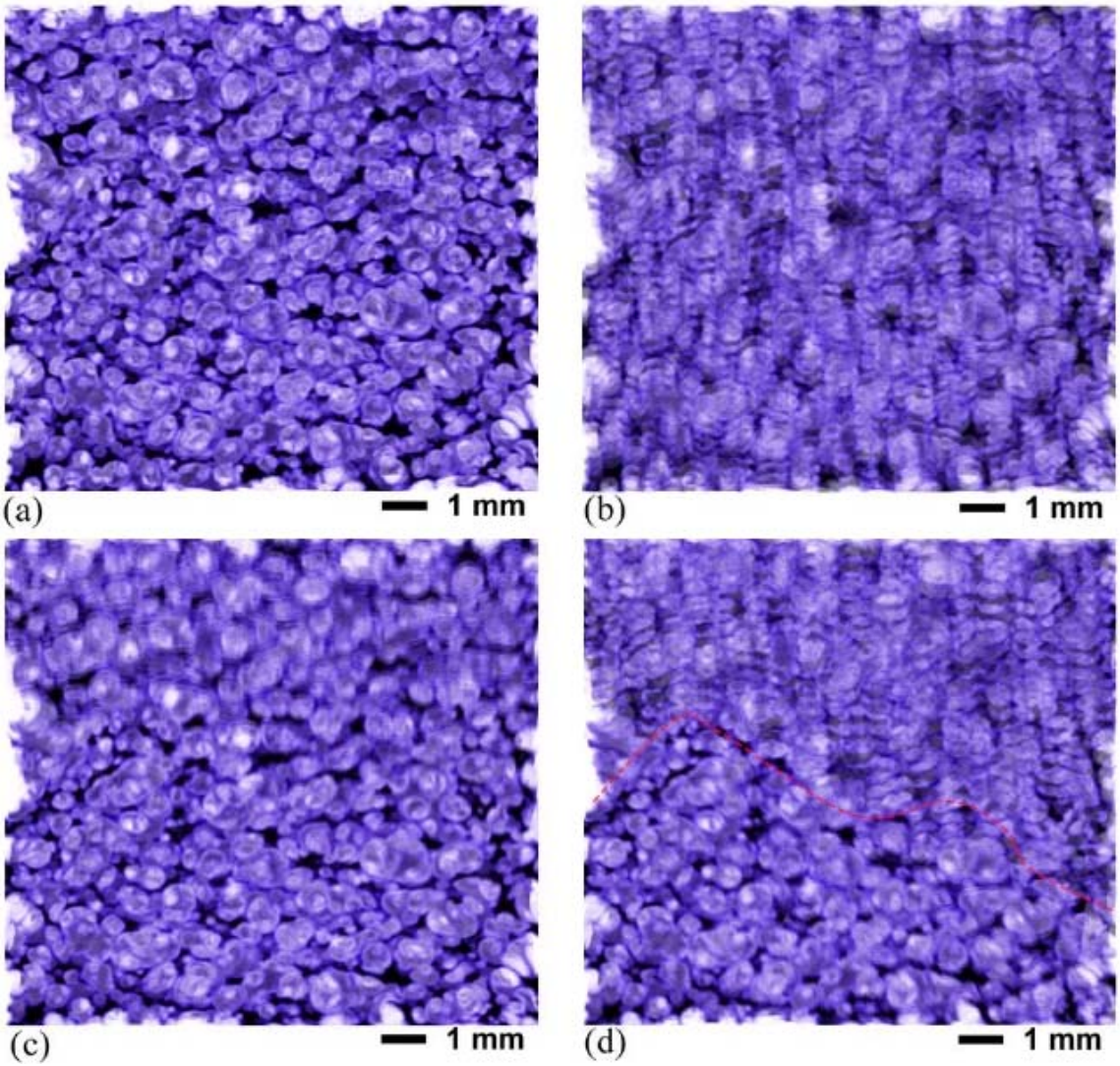

Figure 9. 3D-rendered view of foam structure evolution during deformation. (a) Unloaded state (state 0); (b) linear elastic response (states 1-11); (c) nonlinear response (states 12-14); (d) non-catastrophic collapse (states 14 and 15); the dotted line indicates the regions of localized yielding and ultimate collapse.

Closer inspection within the yielding region of this foam reveals that non-affine displacement is associated with a characteristic length scale on the order of a mm, i.e., on the order of a cluster comprising 4-6 cells. A 3D-rendered view of such a cluster is presented in (Figure 10). Unfortunately, owing to the limited resolution in the present tomographic data (14 μm/pixel), a complete structural examination of these clusters is not feasible. However, the density in the yielding region (at state 0) computed from the

rendered data is found to be 25-30% lower than the bulk foam density, which suggests that cell clusters in this region likely involve high aspect ratio membranes. It is therefore suggested that yielding of those clusters is contributed by cooperative buckling of membranes, which ultimately become unstable and rupture plastically leading to plastic shearing of the cluster.

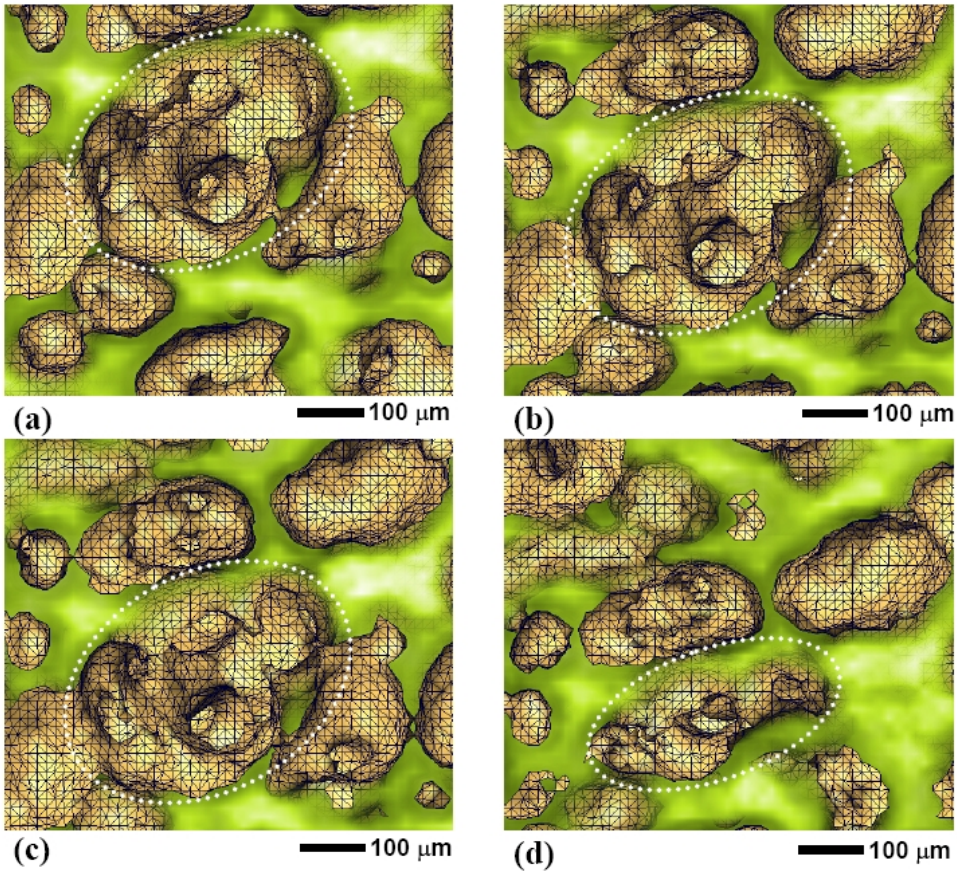

Figure 10. 3D-rendered view of a cooperatively shearing cell cluster within the yielding region. (a) state 0; (b) state 11; (c) state 14; (d) state 15.

Stability of columns against Eulerian buckling is dictated by a critical aspect ratio, which for an ideal column is given by $\sqrt{\pi^2 E/\sigma_y}$ [15], where σ_y/E is essentially the elastic strain limit of the solid. Owing to their high elastic limit, amorphous metals are expected to be unstable against buckling at relatively low aspect ratios [16]. Specifically,

$Pd_{43}Ni_{10}Cu_{27}P_{20}$ is known to have an elastic strain limit of 0.017 [5], which implies that columns of this material having aspect ratios greater than 24 are essentially unstable against Eulerian buckling. As shown in Figure 3.16, membranes having aspect ratios as high as 100 have been detected at random regions in the cellular structure of these foams [8]. In fact, buckling of slender intracellular membranes is clearly visible in a higher-resolution tomographic data (1.4 μm/pixel) [17], in which a specimen originating from the 49% porosity foam produced in this work Figures 3.14c, 3.15c, 3.16c is imaged. 2D-rendered images from that data are presented in Figure 11. Therefore, such geometrically random cellular structure would exhibit a distribution of buckling compliances and can thus be regarded as a stochastic medium.

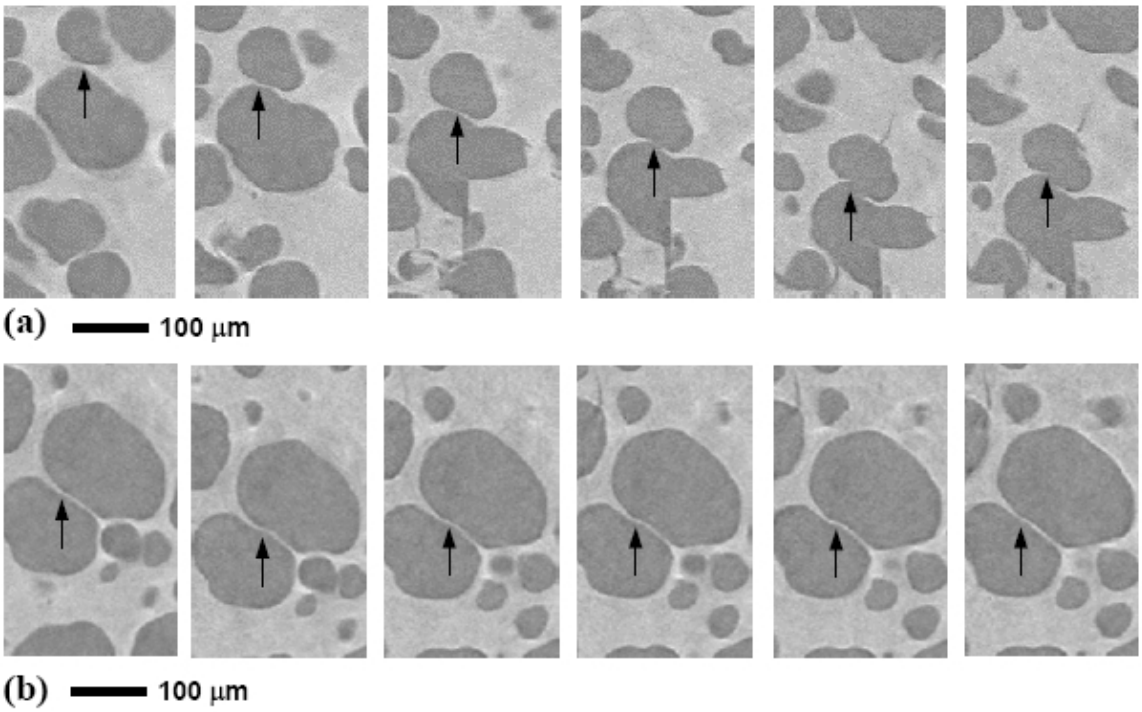

Figure 11. 2D-rendered view of intracellular membranes undergoing Eulerian buckling. (a) membrane buckling followed by plastic rupture; (b) membrane buckling followed by reversible recovery upon unloading.

It is therefore suggested that the global yielding of these foams is dominated by the lower end of the membrane size distribution, i.e., by the slenderer membranes, as these membranes are associated with relatively “softer” (and hence more compliant) structural regions. The principal deformation mechanism of those slender membranes is identified to be Eulerian buckling, which occurs cooperatively and gives rise to a nonlinear-elastic global foam yielding [18]. Once buckling becomes unstable, this buckling instability percolates leading to the formation of a localized buckled band. Ultimately, rupture of the buckled membranes (as shown in panel (a) of Figure 11) gives rise to incipient global foam collapse along the buckled regions. Upon global collapse, plasticity (damage in the form of shear bands and cracks, as evidenced in Figure 7) advances towards thicker intracellular regions, i.e., towards higher sizes in the membrane size distribution. Once plastic collapse is arrested, the structure relaxes to a new state at which it is able to reload again and eventually yield again along a new band of slender membranes. After the occurrence of repetitive collapse events, damage advances towards the tail of the membrane size distribution (i.e., towards the thickest membranes) causing the stiffness of the cellular structure to degrade considerably leading to macroscopic foam failure.

The global nonlinear elastic yielding response of the foam prior to plastic collapse is associated with local membrane buckling. Furthermore, the formation of the localized collapse band is similar to the percolation of a buckling instability. In catastrophe theory, Eulerian buckling is mathematically treated as a cusp catastrophe, i.e., a second-order phase transition [19]. The possible buckling modes of membranes within a cell cluster can therefore be thought of as instabilities of configurational inherent states. Taking ϕ_o

to be the average elastic energy density for configurational hopping to a buckled state, γ to be the overall global configurational strain, and γ_c the average strain per cluster at shear instability, the periodic elastic energy density ϕ can be expressed as $\phi/\phi_o = \sin^2\left(\pi\gamma/4\gamma_c\right)$. This treatment is analogous to that employed by Frenkel to analyze cooperative yielding of a dislocation-free crystal [20] and was recently adopted by Johnson and Samwer to model cooperative yielding of a shear transformation zone in an amorphous metal [21]. This formulation can be extended to a nonlinear shear stress-strain relation as $\tau = \partial\phi/\partial\gamma = \left(\pi\phi_o/4\gamma_c\right)\sin\left(\pi\gamma/2\gamma_c\right)$. Relating ϕ_o to an average shear modulus $G = d^2\phi/d\gamma^2\big|_{\gamma=0} = \pi^2\phi_o/8\gamma_c^2$, the τ - γ relation becomes $\tau = \left(2/\pi\right)G\gamma_c\sin\left(\pi\gamma/2\gamma_c\right)$. Defining E and ν as the average Young's modulus and Poisson's ratio, let's approximate this τ - γ relation by a uniaxial σ - ε relation as follows:

$$\sigma = \frac{2}{\pi}\frac{E}{\left(1+\nu\right)}\gamma_c \sin\left(\frac{\pi}{2}\frac{\varepsilon}{\gamma_c}\left(1+\nu\right)\right) \tag{1}$$

Substituting $E = 6$ GPa and $\nu = 0.42$ [22] for the present foam, Eq. (1) is shown to capture the foam yielding response accurately for $\gamma_c \approx 0.035$ (Figure 8). Furthermore, Eq. (1) is capable of capturing the yielding responses of other closed-cell $Pd_{42.5}Ni_{7.5}Cu_{30}P_{20}$ [5] and $Pd_{35}Pt_{15}Cu_{30}P_{20}$ [7] foams of various porosities (Fig. 4). These foams are found to exhibit γ_c values between 0.035-0.037 (with the exception of one foam exhibiting $\gamma_c \approx 0.033$).

It is therefore evident that this class of foams, which tends to yield cooperatively by percolation of a buckling instability, exhibits a shear-strain limit of ~0.036.

Surprisingly, in the analysis of Johnson and Samwer in which experimental data for more than 30 metallic glasses were utilized, the shear-strain limit of metallic glasses at 0 K (i.e., in the absence of thermal fluctuations) was determined to be 0.036±0.002 [21]. Therefore, this catastrophe induced by nonlinear elastic yielding, identified in both the metallic glass and the metallic glass foam, is characterized by a universal percolation threshold of 0.036.

4.3 High-porosity-foam mechanical properties

High porosity foams with porosities ranging between 83% and 90% were tested by compressive loading. Foams were processed by the refined alpha-foam technique. Cylindrical foam specimens were prepared with polished and parallelized loading surfaces having aspect ratios ranging between 1.25 and 1.65. A screw-driven Instron system with a 50 kN load cell and a servo-hydraulic materials testing system were utilized for the testing. A strain rate of 1×10^{-5} s^{-1} was applied in all tests. Strains were measured using a linear variable differential transformer. The compressive stress-strain response of 83% porosity foam is presented in Figure 12. Up to strains of ~1%, foams are shown to exhibit a linear elastic response. Beyond these strains, foams deform plastically by multiple recurring non-catastrophic collapse events without undergoing macroscopic failure. The numerous minor events indicated are associated with individual ligament collapses. The few major events indicated are associated with the cooperative collapse of several adjacent ligaments and the formation of a collapse band. It is interesting to note that between major events, the serrated flow responses on average

(indicated by dotted lines) appear self-similar and resemble the recurring nonlinear yielding responses exhibited by moderate porosity foams [5,18,23].

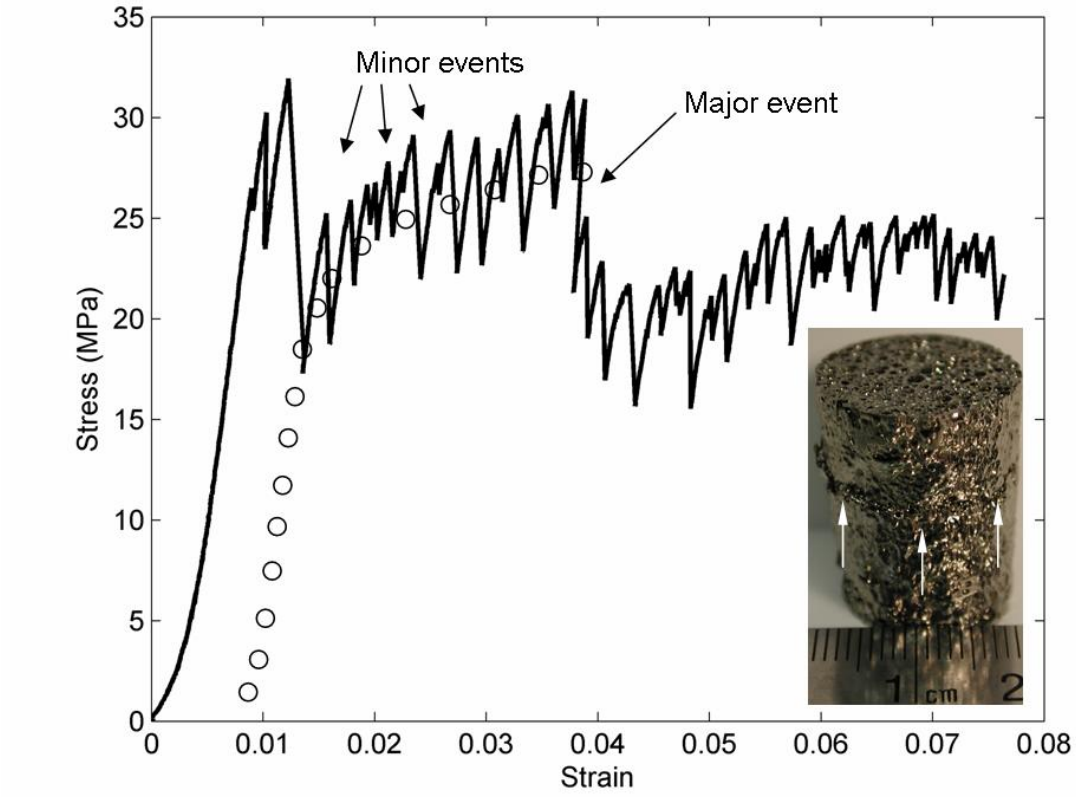

Figure 12. Compressive stress-strain response of 83% porosity foam exhibiting a linear elastic response up to strains of ~1%. Beyond these strains, deformation occurs plastically by multiple recurring non-catastrophic collapse events without undergoing macroscopic failure. Inset shows fully intact specimen after compression and arrows indicate deformation visible at the surface along a nearly horizontal plane. Dotted line represents the average of serrated flow and is extended to zero load to demonstrate the similarity with nonlinear yielding of moderate porosity foams.

Foam yield strengths and Young's moduli normalized by the solid yield strength and Young's modulus are plotted against foam relative densities in Figure 13. These relative strengths and moduli, designated by $\bar{\sigma}_y$ and $\bar{E}$, respectively, can be correlated to the relative densities $\bar{\rho}$ using the correlations established by Gibson and Ashby, as follows [1]: $\bar{\sigma}_y = C_1(\bar{\rho})^{n_1}$; $\bar{E} = C_2(\bar{\rho})^{n_2}$. Power-law fits to the data yield the following

parameter values: $C_1 = 0.31$, $n_1 = 1.64$, and $C_2 = 1.07$, $n_2 = 1.85$. These values are in good agreement with those reported by Gibson and Ashby by fitting mechanical data of various foams:[17] $C_1 = 0.3$, $n_1 = 1.67$, and $C_2 = 1.0$, $n_2 = 2.0$. It is therefore suggested that the foams produced via the refined alpha-foam route exhibit mechanical properties that are consistent at substantially high porosities and in accord with the established correlations.

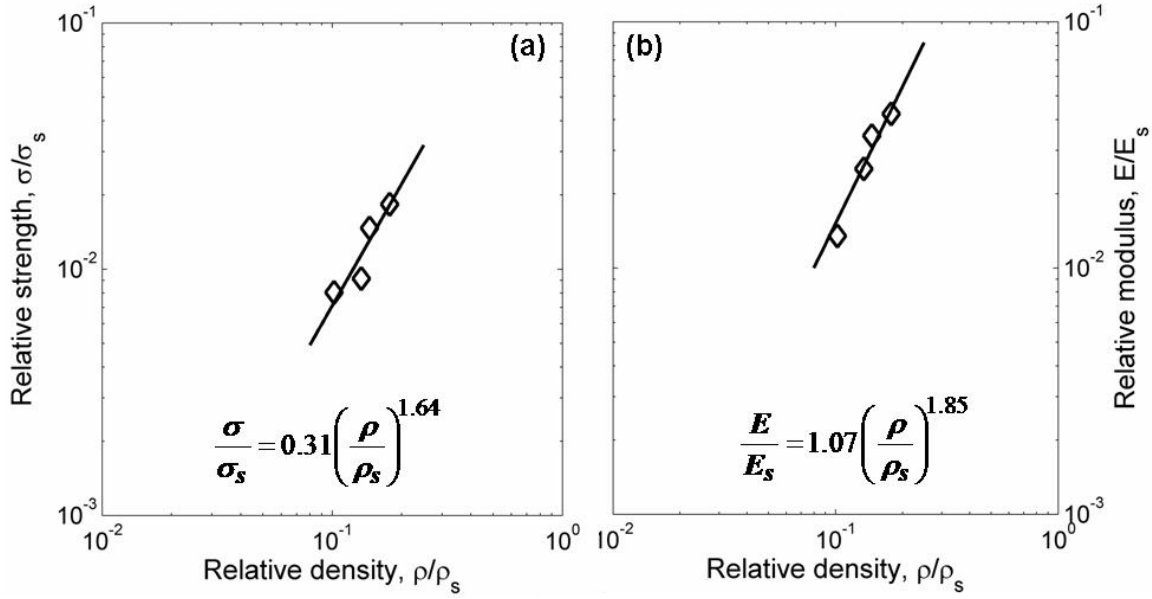

Figure 13. (a)Foam yield strengths (taken as the stress at the first major plastic collapse event) normalized by the solid yield strength plotted against foam relative densities. (b) Foam Young's moduli (taken as the slope of the loading curve in the linear elastic region) normalized by the solid Young's modulus plotted against foam relative densities. The solid yield strength and Young's modulus are taken as 1635 MPa and 102 GPa, respectively [Wada T, Inoue A. Mater. Trans. JIM 2004;45, 2761.]. Power law fits, which conform to established correlations, are shown as dotted lines [Gibson LJ, Ashby MF. Cellular Solids: Structure and Properties. 2nd Ed. Cambridge, UK: Cambridge University Press, Ch. 5., 1997.].

4.4 References

[1] Gibson LJ, Ashby MF. Cellular Solids: Structure and Properties. 2nd Ed. Cambridge, UK: Cambridge University Press, Ch. 5., 1997.

[2] Brothers AH, Dunand DC. Amorphous metal foams. Scr. Mater. 2006;54:513.

[3] Brothers AH, Dunand DC. Ductile bulk metallic glass foams. Adv. Mat. 2005;17:484.

[4] Brothers AH, Dunand DC. Plasticity and damage in cellular amorphous metals. Acta. Mater. 2005;53:4427.

[5] Wada T, Inoue A. Formation of porous Pd-based bulk glassy alloys by a high hydrogen pressure melting-water quenching method and their mechanical properties. Mater. Trans. JIM 2004;45:2761.

[6] Veazey C, Schroers J, Johnson WL. Unpublished Data.

[7] Wada T, Takenaka K, Nishiyama N, Inoue A. Formation and mechanical properties of porous Pd-Pt-Cu-P bulk glassy alloys. Mater. Trans. JIM 2005;46:2777.

[8] Demetriou MD, Veazey C, Schroers J, Hanan JC, Johnson WL. Expansion Evolution During Foaming of Amorphous Metals. Proc. RQ12 (Aug. 2005). Mat. Sci. Eng.: A 2005.

[9] Demetriou MD, Veazey C, Schroers J, Hanan JC, Johnson WL. Thermo-plastic Expansion of Amorphous Metallic Foam. Proc. Ismanam '05 (Jul. 2005). J. Alloys. Comp., 2005.

[10] Di Michiel M, Merino JM, Fernandez-Carreiras D, Buslaps T, Honkimaki V, Falus P, Martins T, Svensson O. Fast microtomography using high energy synchrotron radiation. Rev. Sci. Instrum. 2005;76.

[11] Viggiani G, Lenoir N, Besuelle P, Di Michiel M, Marello S, Desrues J, Kretzschmer M. X-ray microtomography for studying localized deformation in fine-grained geomaterials under triaxial compression. Comptes Rendus Mecanique 2004;332:819.

[12] Kak AC, Slaney M. Principles of Computerized Tomographic Imaging. New York: IEEE, 1988.

[13] Cell positions in 2D rendered images were tracked by means of template recognition using IMAQ Vision Builder image-analysis software.

[14] Chen HS. Plastic-Flow in Metallic Glasses under Compression. Scr. Metall. 1973;7:931.

[15] Inoue A, Nishiyama N, Matsuda T. Preparation of bulk glassy Pd40Ni10Cu30P20 alloy of 40 mm in diameter by water quenching. Mater. Trans. JIM 1996;37:181.

[16] Birringer R, Harmon JS, Veazey C, Demetriou MD, Johnson WL. Unpublished work.

[17] Shiley SA, Üstündag E, Gray JN, Veazey C, Demetriou MD, Lenoir N, Di Michiel M, Johnson WL. In preparation.

[18] Demetriou MD, Hanan JC, Veazey C, Di Michiel M, Nenoir N, Üstündag E, Johnson WL. In review.

[19] Gilmore R. Catastrophe Theory for Scientists and Engineers. New York: John Wiley & Sons, 1981, p. 258.

[20] Frenkel J. Z. Phys. 1926;37:572.

[21] Johnson WL, Samwer K. Phys. Rev.Lett. 2005;95.

[22] The Poisson's ratio of monolithic Pd40Ni10Cu30P20 is evaluated acoustically to be ~0.395 (see Nishiyama N IA, Jiang JZ. Appl. Phys. Lett. 78, 1985 (2001)). For the foams we assume a slightly higher value (0.42 for all foams), in accordance with recently reported correlations (see Phani KK, Sanyal D. J. Mater. Sci. 40, 5685 (2005)). It is noted that Eq. (1) is rather insensitive to Poisson's ratio, so that the choice of the Poisson's ratio value has a minimal effect on the model predictions.

[23] Veazey C, Demetriou MD, Hanan JC, Schroers J, Üstündag E, Johnson WL. In Review.

CHAPTER 5

SUMMARY AND FUTURE RESEARCH

5.1 Summary

The goal of this research was to synthesize amorphous metallic foam and examine its mechanical properties. Several innovative foam processing routes were developed and cutting-edge in situ tomography was utilized to probe mechanical deformation. Models were utilized to explain bubble growth, sedimentation, and stress-strain response. In addition, microgravity foam expansion tests were accomplished and potential space applications were explored. Through four years of collaborative research, an understanding of the critical experimental variables governing the synthesis and mechanical deformation of amorphous metallic foam have developed.

5.2 Future research on amorphous metallic foam

The foaming of closed-cell $Pd_{43}Ni_{10}Cu_{27}P_{20}$ has been researched in detail. The next step in future research would be to extend this foaming capability to commercial alloys such as vitreloy, iron-based alloys, or bio-compatible alloys. Further research could yield a foam product of high homogeneity and desired porosity. Another future research direction would be to develop commercial amorphous metallic foam with hydrogen as its blowing agent. Large amounts of hydrogen can be dissolved homogeneously in alloys at high temperature. This approach has been shown to work with $Pd_{43}Ni_{10}Cu_{27}P_{20}$ and could be adapted to a commercial alloy [1]. A major drawback

of using hydrogen is that it may cause embrittlement of some alloys. Perhaps a synthesis route can be developed using an alloy that does not embrittle.

5.3 Future research on amorphous cellular composites

In 1982, Johnson and co-workers developed a method called the hollow-jet instability technique to produce hollow metallic glass spheres [2,3]. This technique uses a jet of gas to make a drop of liquid metal into a thick-walled bubble as shown in Figure 1. The hollow sphere solidifies amorphous at it falls freely. Although, there are technical difficulties surrounding the production of high quality hollow spheres. For example, the surface could become distorted by the aerodynamic eddies swirling around the falling sphere.

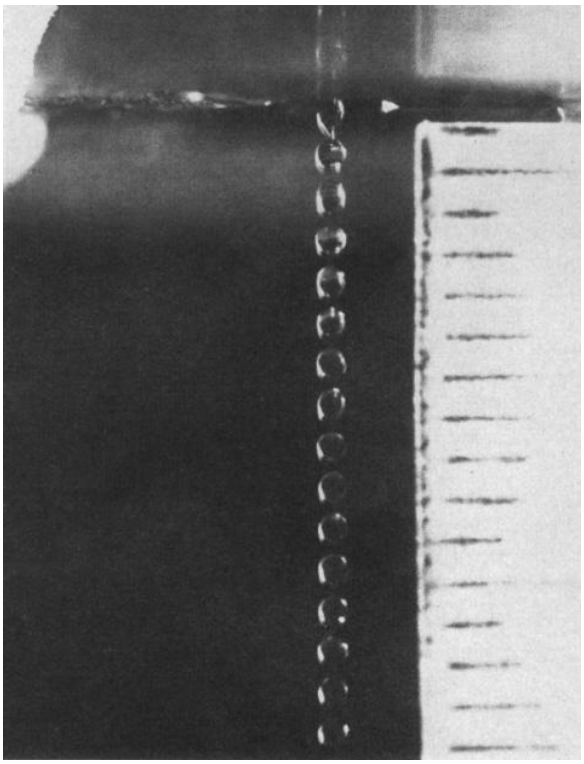

Figure 1. Test of shell generator using water. Kendall JM, Lee MC, Wang TG. Metal shell technology based upon hollow jet instability. J. Vac. Sci. Technol. 1982;20:1091.

One application of hollow spheres would be to closely pack the shells and bond them together to form a desired shape. The resulting closed-cell foam would be highly porous with homogenous and isotropic mechanical properties. The shell thickness could be tailored for the desired strength and stiffness. A variety of bonding techniques could be explored to reduce stress concentrations on the touching surfaces of spheres.

5.4 Future research on the application of amorphous metallic foam

The benefits of a high strength and highly elastic metallic foam could be realized by its application as a kinetic energy absorber as shown in Figure 2. Several other desirable qualities include high stiffness and low density. Military and civilian applications are envisioned such as vehicle armor shielding and earthquake vibration absorbers.

Figure 2. Crushable aluminum foam structure. The outer skin is a container for foam expansion.

The unique processing ability of amorphous metallic foam would enable its use as a deployable and expandable structure material for space applications. Additionally, it would provide shielding from micro-meteorites and radiation. The impact of landing

could be absorbed by crushable foam landing pads. A habitat could be constructed in space as shown in Figure 3.

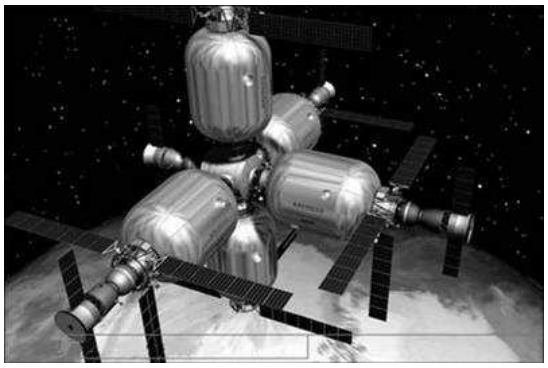

Figure 3. Space habitat constructed from repeating structures.

Implantation of bio-compatible amorphous metallic foam is envisioned as an application due to its cellular structure. An example of open cellular bone is shown in Figure 4. The material could be designed to have bio-mimetic properties such as bone in-growth. Additionally, the implants could be designed for dental, spinal, or orthopedic applications.

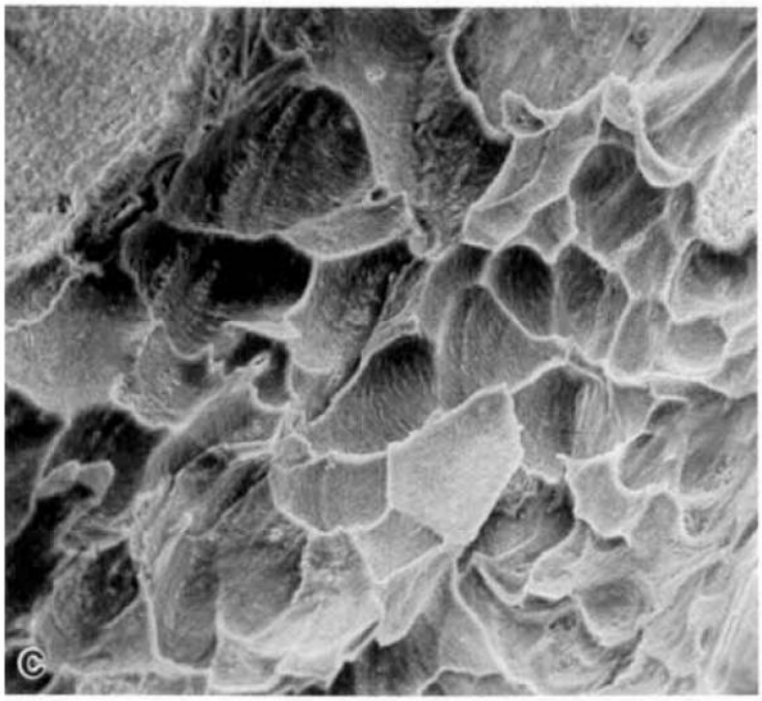

Figure 4. Cervical vertebra cancellous bone imaged with a field width 170 microns Boyde, Jones, Microscopy Research and Technique. 33, 92 (1996)

5.5 Conclusion

Research on advanced materials is often met with unforeseen challenges. The critical aspects are only appreciated after years of experiments are conducted. Careful research will lead to important discoveries. Hopefully, this thesis will aid the next researcher in their scientific endeavors.

5.6 References

[1] Wada T, Inoue A. Formation of porous Pd-based bulk glassy alloys by a high hydrogen pressure melting-water quenching method and their mechanical properties. Mater. Trans. JIM 2004;45:2761.

[2] Lee MC, J.M. K, Wang TM, Johnson WL. Investigation of metallic and metallic glass hollow spheres for fusion target application. Materials Processing in the Reduced Gravity Environment of Space 1982:105.

[3] Kendall JM, Lee MC, Wang TG. Metal shell technology based upon hollow jet instability. J. Vac. Sci. Technol. 1982;20:1091.

APPENDIX I

MICROGRAVITY FOAMING ONBOARD THE INTERNATIONAL SPACE STATION

In preparation for publication

"Foaming of Amorphous Metals Approaches the Limit of Microgravity Foaming"

Foaming liquid metals is a challenging task since the dynamics of bubble nucleation, growth, sedimentation, merge, and collapse scale inversely with liquid viscosity, which for conventional metals is relatively low. A newly discovered foam-synthesis route utilizing the viscous undercooled liquid state of metallic glasses [1,2] seems promising in evading these technological intricacies arising from the low viscosity of conventional metallic liquids. The high viscosity exhibited by undercooled liquid states contributes to dampen the rate of foaming effectively and hence enhance foaming controllability. More importantly, this high viscosity contributes to reduce bubble sedimentation caused by gravity and hence improve cellular-structure homogeneity.

In Figure 1, the temperature-dependent viscosity of liquid aluminum [3] is compared against that of $Pd_{40}Ni_{40}P_{20}$ [4], a rigorously studied glass-forming metallic liquid. As evidenced from this plot, at their respective foam processing windows the viscosity of $Pd_{40}Ni_{40}P_{20}$ exceeds that of aluminum by more than 10 orders of magnitude. Using the Stokes equation, the sedimentation velocity of a 1 mm argon bubble in liquid aluminum can be estimated to be on the order of 1 m/s, while in liquid $Pd_{40}Ni_{40}P_{20}$ it can be estimated to be on the order of 1 nm/s. This simple estimate underlies the foaming

advantage of glass-forming metallic liquids over conventional metallic liquids. In fact, owing to this advantage, foaming of amorphous metals can be thought as the equivalent of microgravity foaming of conventional metals.

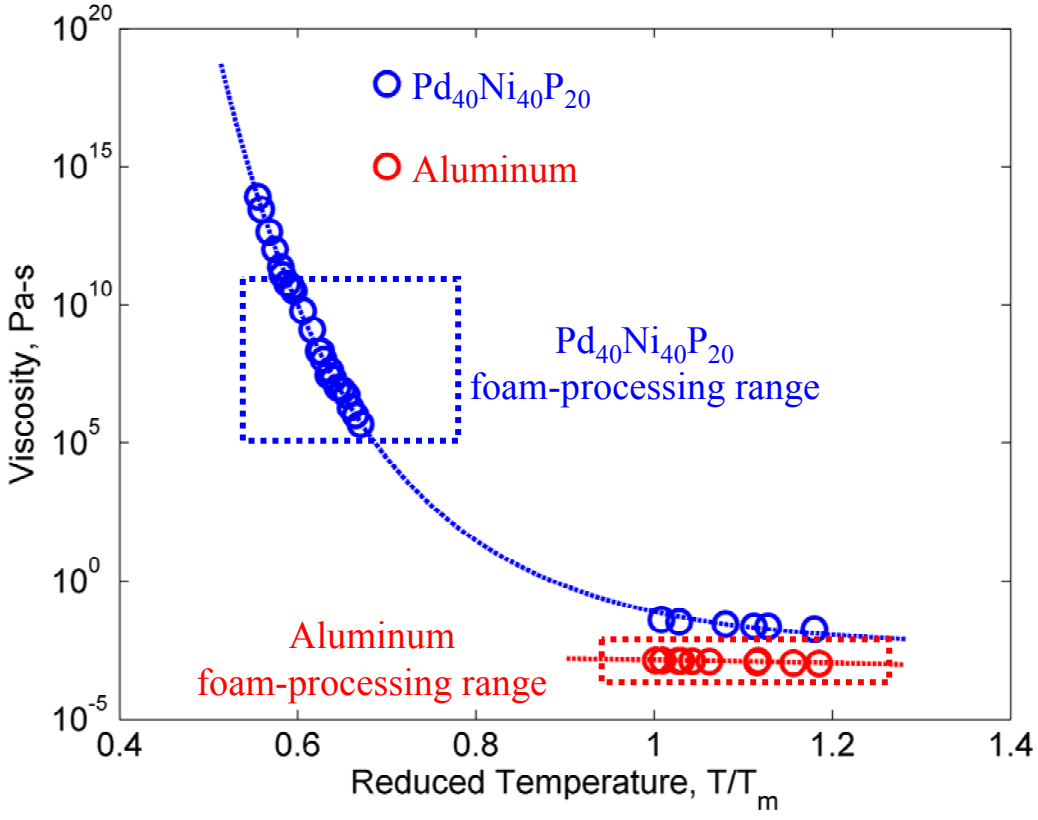

Figure 1. Viscosity of liquid aluminum and $Pd_{40}Ni_{40}P_{20}$ plotted against reduced temperature (ratio of temperature to melting temperature). The respective foam-processing ranges are indicated.

An additional effect of microgravity is to eliminate gravitational shape changes on bubble sphericity. The gravitational pressure gradient for a single 1 mm radius bubble is approximately 200 Pa from top to bottom (Equation 1). Meanwhile, the capillary pressure for the 1mm radius bubble is 2,000 Pa (Equation 2).

$$\nabla P_{Gravity} = \rho g \Delta h \qquad (1)$$

$$P_{Capillary} = \frac{2\sigma}{R} \qquad (2)$$

ρ = 9.3 kg/m^3 , σ = 1 J/m^2 , g = 9.8 m/s^2 (approximate values)

Thus, the gravity exerts a pressure at the bottom of the bubble that is 10% higher than at the top, although, this effect has not been observed in our foams. This communication aims to demonstrate that foaming of amorphous metals under microgravity conditions results in cellular structures similar to those obtained under the effect of gravity.

A set of foaming experiments under gravity was performed at the California Institute of Technology, while a set of microgravity foaming experiments was performed on the International Space Station on July 6, 2005 (see NASA Foam experiment patch in Figure 2). Cylindrical 1.4-gram amorphous $Pd_{43}Ni_{10}Cu_{27}P_{20}$ foam precursors were prepared. The precursors incorporate micro-bubbles containing gas at 1 atm, and are capable of foaming when heated above the softening point of the metallic glass under reduced pressures. The precursors were enclosed in evacuated cylindrical copper ampoules, whose volume was larger than the precursor volume to allow expansion. The ampoules were threaded onto a modified soldering iron tip, which was used to heat the samples to initiate foaming. In Figure 3, the ampoule/compact resistance unit before and during foaming is presented, respectively. Samples were foamed for a duration of 5 minutes, and were subsequently allowed to free-cool and vitrify.

Figure 2. NASA Foam experiment patch designed by Candice Young at MSFC.

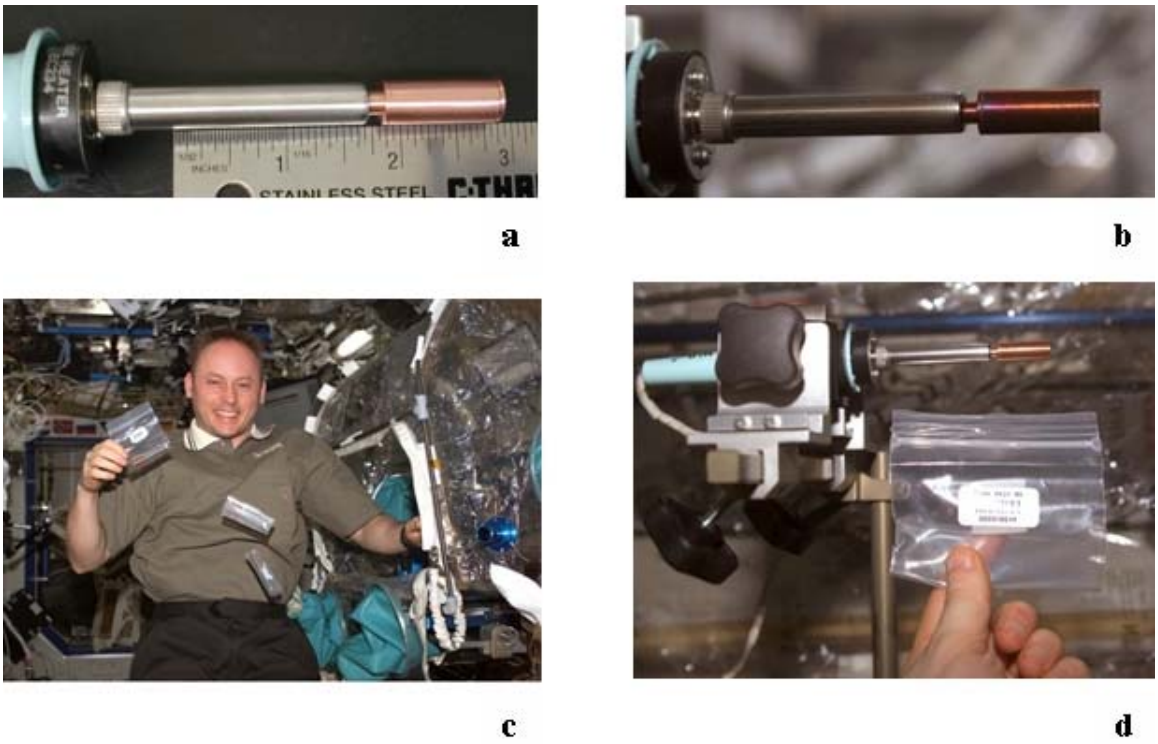

Figure 3. Copper ampoule before (a) and during (b) foaming. Astronaut Science Officer Mike Fincke foaming bulk metallic glass using the soldering iron inside the Maintenance Work Area onboard the International Space Station (c and d).

The hardware utilized for this investigation was readily available on the International Space Station. To heat samples, a battery-operated soldering iron that is part of their on-orbit tool kit is utilized. The experiment was conducted inside the Space Station Maintenance Work Area -- a portable workbench that can be used throughout the Station. Gloveports on the sides and ends of the workbench's plastic cover and a front flap that unzips allow crew members to use the soldering iron or other tools for space operations. In Figure 3, a photograph of Astronaut Mike Fincke using the soldering iron to heat the foam precursor ampoule is presented.

Optical micrographs of the foam sections produced under gravity and microgravity are shown in Figure 4. As evidenced from these images, foam morphologies from both experiments exhibit negligible bubble-size gradients along the

gravity direction. This suggests that gravity has a negligible effect on the foaming of amorphous metals. Close-up micrographs of these sections are presented in Figure 5. Foam morphologies from both sets of experiments exhibit similar cellular structure, which also supports that gravity and microgravity foaming produce cellular structures that exhibit essentially identical characteristics.

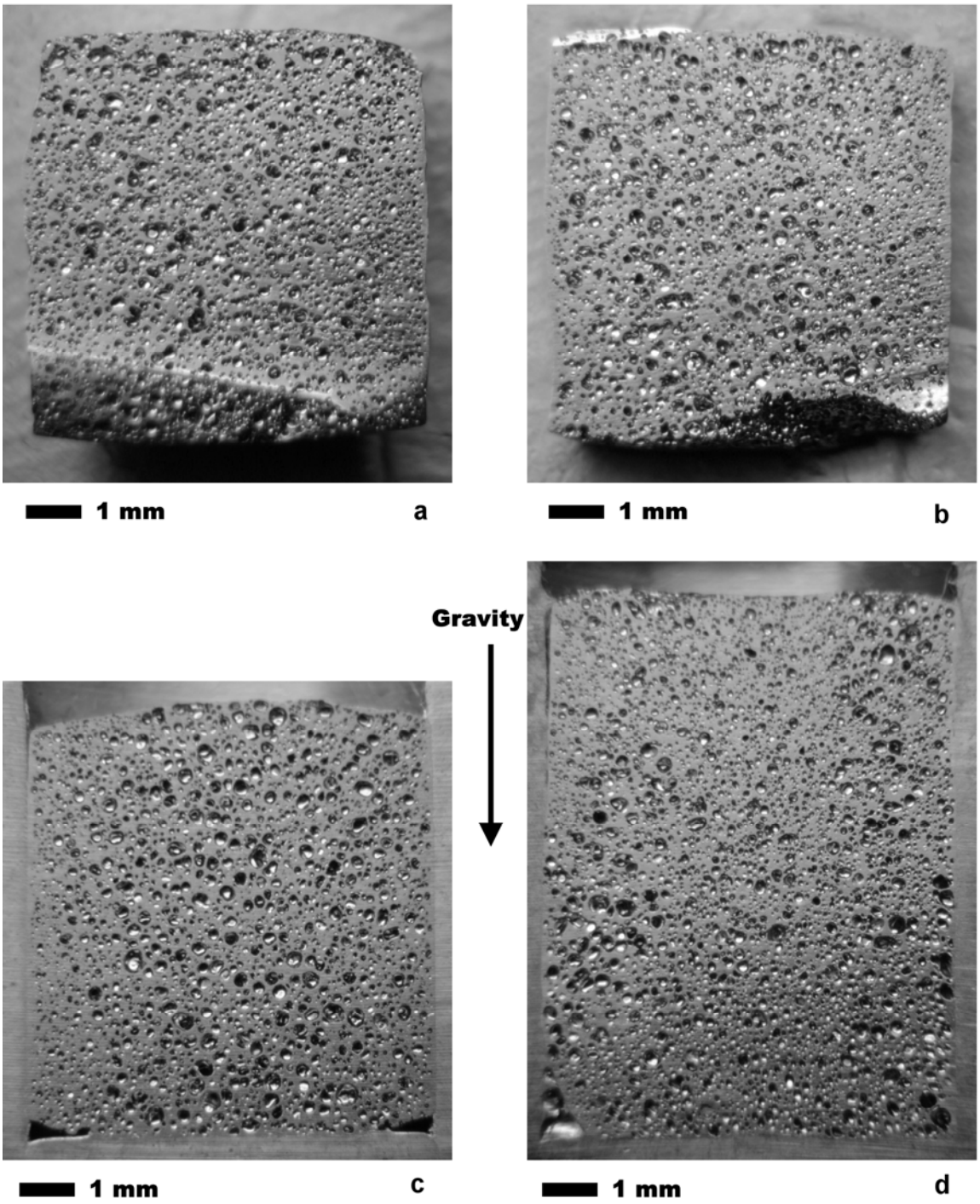

Figure 4. Macroscopic optical micrographs of foams processed at 360 °C for 5 minutes under microgravity (a and b); under gravity (c and d). Gravity vector points down.

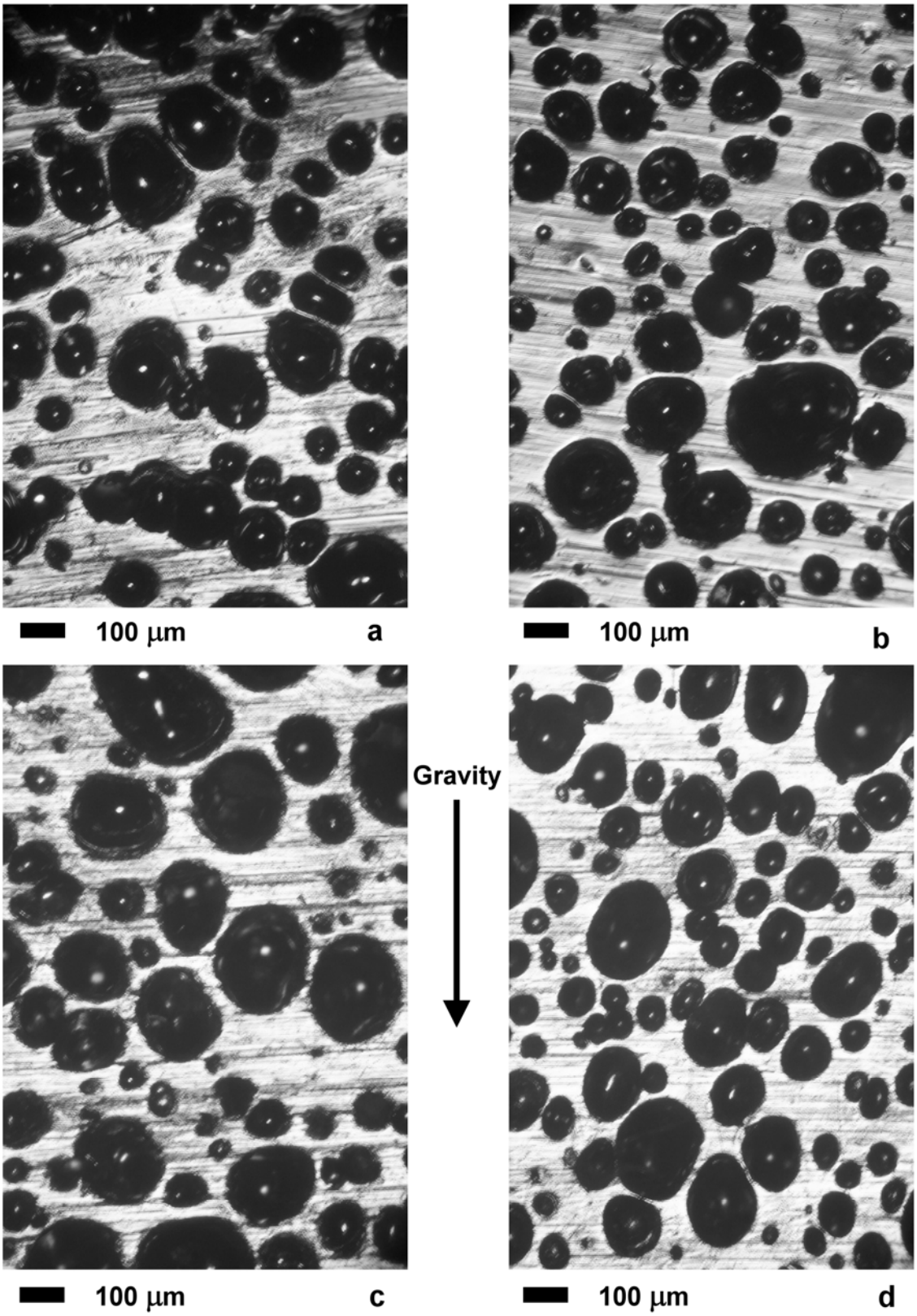

Figure 5. Close-up optical micrographs of foams processed at 360 °C for 5 minutes under microgravity (a and b); under gravity (c and d). Gravity vector points down.

It is therefore demonstrated by these two sets of experiments that foaming of amorphous metals approaches the limit of microgravity foaming. Under microgravity conditions, bubbles don't rise, liquid doesn't drain, and surface tension dominates. These advantages of microgravity are significant in conventional metal foaming, since the morphological inhomogeneities arising due to bubble sedimentation would be eliminated. In fact, in order to mimic the advantages of microgravity in conventional metal foaming, elaborate processes are employed in order to increase melt viscosity. These include stirring additives into the melt [5] or process foaming in the semi-solid state [6]. On the contrary, the advantages of microgravity are demonstrated in this study to be redundant for amorphous metal foaming. This is due to the high viscosity of their undercooled liquid, which negates the effects of gravity. Owing to their low liquid viscosity, conventional metal foaming can be thought as frothy soap-water. Conversely, amorphous metal foaming can be envisioned as bubbly honey. This advantage renders bulk metallic glasses an ideal material for metal foaming.

In addition to the primary purpose of the current experiment, which was to demonstrate the inherent microgravity-foaming ability of amorphous metals, the experiment also demonstrated the applicability of amorphous metallic foam as a space structural material. Owing to the thermoplastic-like processing ability of amorphous metals [7,8], foaming can be performed by softening pre-processed amorphous foam precursors, as has been demonstrated in this study. Owing to this capability, low-volume expandable amorphous precursors can be deployed, thereby reducing payload launch volume. Under naturally low ambient pressures, these precursors can be expanded into

metallic foam structures by simply raising temperature. Furthermore, owing to their net-shape forming ability, precursors can be foamed into various shapes necessary to construct a structure. In fact, construction of expandable habitat structures on the moon can be thought to be a rather attractive structural application for this material. This is because of the unique energy absorption capability of the material [9], which would enable effective shielding of vital Space Station components. Due to this energy absorption capability, micro-meteoroid impacts and the associated energetic plasma cones of debris would spread uniformly within the material, thereby preventing damage to shielded parts. It can therefore be anticipated that the next generation of space exploration would greatly benefit from advanced materials such as amorphous metallic foam.

APPENDIX II

THE GAMMA-FOAM METHOD

The invention of gamma-foam allows the development of a commercially viable BMG foam.[†] The method utilizes powder consolidation under highpressure and foam expansion in the undercooled liquid state. Bubble expansion is driven by either blending in gas-releasing agents or by trapping inert gas at high pressure between granules of BMG powder.

Consolidation of the mixture is performed at a temperature below the crystalline transition temperature of the alloy. The consolidation process is performed at the highest possible temperature in order to promote visco-plastic deformation during powder consolidation. Consolidation is performed for a duration not exceeding the time for the crystalline transformation to take place, and is immediately followed by cooling in order to retain the amorphous state of the material. In this experiment, hot isostatic pressing (hipping) is performed to consolidate amorphous powders.

Expansion of the consolidated amorphous precursor into foam is performed in the undercooled liquid state of the alloy, which forms between the amorphous transition and the crystalline transition of the alloy. The expansion process is performed at the highest possible temperature in order to promote visco-plastic deformation during bubble expansion. The expansion process is performed at the lowest possible ambient pressure in order to promote the expansion driving force arising from difference between the

[†] Patent pending on "Production of amorphous metallic foam by powder consolidation" (US60/645638).

stored gas pressure and the ambient pressure. A micrograph in Figure 6 compares a precursor to the expanded foam. The expansion process is performed for a duration not exceeding the time for the crystalline transformation to take place, and is immediately followed by cooling in order to retain the amorphous state of the material. A DSC thermogram in Figure 7 shows the amorphous state has been retained but slightly degraded.

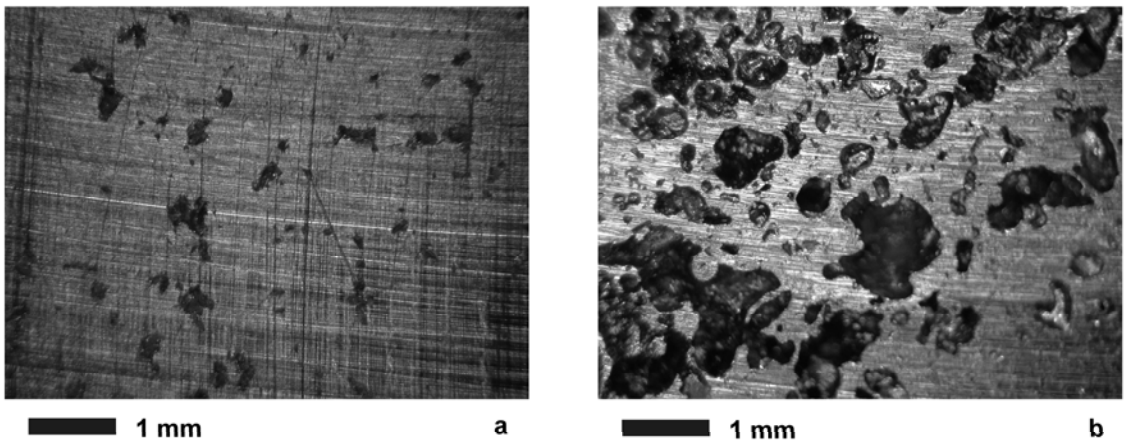

Figure 6. Micrographs of (a) hipped prefoam $Pd_{43}Ni_{10}Cu_{27}P_{20}$ (b) after foaming in an RF coil.

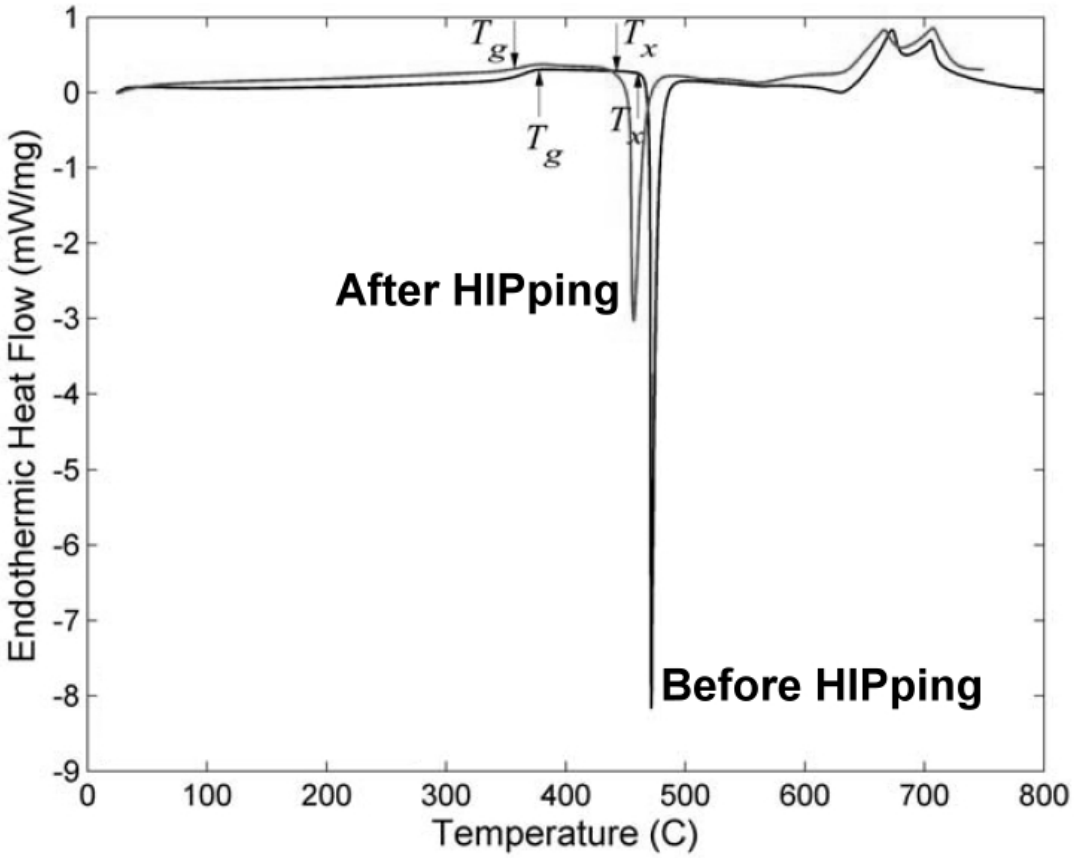

Figure 7. DSC thermogram on $Pd_{43}Ni_{10}Cu_{27}P_{20}$ shows the effect of hipping process on degradation of the glass. Before hipping, the crystallization peak is sharp and large. After hipping, the crystallization peak is smaller and has shifted to lower temperature.

Methods exist by which metallic foam can be produced by consolidating particulates of the alloy in its crystalline state under a high-pressure gas atmosphere, or blended with gas-releasing agent particulates. Since metals in their crystalline state exhibit poor plasticity, the plastic deformation that can be accomplished during consolidation, as well as during expansion, is limited. The proposed method constitutes an improvement over this existing method, as the "softened" undercooled liquid state of amorphous metals possesses visco-plastic properties, which can be utilized to accomplish higher plastic deformation during consolidation as well as during expansion.

By the beta-foam method, amorphous metallic foam can be produced by introducing bubbles of supersaturated gas to the liquid metal at a temperature above the liquidus temperature of the alloy and then quenching to form an amorphous precursor foam. The precursor can be expanded in the same manner as described in this proposed invention. The gamma-foam method constitutes an improvement over the beta-foam, as the volume fraction as well as the spatial and size distribution of gas voids can be effectively controlled by the size distribution of the powder particulates. Another improvement of the gamma-foam method is that the interaction between the alloy and the gas or gas-releasing agent occurs in the undercooled liquid state rather than in the liquid state, and consequently, the temperature is lower and the reactivity between the alloy and the gas or gas-releasing agent is suppressed. A further improvement is that in the proposed method, no limitations on the size of the produced precursor are imposed. This is in contrast to beta-foam, in which the precursor is rendered amorphous by quenching from the liquid state, and consequently limitations on the size of the produced precursor are imposed by the rate of heat removal. A list of relevant patents and publications can be found in references [2,10-16].

APPENDIX III

PREFOAMING BY THE MECHANICAL ENTRAINMENT METHOD

An alternative to using a blowing agent to produce a prefoam is to create bubbles in the liquid mechanically by air entrainment. In the mechanical air-entrainment technique, bubbles are created as a consequence of induced liquid-gas instabilities, known as Rayleigh-Taylor instabilities. Such instabilities are often quantified by a dimensionless scaling number called the Weber number. The Weber number scales inertia forces to surface-tension forces. It is defined as $\mathrm{We} = \rho u^2 R / \sigma$, where u is the relative velocity between liquid and brush and σ is the liquid-gas surface tension. When We > 1, inertia forces exceed interfacial tension forces and consequently interfacial instabilities are generated. Such instabilities develop at existing liquid-gas interfaces, and contribute to interface breakup such that small bubbles are generated. The Weber number can be employed to calculate the size of bubbles that can be created by assuming that bubbles can be broken up when We > 1. Using typical values for density and surface tension as ρ = 6500 kg/m^3 and σ = 1 N/m and a relative velocity of u =3 m/s, the smallest bubble radius that can be broken up based on the above considerations is ~20 microns.

With a kitchen eggbeater as a model, a setup was built as shown schematically in Figure 8. The setup comprises a molybdenum whisk of 3 cm diameter that is spinning at speeds of up to 2500 rpm. This results in relative velocities between liquid and brush of up to 3 m/s. The liquid sample is processed in a graphite crucible that is inductively heated. Small bubbles are created by breaking up large bubbles originated by either

entrapping gas through the surface, or by releasing gas through a bubbler positioned underneath the whisk. In the mechanical air entrainment technique, relatively high material quantities are required due to the large size of crucible needed in this process. Therefore, in this prefoam technique, $Zr_{58.5}Nb_{2.8}Cu_{15.6}Ni_{12.8}Al_{10.3}$ alloy was used due to its relatively low cost.

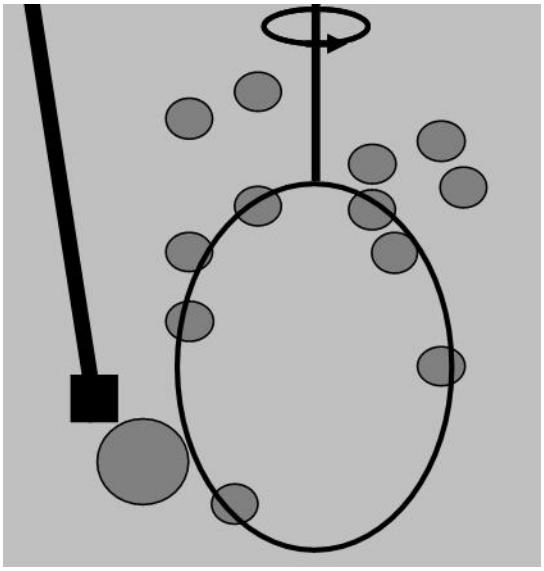

Figure 8. Schematic drawing of the eggbeater constructed for the mechanical air-entrapment method. The setup comprises a molybdenum brush of 3-cm diameter spinning at speeds of up to 2500 rpm.

Figure 9 shows a $Zr_{58.5}Nb_{2.8}Cu_{15.6}Ni_{12.8}Al_{10.3}$ prefoam synthesized by the mechanical air-entrainment method. The quenched prefoam consists of 10% by volume bubbles with an average size of 250 μm. The spatial distribution of bubbles appears to be fairly uniform, which implies that sedimentation was negligible during processing. Furthermore the size distribution of bubbles appears fairly narrow as shown in the magnified view (Figure 10). It can therefore be concluded that prefoams exhibiting adequate homogeneity can be produced by the air-entrainment technique. Unfortunately,

the amount of gas inside the bubbles was insufficient to activate significant expansion. To activate foaming, prefoaming should be performed under high pressures.

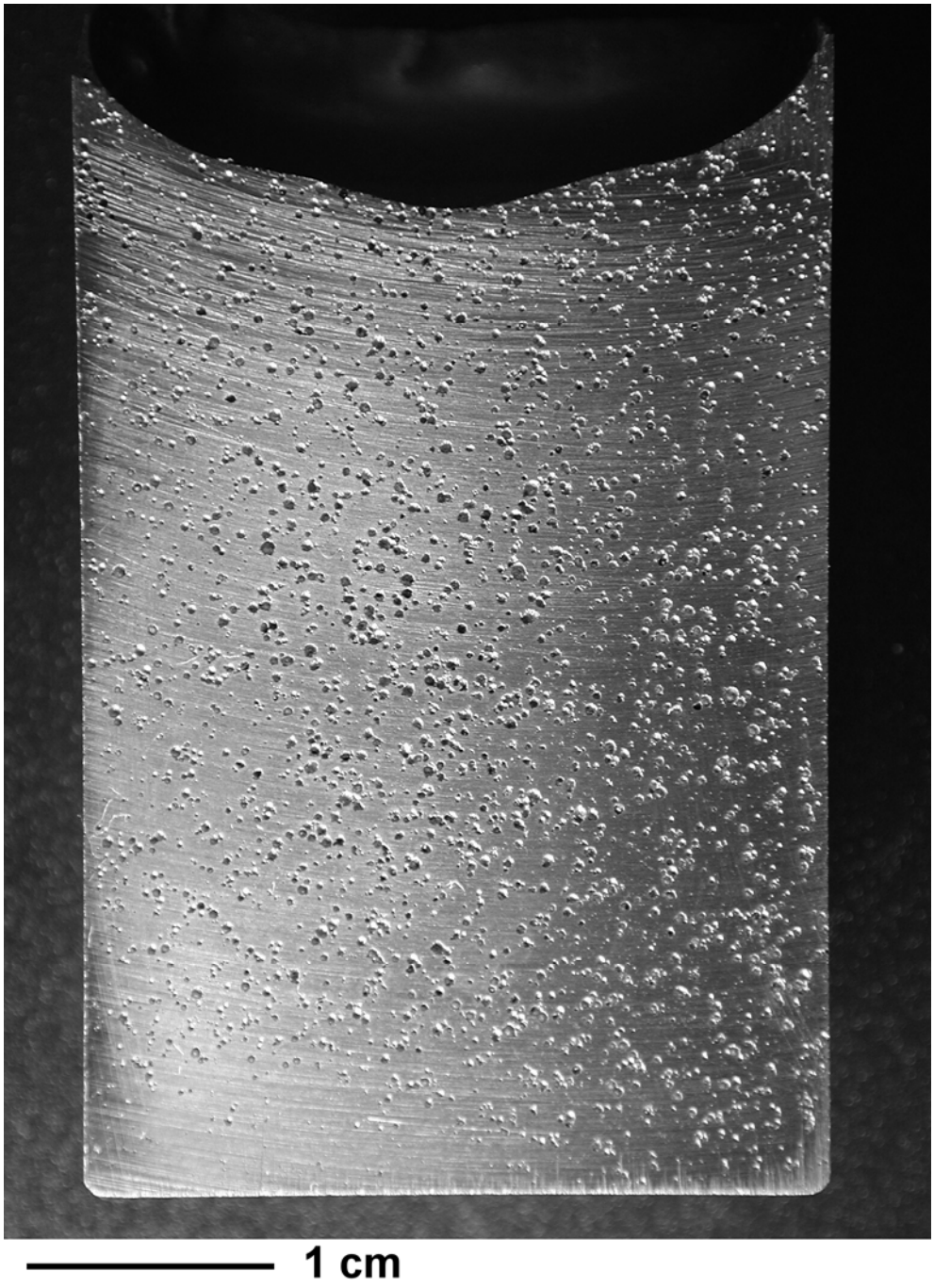

Figure 9. $Zr_{58.5}Nb_{2.8}Cu_{15.6}Ni_{12.8}Al_{10.3}$ prefoam synthesized by the mechanical air entrapment method. It consists of 10-vol% bubbles with an average size of 250 microns.

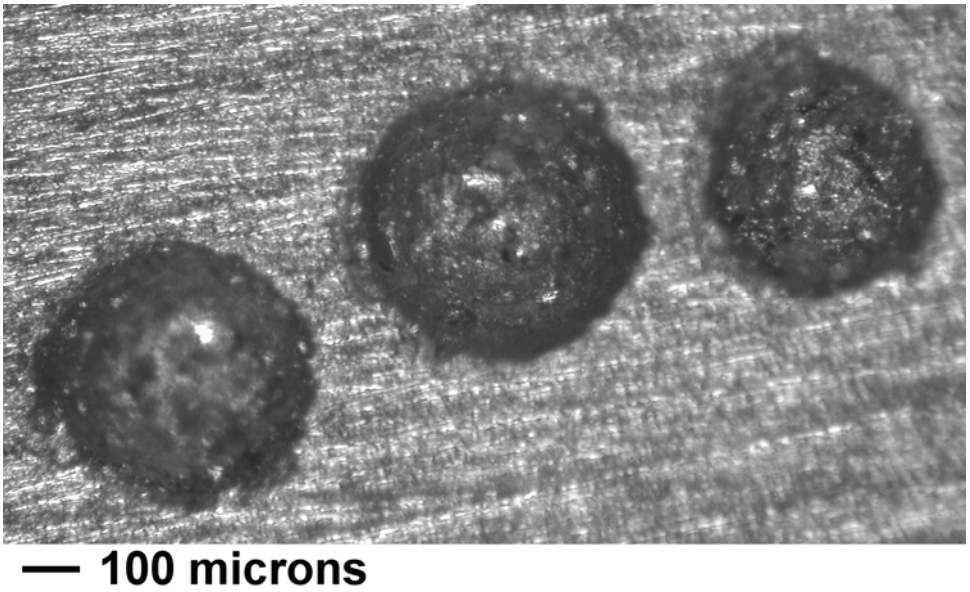

Figure 10. Magnified view. The bubble size distribution appears fairly narrow.

With a jig-saw as a model, a method was developed to entrain argon bubbles into molten metallic glass by agitating the sealed vessel using a high-speed jig-saw. The vessel is then water quenched and cut open as shown in Figure 11. Next, the prefoam is heated above the glass transition temperature and allowed to foam in a vacuum chamber. This synthesis route was developed for commercial alloys for two reasons. First, large batches of prefoams could be created in large vessels and subsequently expanded. Second, the entrainment of inert argon is thought to be ideal for commercial alloys which are easily contaminated by common blowing agents. Unfortunately, the jig-saw foam route has a few problems to overcome. Vitreloy is not meant to be melted and cast in a stainless steel tube as it degrades the glass forming ability.

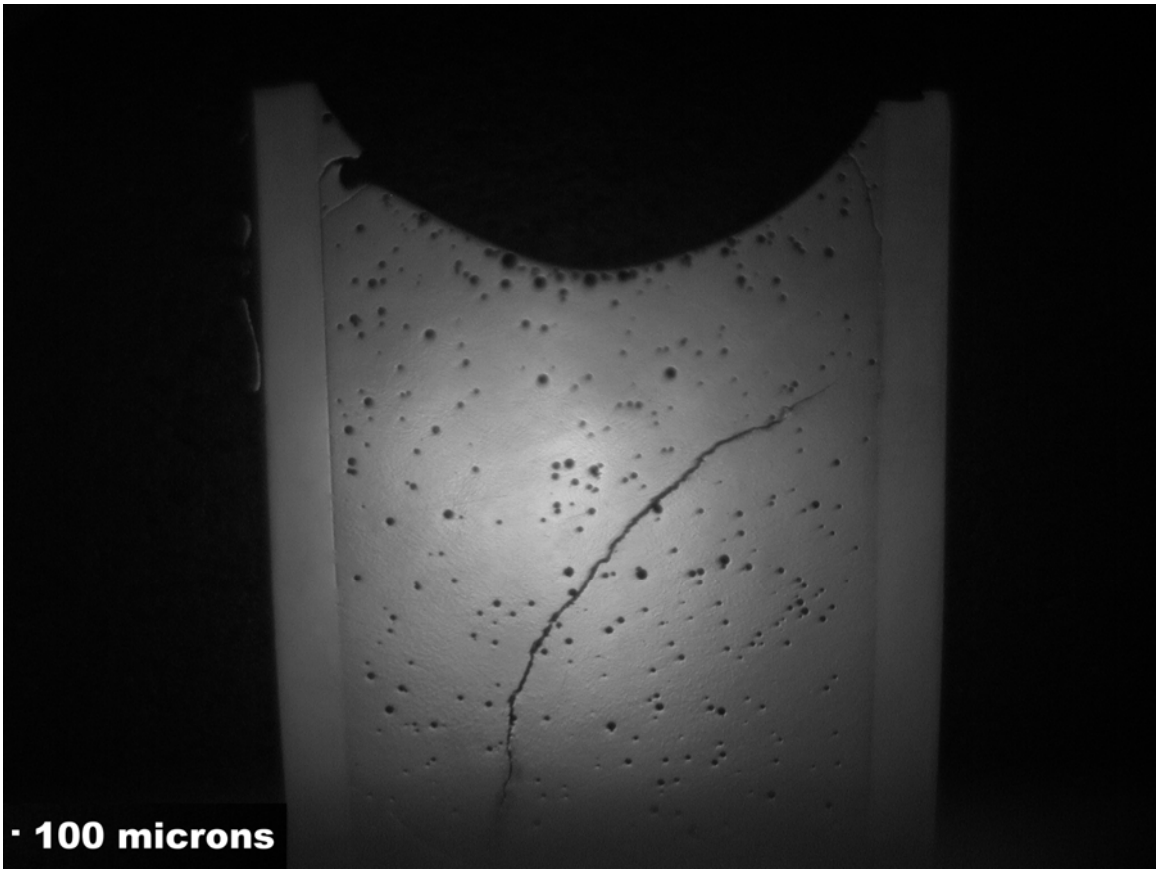

Figure 11. Vitreloy 1 prefoam made by jig-saw processing in a stainless steel tube. The crack across the sample is possible evidence of embrittlement.

In preliminary testing using glycerol, achieving high population bubble generation was problematic. Furthermore, it was shown that bubble generation by jig-saw entrainment was problematic as the creation of bubbles using the jig-saw resulted in annihilation of small bubbles and the steady-state bubble population was too low for successful foaming. Experimentally, sealing the stainless steel vessel to significantly high pressures needed for pore expansion not possible at the high temperature necessary to melt vitreloy. At the melting point of vitreloy, stainless steel begins to lose its strength. One suggestion would be to try using a vessel made of higher melting point alloy, such as inconel, which may retain its strength at the temperatures needed to melt vitreloy. Several foaming attempts were executed and the resulting foam expansion was

unsuccessful. Future attempts at jig-saw foaming or stirring entrainment processes should strive to improve bubble population and incorporate higher internal bubble pressures.

References

[1] Schroers J, Veazey C, Johnson WL. Amorphous metallic foam. Appl. Phys. Lett. 2003;82:370.

[2] Schroers J, Veazey C, Demetriou MD, Johnson WL. Synthesis method for amorphous metallic foam. J. Appl. Phys. 2004;96:7723.

[3] Rothwell E. Precise Determination of Viscosity of Liquid Tin, Lead, Bismuth, and Aluminium by an Absolute Method. J. Inst. Metals 1962;90:389.

[4] Kawamura Y, Inoue A. Newtonian viscosity of supercooled liquid in a $Pd_{40}Ni_{40}P_{20}$ metallic glass. Appl. Phys. Lett. 2000;77:1114.

[5] Ma LQ, Song ZL. Cellular structure control of aluminium foams during foaming process of aluminium melt. Scr. Mater. 1998;39:1523.

[6] Chino Y, Nakanishi H, Kobata M, Iwasaki H, Mabuchi M. Processing of a porous 7075 Al alloy by bubble expansion in a semi-solid state. Scr. Mater. 2002;47:769.

[7] Demetriou MD, Veazey C, Schroers J, Hanan JC, Johnson WL. Thermo-plastic Expansion of Amorphous Metallic Foam. Proc. Ismanam '05 (Jul. 2005). J. Alloys. Comp., 2005.

[8] Demetriou MD, Veazey C, Schroers J, Hanan JC, Johnson WL. Expansion Evolution During Foaming of Amorphous Metals. Proc. RQ12 (Aug. 2005). Mat. Sci. Eng.: A 2005.

[9] Wada T, Inoue A. Formation of porous Pd-based bulk glassy alloys by a high hydrogen pressure melting-water quenching method and their mechanical properties. Mater. Trans. JIM 2004;45:2761.

[10] Kearns MW. Formation of porous bodies. Patent Number 4,659,546. 1987.

[11] Baumeister J, Schrader H. Methods for manufacturing foamable metal bodies. Patent Number 5,151,246. 1992.

[12] Bae DH, Lee MH, Lee JK, Kim DH, Kim WT, Sordelet DJ. Ductile particle-reinforced amorphous matrix composite and method for manufacturing the same. Patent Number 6,669,899. 2003.

[13] International Publication Number: WO 2004/076099 A2.

[14] Kearns MW, Blenkinsop PA, Barber AC, Farthing TW. Int. J. Powder Metall. International Journal of Powder Metal 1988;24:59.

[15] Ohtera K, Inoue A, Masumoto T. High Mechanical Strength of Aluminum-Based Crystalline Alloys Produced by Warm Consolidation of Amorphous Powder. Mater. Sci. Eng., A 1991;134:1212.

[16] Kunze HD, Baumeister J, Banhart J, Weber M. P/M Technology for the Production of Metal Foams. Powder Metall. Int. 1993;25.